TAMPEREEN TEKNILLINEN YLIOPISTO
TAMPERE UNIVERSITY OF TECHNOLOGY

Turkka Salminen

Production of Nanomaterials by Pulsed Laser Ablation

Julkaisu 1121 • Publication 1121

Tampere 2013

Tampereen teknillinen yliopisto. Julkaisu 1121
Tampere University of Technology. Publication 1121

Turkka Salminen

Production of Nanomaterials by Pulsed Laser Ablation

Thesis for the degree of Doctor of Science in Technology to be presented with due permission for public examination and criticism in Sähkötalo Building, Auditorium S1, at Tampere University of Technology, on the 12th of April 2013, at 12 noon.

Tampereen teknillinen yliopisto - Tampere University of Technology
Tampere 2013

ISBN 978-952-15-3042-5 (printed)
ISBN 978-952-15-3051-7 (PDF)
ISSN 1459-2045

Abstract

Nanotechnology has been predicted to change many aspects of our everyday life and revolutionize the way we produce materials. The remarkable size-tunable properties of nanomaterials make them a hot research topic with far-reaching applications ranging from quantum computers to cures for cancer. To achieve these ambitious visions, new production methods need to be developed.

In this thesis the production of nanomaterials by pulsed laser ablation is investigated. This work was initially motivated by an interest to test recently developed high repetition rate fibre lasers in pulsed laser deposition (PLD) and pulsed laser ablation in liquids (PLAL).

In this work PLD was used to deposit thin films, nanoparticles and high surface area structures. The high repetition rate was observed to have important implications for the quality of the deposited films and the surfaces of the evaporated targets.

Nanoparticles produced by conventional chemical synthesis techniques often include unwanted residues from the reactants. These residues can be toxic and detrimental for applications. Nanoparticle production by PLAL has been shown to be a method capable of producing pure nanoparticles directly from a wide variety of bulk materials and compounds.

In this work a single-step PLAL process for production of luminescent GaAs-nanoparticles and silica-coated gold nanoparticles was developed.

Acknowledgements

This thesis presents the essential parts of the work that I carried out at Optoelectronics Research Centre, Tampere University of Technology during the years 2006-2012. The research was funded by the Finnish Funding Agency for Technology and Innovation (Tekes), Council of Tampere region, European Union regional development fund and Jenny and Antti Wihuri foundation, towards all of which I wish to express my gratitude.

The work involved the initiation of research activities in two fields not previously studied at ORC. This made the task both very interesting and challenging. Working as a 'pioneer' was a great learning experience but on the other hand the lessons were often learnt by trial and error. Throughout this process I have received help from many wonderful people who have made this thesis possible.

First I wish to thank my supervisor, Professor Tapio Niemi, for the guidance, the long discussions and the ideas that we few months later read about in minor journals like Nature. I am grateful to Professor Emeritus Markus Pessa for giving me the opportunity to work at ORC and for Dr. Pekka Savolainen, current director of ORC, for making sure that ORC is a place of high quality research year after year.

Throughout the years I have had the pleasure of working with many talented research assistants, especially Noora Viitanen, Mikko Hahtala, Ilkka Seppälä, Minna Kotilainen and Kirsi Lahtinen, to whom I am extremely grateful to. Noora and Minna helped me build the laboratory and shared the intense first years filled with visions and visionaries. During the long days and nights spent in the laboratory to further develop the equipment the help from Mikko and Ilkka was invaluable.

For the TEM analysis I owe thanks to Dr. Mari Honkanen and Dr. Hua Jiang, and to Dr. Soile Suomalainen for helping me understand the results of the analysis. From

the University of Turku I wish to thank Dr. Pekka Laukkanen for his expertise and encouragement and Johnny Dahl and Marja Tuominen for the XPS-measurements.

I am indebted to Dr. Janne Simonen, my personal guru in programming and simulation, without whom the simulations of chapter 4.3 could not have been accomplished. Dr. Antti Tukiainen is gratefully acknowledged for the countless advice and inspiring enthusiasm towards science. I wish to thank them both for the many interesting discussions about science and life in general.

I wish to thank all of my past and present co-workers for making ORC such a great place to work at. I am especially grateful to Anne Viherkoski and Eija Heliniemi for preserving my sanity in the fight against the wind mills of bureaucracy. Ilkka Hirvonen, Bengt Holmström, Timo Lindqvist, Antti Lepistö and Veli-Pekka Plym are thanked for the help in acquisition and fabrication of the laboratory equipment. Maija Karjalainen and Mariia Bister were immensely helpful during my feeble attempts to play chemist.

I thank Jorma Vihinen and Tero Kumpulainen for their assistance and the access to use the lasers of the Department of production engineering. For sharing their knowledge and expertise I am grateful to Prof. Petri Vuoristo, Dr. Eero Arola, Dr. Jukka Köngäs, Prof. Carmen N. Afonso and Dr. José Gonzalo.

For the support during the writing process of this thesis I wish to thank Dr. Antti Härkönen for making the LaTeX-template, Juha Kontio for our peer support group of two and Sanna Ranta for enduring my enthusiastic rants on various topics and accommodating to my musical preferences. Special thanks to family Turtiainen, to Charis for improving the language of the thesis and to Antti for the seamless agent-style co-operation in the delivery of the comments.

In addition to those who have directly helped me with my work, I wish to thank my friends for the countless joyful and memorable moments to counterbalance the intensive work. I am especially grateful to Onni Leiman & co. and *#bukkis*-community.

I have no words to express how grateful I am to my parents and family for their endless support and encouragement.

Finally, the warmest thanks go to my beloved Annukka.

Tampere, March 2013
Turkka Salminen

Contents

List of Publications

This thesis contains the following publications, published in peer-reviewed scientific journals:

[P1] T. Salminen, M. Hahtala, I. Seppälä, T. Niemi, M. Pessa, ”Pulsed laser deposition of yttria-stabilized zirconium dioxide with a high repetition rate picosecond fiber laser”, *Applied Physics A*, Vol. 98, pp. 487–490, 2010

[P2] T. Salminen, M. Hahtala, I. Seppälä, P. Laukkanen, T. Niemi, ”Picosecond pulse laser ablation of yttria-stabilized zirconia from kilohertz to megahertz repetition rates”, *Applied Physics A*, Vol. 101, pp. 735–738, 2010

[P3] T. Salminen, J. Dahl, M. Tuominen, P. Laukkanen, E. Arola, T. Niemi, ”Single-step fabrication of luminescent GaAs nanocrystals by pulsed laser ablation in liquids”, *Optical Materials Express*, Vol. 2, No. 6, pp. 799–813, 2012

[P4] T. Salminen, M. Honkanen, T. Niemi, ”Coating of gold nanoparticles made by pulsed laser ablation in liquids with silica shells by simultaneous chemical synthesis”, *Physical Chemistry Chemical Physics*, Vol. 15, pp. 3047–3051, 2013, DOI: 10.1039/C2CP42999C

Author's contribution

Publications P1 and P2 were a result of group work with the author of this thesis designing all of the experiments and performing the majority of the experimental work. In publications P3 and P4 all of the samples were designed and prepared by the author. The majority of the characterization was performed by the author. Co-authors contributed in additional material characterization.
The author is the main author in all of the publications. The contributions are summarized in the table below.

Publication #	Contribution in experimental work	Contribution in writing the publication
P1	Group work (80 %)	Main author (90 %)
P2	Group work (80 %)	Main author (90 %)
P3	Main work (90 %)	Main author (90 %)
P4	Main work (90 %)	Main author (90 %)

List of Abbreviations and Symbols

Abbreviations

CW	Continuous Wave, refers to lasers
EDS	Energy Dispersive Spectroscopy
HRTEM	High-Resolution Transmission Electron Microscope
LIBS	Laser-Induced Breakdown Spectroscopy
LIBWE	Laser-induced backside wet-etching
MBE	Molecular Beam Epitaxy
PLAL	Pulsed Laser Ablation in Liquids
PLD	Pulsed Laser Deposition
PVD	Physical Vapour Deposition
RGB	Red-green-blue
RTA	Rapid Thermal Annealing
SEM	Scanning Electron Microscope
SERS	Surface-Enhanced Raman Scattering
TEOS	Tetraethyl orthosilicate
TERS	Tip-Enhanced Raman Scattering
TOF	Time-of-flight
UHV	Ultra-High Vacuum
UV	Ultraviolet
XPS	X-ray Photoelectron Spectroscopy
YSZ	Yttria-stabilized zirconium dioxide

Symbols, elements and compounds

As	Arsenic
Au	Gold
$C(q)$	Weight function in Gaussian confinement model
C_{ext}	Extinction factor
c_l	Speed of sound in a liquid
CO_2	Carbon dioxide
d	Diameter of a nanocrystal
D_{spot}	Diameter of the laser focal spot
dg/dt	Rate of nanoparticle growth
E	Electric field
E_g	Band gap energy
E_p	Pulse energy
f_{laser}	Laser repetition rate
F_{th}	Ablation threshold
$f(\kappa a)$	Henry's function
g	Number of atoms in a nanoparticle
Ga	Gallium
GaAs	Gallium-arsenide
ΔG	Change in the Gibbs free energy
ΔG^*	The energy barrier required to form a nanoparticle of critical size
ΔG_V	Gibbs free energy change per unit volume
$I(\omega)$	Intensity
J/cm^2	Energy per area, unit of fluence

k_B	Boltzmann constant
n	Refractive index
Nd:YAG	Neodymium-doped yttrium aluminium garnet
N_p	Number of overlapping laser pulses
m	Atomic mass
P_∞	Liquid pressure at infinity
P^*	Probability of forming a nanoparticle with radius r^*
$P_B(t)$	Interior pressure of the bubble
q_0	Phonon wave vector
q	Heat of vaporization
r	Radius of a nanoparticle
r^*	Critical radius for stable nanoparticles
R, $R(t)$	Bubble radius
t	Time
T	Temperature
T_c	Critical temperature
T_{eq}	Equilibrium temperature
T_v	Vapour temperature
TiO_2	Titanium dioxide
$u(q_0, r)$	The potential caused by a crystal lattice
U_E	Electrophoretic mobility
v_E	Electrophoretic velocity
v_{scan}	Laser scanning speed
$v(T_v)$	Mean velocity
$W(r)$	Gaussian confinement function
Y	Yttrium
$Y(\theta)$	Spatial distribution of laser generated plume
Zr	Zirconium

Symbols, Greek alphabet

α_G	Confinement parameter
Γ_0	Natural linewidth of a phonon
ε	Dielectric function
ε_0	Dielectric constant of vacuum
ε_m	Dielectric constant of a surrounding medium
ε_r	Relative dielectric constant
ζ	Zeta-potential
η	Viscosity coefficient
κ	Extinction coefficient, imaginary part of the refractive index
λ	Wavelength
ρ_l	Density of the liquid
ρ_N	Number density of atoms
σ	Surface tension of the liquid
σ	Gibbs free energy change per unit surface area
τ_{e-p}	Time constant for electron-phonon coupling
$\Phi(q_0, r)$	Wave function of a phonon in an infinite crystal
ω	Wavenumber
$\omega(q)$	Phonon dispersion curve

Chapter 1

Introduction

This thesis deals with the production of nanomaterials. The work was initially motivated by an interest to test recently developed high-repetition rate fibre lasers in the various applications taking advantage of pulsed laser ablation. Particularly interesting topics were thin films made by pulsed laser deposition (PLD) and nanoparticles made by pulsed laser ablation in liquids (PLAL).

Light amplification by stimulated emission of radiation, the laser, was first demonstrated by Theodore Maiman in 1960 [1], 43 years after Albert Einstein laid its theoretical foundations in 1917 [2]. Though this novel light source was initially described as "a solution looking for a problem", now there are few fields of science or aspects of our everyday life that are not affected by lasers in one form or another. Therefore it might be said that the greatest success of lasers has been in finding suitable problems.

Around the same time, in the last days of 1959, Richard Feynman gave his now famous speech titled "There's plenty of room at the bottom" [3], which is considered as the figurative starting point of nanotechnology. At the time, Feynman was ahead of his time and the speech had little impact. It was only much later, in the late 1980's when it was rediscovered and widely referred to, as the new scientific field was taking its baby-steps. Maturation of nanotechnology has been predicted to revolutionize industry and our lives to a similar extent as electricity and computers did in the past.

Laser ablation was discovered in 1962 when Brech and Cross observed that intense laser pulses damage optical components and evaporate solid materials. [4] In 1965 Smith

and Turner [5] carried out laser ablation in vacuum and collected the evaporated material, thus performing the first experiments of PLD. However, PLD was not a widely applied technique until Dijkkamp and Venkatesan reported the successful fabrication of high-temperature superconductor thin-films by PLD in 1987. [6] Since then PLD has been shown to be a versatile technique, especially in the production of high-quality films from complex materials.

A new application for laser ablation was discovered in 1992 when Ogale *et al.* observed that the ablation of materials submerged in liquids produces nanoparticles. [7] Research in the field of PLAL is progressing rapidly and the mechanisms affecting the formation of nanoparticles are mostly understood. The PLAL method has been shown to be capable of producing stable nanoparticles of high purity, giving the method an advantage over the chemically produced particles that often contain trace amounts of residue chemicals. Partly due to their purity, nanoparticles produced with PLAL are highly suitable for further functionalization and can be readily embedded within *e.g.* polymers.

1.1 Structure of the thesis

This thesis is structured to serve as a brief introduction into the field of pulsed laser ablation in the production of nanomaterials. A reader who is interested in a quick overview of the topics handled in this thesis is advised to read the introductions of the chapters which provide an overview of the basic concepts and a brief history of their respective topics.

Chapter 2 addresses the motivation of this thesis: nanomaterials and the properties that make them so interesting for applications. Chapter 3 introduces the basic principles of laser ablation that are common to experiments performed in vacuum, gas and liquid environments. Chapter 4 is dedicated to pulsed laser deposition. This chapter is closely related to publications 1 and 2. Pulsed laser ablation in liquids is discussed in chapter 5 which is closely related to publications 3 and 4. The conclusions are presented in chapter 6.

Chapter 2

Nanomaterials

The properties of bulk materials and the individual atoms and molecules that form them are very different. The transition from atomic behaviour to bulk properties can be observed in nanomaterials. The size of these materials ranges from clusters of a few atoms, to particles a few tens of nanometers in diameter, and to nanotubes only a few nanometers in diameters, but millimeters in length. The defining factor is that at least one of the material's dimensions is on the nanoscale.

These nanomaterials have extraordinary properties that are typically size-dependent and thus tunable. A common definition for the upper size limit of what is considered a nanomaterial is 100 nm. At this size-range the phenomena responsible for the useful new properties are related to the increased surface area in respect to the total material volume. However, many of the more interesting properties of nanomaterials manifest at sizes closer to 10 nm and below.

The current and possible applications of nanomaterials and nanoparticles cover all fields of technology (Fig. 2.1). The possibility for increased control of the material behaviour combined with the need for less resources has been predicted to revolutionize manufacturing of materials. To understand the potential of nanomaterials one only needs to remember that 2 cl of water has approximately the same number of molecules as there are stars in our known universe. As Richard Feynman said: there truly is plenty of room at the bottom.

Nanomaterials research can be approached from two opposing directions. Feyn-

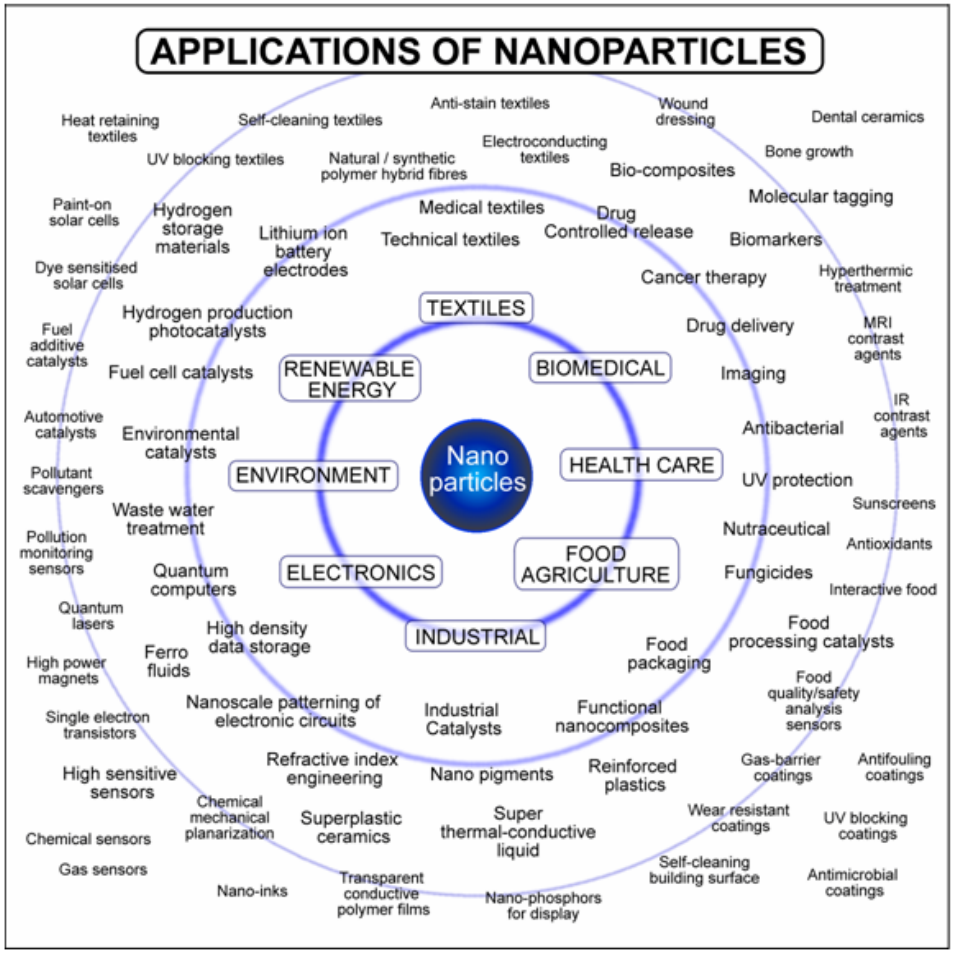

Figure 2.1: Nanoparticle research forms a significant fraction of all nanotechnology research. [8] The existing and potential applications of nanoparticles cover almost all fields of technology. [9][2]

man's vision was to use tiny nanofactories to build materials from individual atoms, *i.e.* to approach the issue from the bottom-up. [3] In the top-down approach, the starting materials are macroscopic and they are manipulated by *e.g.* evaporation or fragmentation to produce nanomaterials. Laser ablation, which was used in the discovery of C-60 buckminsterfullerenes [10], falls into the top-down category, though in a sense it shares features of both approaches.

[2]The figure has been reprinted from ref [9] with permission from the copyright holder Inderscience.

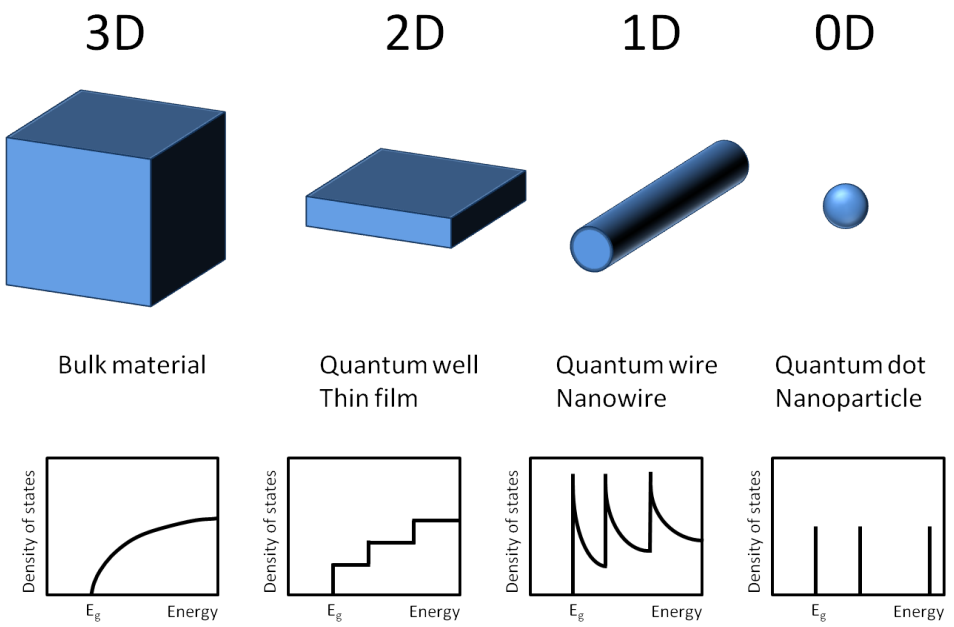

Figure 2.2: Nanomaterials are often classified by the number of their unconfined dimensions. The number of confined dimensions influences the density of the allowed energy states and 0D materials *i.e.* small nanoparticles, also known as quantum dots, approach atomic behaviour.

2.1 Quantum confinement

The size-tunable electrical and optical properties of small nanostructures arise from a quantum mechanical phenomenon known as quantum confinement. The excitation of a material leads to formation of electron-hole pairs that are called excitons. The excitons can in some sense be treated similarly to the hydrogen atoms. Therefore, the radius of the exciton is said to be the exciton Bohr radius. This radius ranges from a few nanometers to several tens of nanometers depending on the material. The effects related to the quantum confinement become important when the size of a physical dimension approaches the exciton Bohr radius.

The number of unconfined dimensions can be used to classify the types of nanomaterials (Fig. 2.2). Bulk materials are classified as '3D' since they are completely unconfined. Very thin films used as quantum wells in *e.g.* semiconductor lasers are classified as 2D materials. Nanotubes and quantum wires belong to 1D materials and finally, small

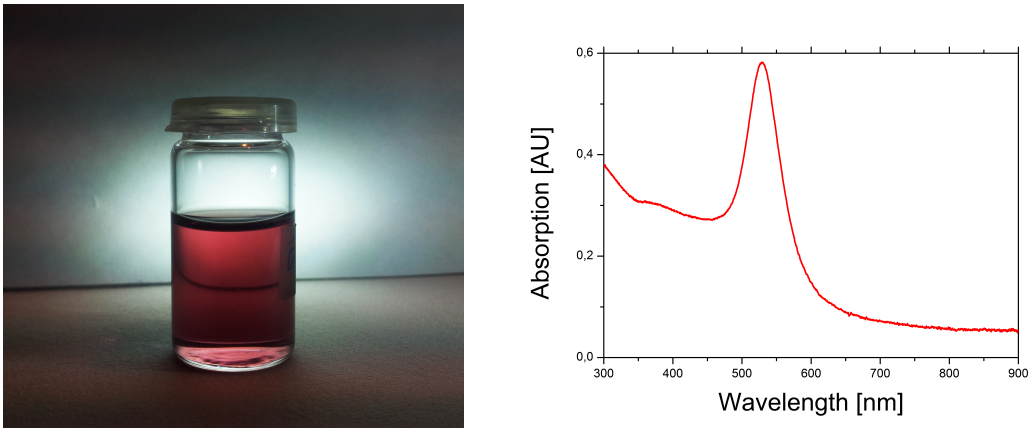

(a) (b)

Figure 2.3: Gold nanoparticles prepared by PLAL color the solution bright red due to their surface plasmon resonance (a). The transmission spectrum showing the plasmon peak of gold nanoparticles (b).

nanoparticles are 0D materials as all dimensions are confined. These small nanoparticles are sometimes called quantum dots to separate them from the larger nanoparticles that do not exhibit effects related to quantum confinement.

2.2 Plasmons in metallic nanoparticles

An important application field of metallic nanomaterials in particular is plasmonics. [11] It takes advantage of the collective oscillations of electrons driven by the electromagnetic field of light, *i.e.* plasmons. The surface plasmon polaritons that can be excited with light enable a plethora of possible applications. [11, 12]

Excitation of plasmons induces very strong local electric fields. This enhances non-linear optical effects by several orders of magnitude and is the basis of many well known measurement techniques, such as surface-enhanced Raman spectroscopy (SERS) [13,14] and tip-enhanced Raman scattering (TERS) [15]

In nanoparticles the localised surface plasmons produce resonances that are sensitive to the material properties as well as to the size and the shape of the particle. In the case of gold, the particle plasmon resonance can be identified from an absorption peak around

530 nm as shown in Fig. 2.3. In addition, the resonances are sensitive to the surrounding medium, which can be used in material characterization such as observing the growth of a shell around the particle, as will be shown in chapter 5.

Interaction of light and nanoparticles is described by the Mie theory. [16] In the case of a metallic nanoparticle, where the particle is much smaller than the wavelength of light, the scattering terms can be ignored and the extinction of light C_{ext} can be estimated from

$$C_{ext} = \frac{24\pi^2 r^3 \varepsilon_m^{3/2}}{\lambda} \frac{\varepsilon_2}{(\varepsilon_1 + 2\varepsilon_m)^2 + \varepsilon_2^2}, \tag{2.1}$$

where λ is the wavelength of light, ε_m is the dielectric function of the medium surrounding the nanoparticle and ε_1 and ε_2 are the real and imaginary parts of the dielectric functions of the material of the nanoparticle, respectively (see section 3.1). Peak-like resonances can occur if the condition $\varepsilon_1 = -2\varepsilon_m$ is satisfied at the so called plasma resonance frequency, which is characteristic to materials with free carriers *e.g.* noble metals.

2.3 Raman spectroscopy of nanomaterials

Raman spectroscopy is a well known technique for material characterization. [17] It is based on Raman scattering, where the scattering photon interacts with a molecular or lattice vibration (phonon) and loses or gains energy. When the photon loses energy the change in the photon energy is called a Stokes shift and when energy is gained an anti-Stokes shift.

Raman scattering is a phenomenon with a very low probability and the elastic Rayleigh scattering that conserves the photons' energy is typically $10^6 - 10^7$ times more probable. Therefore Raman spectrometry requires precise spectrometers and efficient filtering of the scattered light.

The intensity of the Raman signal can be enhanced by various techniques. Measurement with an excitation wavelength close to an allowed electronic transition in the material can improve the signal strength by several orders of magnitude. This approach

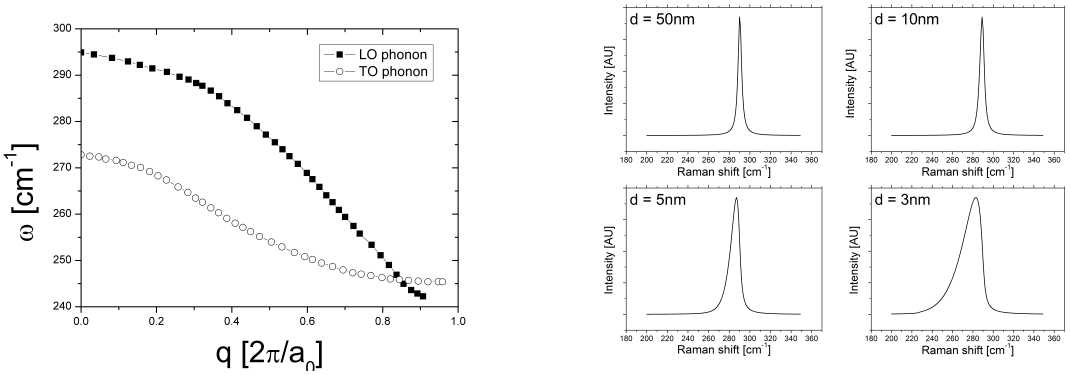

(a) (b)

Figure 2.4: Dispersion relation for the TO and LO phonon in GaAs, adapted from ref [21] (a). The evolution of the GaAs LO phonon as the size of the nanocrystal is reduced (b).

is known as resonant Raman spectroscopy. Nanomaterials and surfaces that are rough in the nanoscale are used in SERS and TERS.

Local field enhancement by metallic nanoparticles enhances the Raman scattering from molecules that are very close to the nanoparticle or adsorbed on its surface. This can be used to produce label nanoparticles with conjugated molecules that have identifiable Raman fingerprints. [18] This is a potentially powerful tool for medical diagnostics as the label particles can be selectively targeted to attach to *e.g.* cancer cells by additional functionalization of the particles. [19, 20]

Raman spectroscopy of nanoparticles

For a phonon with a wave vector q_0, the wave function $\Phi(q_0, r)$ in an infinite crystal is:

$$\Phi(q_0, r) = u(q_0, r)e^{-iqr}, \tag{2.2}$$

where the potential $u(q_0, r)$ has the periodicity of the lattice and r is the spatial coordinate. In a small crystal[3] the approximation of the phonon by a plane wave described

[3]The term crystal or nanocrystal will be used in this context instead of the term nanoparticle. This is because Raman scattering is influenced by the size of the individual crystals rather than the size of the whole nanoparticle.

by $\Phi(q_0, r)$ breaks down since it cannot propagate beyond the crystal surface. The phenomenological Gaussian confinement model [22, 23] approximates this by multiplying the original wave function $\Phi(q_0, r)$ by a confinement function $W(r)$

$$W(r) = e^{-\alpha_G r^2/d^2}, \tag{2.3}$$

where d is the diameter of the crystal and α is a phenomenological parameter that determines the strength of the confinement.

The intensity $I(\omega)$ of the Raman scattering at the wavenumber ω can be calculated from:

$$I(\omega) = \frac{|C(q)|^2 d^3 q}{(\omega - \omega(q))^2 + \left(\frac{\Gamma_0}{2}\right)^2}, \tag{2.4}$$

where $\omega(q)$ is the dispersion relation of the phonon, Γ_0 is the natural linewidth of the zone center phonon in the bulk material and q is the wave vector. $C(q)$ is the weight function, a Fourier-transform of $W(r)$,

$$|C(q)|^2 = e^{-q^2 d^2/2\alpha_G}, \tag{2.5}$$

for estimation of the contribution of phonons away from the centre of the Brilloun zone. For bulk materials and large particles, the numerator is very small due to $C(q)$, and the scattering intensity differs from zero practically only when $\omega \approx \omega(q)$ and the width of the peak is close to Γ_0. As the particle size gets smaller, the contribution for $\omega \neq \omega(q)$ can no longer be neglected and the shape and location of the peak is influenced by the dispersion relation as is illustrated in Fig. 2.4 (b).

It has been suggested that the value of α should be 2 [22], 9.67 [24] or $8\pi^2$ [25]. The value of $\alpha = 8\pi^2$, corresponding to a strong confinement within the nanocrystal, has often provided the best agreement with experimental data. Though the physical basis of the model is questionable, the model can be used to estimate the size of nanocrystals.

Chapter 3

Laser Ablation

Light in the form of high-energy laser pulses behaves very differently to what we have learned to expect through our senses. We can feel the warmth of sunlight on our skin on a summer day and we know how hot a dark surface can get in direct sunlight. We know that the sweet sugar we taste is a product of photosynthesis. And of course, the most efficient way for us to observe our surroundings and to gain new information is through light and vision.

Common to these everyday phenomena is their linear nature. Thus, the intensity of light, *i.e.* the amount of photons, defines the strength of the phenomenon, but does not change the phenomenon itself.

A good reference for an everyday light source is sunlight. The intensity of sunlight on the surface of the Earth is approximately 1000 W/m^2, or 0.1 W/cm^2, expressed in units more often used with lasers. With a regular magnifying glass the intensity can be increased to approximately 0.5 W/cm^2, which is enough to burn paper, wood and as some twisted children know: ants. In concentrator solar cells and solar furnaces the intensity can be increased above 100 W/cm^2. Though these intensities might already seem high, the related phenomena are still linear.

Lasers have two qualities that enable generation of much higher intensities. First, the produced light is nearly monochromatic and coherent, which allows efficient focusing. Second, several different techniques enable generation of short laser pulses resulting in high peak intensities with modest average powers. High intensities change the interac-

tion of light and matter, due to the extreme rate of the interaction events, and due to the related high electro-magnetic fields which give rise to various non-linear effects.

The intensities typically used in laser ablation and in this work range from 10^8–10^9 W/cm^2 with nanosecond pulses, to 10^{10}–10^{13} W/cm^2 with pico- and femtosecond pulses. These intensities are high enough to evaporate any material, but even they pale in comparison with the lasers currently being tested in several different projects with the aim to surpass intensities of 10^{23} W/cm^2. [26, 27]

Removal of material with such short laser pulses is known for its high precision and is called *laser ablation*[1]. The laser ablation process begins with the absorption of the energy of the laser pulse by electrons. The absorption is followed by the energy transfer from the excited electrons to the crystal lattice, which leads to very rapid heating and breakdown of the laser illuminated area. This leads to formation of plasma and ejection of atoms, molecules and clusters. The different processes related to laser ablation are mostly well understood.[2] However, theoretical models capable of reliable predictions are not available.

Laser ablation is a seemingly simple process that can be applied without full understanding of the underlying mechanisms. The lasers used in various studies have created a wide spectrum of different results depending on the wavelength, pulse length and pulse energy. Furthermore, the beam profile and the temporal shape of the pulse can have a significant impact on the process, which in most of the studies is given little or no attention. These factors have fueled some debate about the governing mechanisms in laser ablation under various conditions and have slowed down the development of generally applicable models. Also in many practical applications, *e.g.* in PLD and in PLAL, the most useful intensities are relatively low, just slightly above the ablation threshold, whereas many of the more complex mechanisms manifest at much higher intensities.

Laser ablation can be divided into two domains on the basis of the pulse length of the applied laser. The mechanisms responsible for the absorption and subsequent ablation are very different for nanosecond and femtosecond pulses. The majority of the work

[1] For an interesting discussion on the etymology of the term ablation and on the definition of what is considered laser ablation, see the introduction of reference [28].

[2] A slight exception is formed by ablation with femtosecond pulses. The related mechanisms and especially their importance is still under some debate.

in this thesis was performed with picosecond pulse lasers, which share features with lasers of both pulse lengths and thus the general features of both ablation domains will be discussed.

In this chapter we introduce the fundamentals of laser ablation that form the basis of this thesis. We begin by a brief discussion of the interaction of light and matter and the various mechanisms of absorption that are relevant with short laser pulses. We consider the timescales of the effects following the absorption and the dynamics of the eventual evaporation of the material. The final section (3.7) of the chapter deals with the effects caused by the high repetition rate lasers used in publications 1 and 2. As a final summary of this chapter, an instructive graph is presented (Fig. 3.12).

3.1 Interaction of light and matter

Light can interact with a material in many different ways. Light can be absorbed within the material, it can be reflected or refracted on interfaces of different materials and it can be scattered from non-uniformities such as defects and particles in the material.

Interactions between light and matter are always interactions between photons and electrons. For example, heating of the material is a secondary effect that results from the subsequent interaction of the excited electrons with the crystal lattice. In these interactions the electrons are exchanging energy with the lattice vibrations known as phonons.

The color and appearance of materials depends on how they absorb and reflect different wavelengths of light and how the light refracts on the surfaces of (partially) transparent materials. The behaviour of a material in these linear interactions can be described by the dielectric function (permittivity), ε

$$\varepsilon(\lambda) = \varepsilon_1(\lambda) + i\varepsilon_2(\lambda). \tag{3.1}$$

The dielectric function depends on the wavelength, λ , and it has a real component ε_1 and an imaginary component ε_2. The relationship of the dielectric function to the commonly used refractive index is

$$n(\lambda) + i\kappa(\lambda) = \sqrt{\varepsilon(\lambda)} \tag{3.2}$$

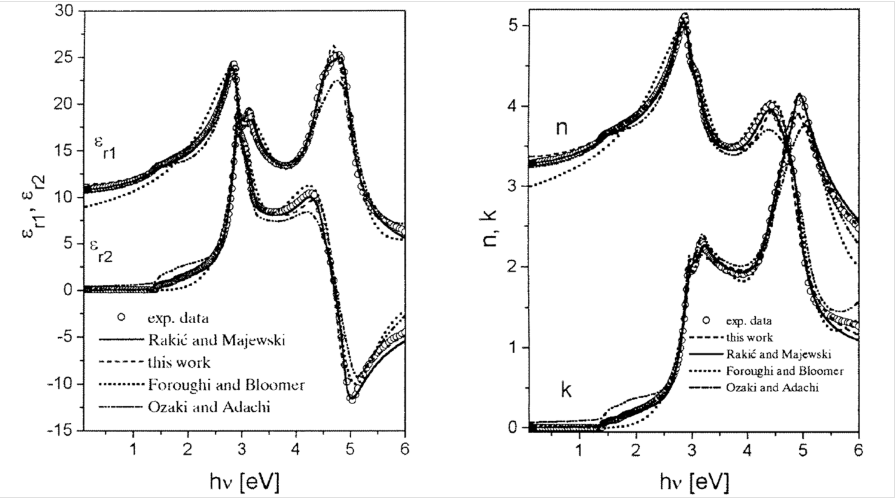

Figure 3.1: The visual appearance of a material depends on its dielectric function, which can also be expressed as the index of refraction. [29][4]

The real part of the refractive index, n , describes the wavelength and the speed of light in a material and as its name suggests, the refraction of light on the interfaces with other materials. The imaginary part, κ , describes the absorption (or gain) of the material.

3.2 Absorption of light

From the perspective of a single photon, κ can be interpreted as the probability of absorption. In the case of linear interactions, the absorption probability differs from zero only for wavelengths that correspond to the allowed electron transition energies in the material. For individual atoms the allowed transitions are defined by the occupied and unoccupied energy states. For bulk materials the individual electron states are replaced with energy bands. Sufficiently high energy photons can also directly free the electron and ionize the atom or material.

In insulators and semiconductors the electrons are in the *valence band* and the absorption occurs by excitation of the electrons to the *conduction band* over the band gap. The band gap has no allowed energy states. Metals have a considerable amount of elec-

[4]The figures are reprinted from the reference [29] with the kind permission of the original authors and IOP Publishing Ltd

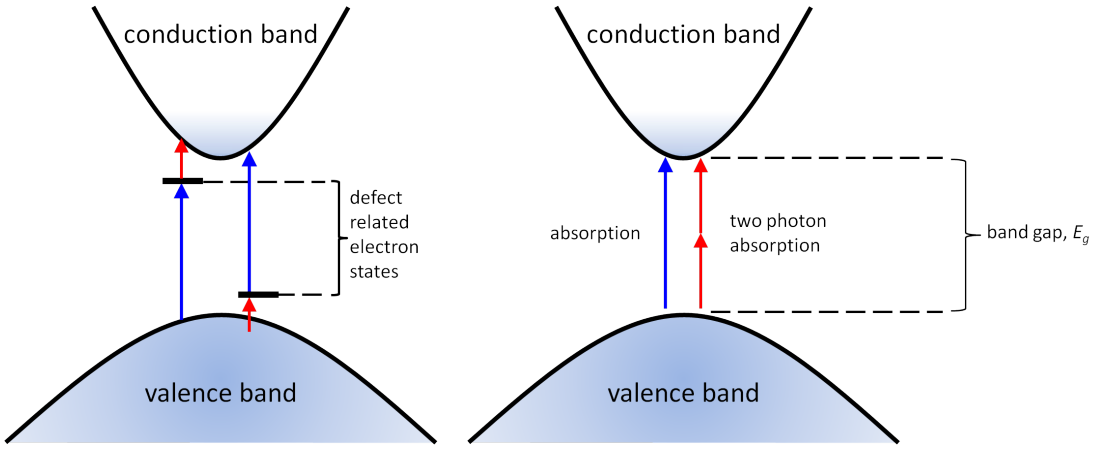

Figure 3.2: A single photon can be absorbed by the material if the photon energy is at least equal to the bang gap energy E_g of the material. (a) Defects within the band gap can directly accept or donate an electron to the material and allow absorption with sub-band gap wavelengths by serving as intermediate states. (b) Very high intensity illumination enables multi-photon processes, where two or more photons are absorbed almost simultaneously.

trons in the conduction band, which absorb the light in a thin layer with a thickness roughly corresponding to the optical penetration depth.[5]

All real materials are non-ideal and include impurities and defects. The electron energy states related to these non-idealities can lie within the band gap of an insulating or a semiconducting material. This allows some absorption at photon energies lower than the band gap energy, where electrons can be excited from the valence band to the defect states and subsequently from the defect states into the conduction band (Fig. 3.2 (a)). The probability of such a two-phase excitation process depends on the life-time of the electron in the defect state.

In high-quality materials, like the ones used in semiconductor industry and optics, the number of defects is typically so low that the defect-assisted conduction electron generation does not significantly alter the optical properties of the material unless the

[5]The absorption process for a conduction band electron is a three-body interaction with the additional momentum provided by another electron or a phonon of the lattice. In the case of free electrons in particular this mechanism is referred to as *inverse brehmsstrahlung*. [30]

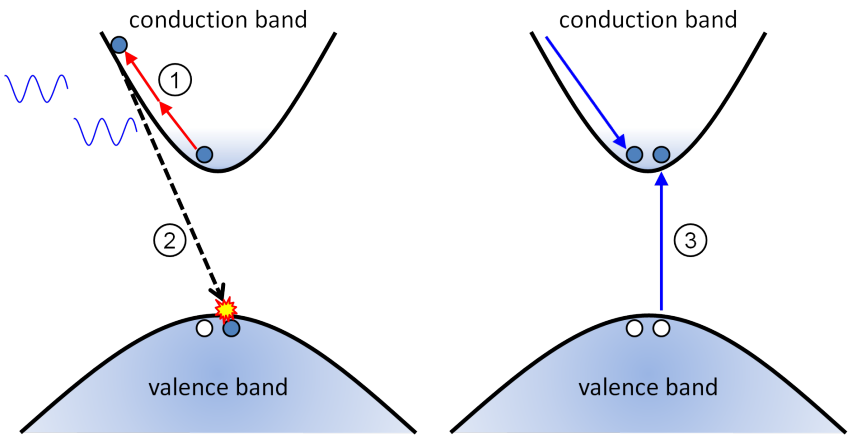

Figure 3.3: An electron in the conduction band can absorb photons with energies much lower than the band gap energy. If the electron gains enough kinetic energy, it can excite an electron from the valence band to the conduction band. Under continued, intense illumination this process can rapidly lead to an avalanche as the number of electrons increases exponentially.

intensity of the exciting light is very high – close to the intensities produced with focused pulsed lasers.

Electrons in the valence band can also be excited to so called virtual states that have extremely short life-times on the order of one femtosecond. Another photon can excite the electron from the virtual state to a higher allowed energy state or to another virtual state (Fig. 3.2 (b)). The probability of this multi-photon absorption [31] is extremely low and it becomes significant only at sufficiently high intensities, on the order of $10^{12} W/cm^2$. In laser ablation this phenomenon is thus significant mostly when femtosecond pulses are used. Two photon absorption has found many applications in imaging [32, 33] and in a high resolution three dimensional micro-fabrication method called two-photon polymerization [34].

With even higher laser intensities the electric field of the light can distort the local potential of the crystal lattice, allowing tunneling ionization. [30, 35, 36]

The allowed energy states in the conduction band lie close to each other and thus conduction band electrons can absorb photons with energies much lower than the band gap energy. Electrons that absorb multiple low energy photons can get enough energy to excite valence band electrons to the conduction band through collisions (Fig. 3.3). Thus

even a low number of conduction band electrons, generated *e.g.* through defect-related absorption or thermally, can seed an avalanche process under sustained high intensity illumination. This phenomenon, known as avalanche ionization or impact ionization, can transform an insulator or a semiconductor into a metal-like material very rapidly.

These mechanisms allow absorption and laser ablation even with lasers for whose wavelength κ is zero. The sequential *multiple-photon* processes are typically significant at lower intensities than the simultaneous multi-photon and strong-field processes. However, the relative importance of the various excitation mechanisms depends on the material and on the laser parameters. The significance of these mechanisms is also dependent on the wavelength and the wavelength dependency of each mechanism.[6]

For nanosecond pulses the prevalent mechanism is typically impact ionization. The seed electrons are generated by direct absorption, if the wavelength of the laser is suitable, or through defect assisted absorption. In some cases multi-photon absorption can also take place, but it's less important than for femtosecond pulses. In nanosecond pulse laser ablation, lasers with wavelengths in the ultra-violet range are usually preferred to guarantee high ablation efficiency through direct absorption in the material.

With femtosecond pulses the importance of multi-photon absorption increases. Not only is it responsible for generation of the seed electrons for impact ionization, but it can also be the dominant absorption mechanism. Tunneling ionization typically requires higher intensities than those commonly used in laser ablation, but in some cases, especially with long wavelength lasers, it can have a significant effect. [37] The higher intensities make femtosecond lasers less dependent on the laser wavelength.

When picosecond pulses are used, the dominant absorption mechanisms depend strongly on the material. For most materials the laser wavelength is still an important factor.

3.3 Melting of laser excited material

Under low intensity illumination, *i.e.* in the linear region, an excited electron will eventually relax back to a lower energy state. In the relaxation process the excess energy is

[6]For a good review on the significance of the different mechanisms, see *e.g.* reference [36]

either emitted as a photon or deposited to the crystal lattice as phonons, *i.e.* heat.

After a high intensity laser pulse, the material is in a non-equilibrium state where the area treated with the laser has more energy than the surrounding material. The surrounding material can still be at the ambient temperature, whereas the temperature for the laser affected area can be extremely high, though it is not necessarily unambiguously defined. The distribution of the energy depends on the pulse length.

As previously discussed, the energy of the laser pulse is absorbed by the electrons. The rate of the energy transfer from electrons to the lattice depends on the strength of the electron-phonon coupling. The time constant, τ_{e-p} , describing the rate of the process varies between materials but is typically from picoseconds to a few tens of picoseconds.

Melting after excitation by nanosecond pulses

With pulses longer than τ_{e-p}, the energy transfer to the lattice takes place already during the duration of the laser pulse. At the end of a nanosecond pulse, the temperature of the laser treated area has increased considerably [38], while thermal diffusion has not significantly distributed the energy into the surrounding material.

If the absorbed energy is high enough, the laser affected volume will melt through one of the various mechanisms observed in laser ablation. [38–43]

Generally, melting of a material starts from the surface where the binding energy of the atoms is the lowest. The melting front progresses into the bulk of the material relatively rapidly. The upper limit for the velocity of the front is the speed of sound in the materials, though the actual speed is typically considerably slower. [44] The thickness of the absorption layer that contains the energy of the laser pulse is typically on the order of 100 nm. Therefore, for typical solids the melting will take from a few tens to approximately one hundred picoseconds. With nanosecond pulses the material can thus melt during the laser pulse (Figs. 3.4 and 3.5). [38]

Behaviour of material after excitation by femtosecond pulses

If the laser pulse is shorter than τ_{e-p}, the electrons have most of the energy of the laser pulse when the laser pulse ends. Thus the electron temperature is higher than the lattice

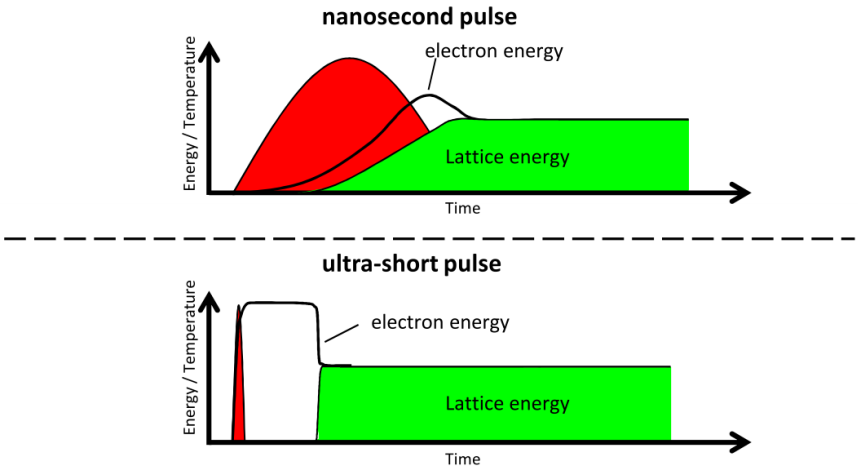

Figure 3.4: The energy of the laser pulse is absorbed by electrons. With long pulses the energy is transferred to the lattice during the laser pulse. If the laser pulse is shorter than the electron-phonon coupling time constant, *i.e.* the pulse is "ultra-short", the electrons have all of the energy when the pulse ends. In this case the subsequent energy transfer process is governed by the material dependent electron-phonon coupling.

temperature (Fig. 3.4).[7] In this case the following energy transfer is governed solely by the electron-phonon interactions.[8]

The energy transfer to phonons happens almost simultaneously in the whole absorption volume. This can lead to considerable superheating and enables homogeneous nucleation, where the whole volume melts much faster than would be possible through normal melting. [39, 41, 42] Melting through homogeneous nucleation takes place typically on the order of a picosecond. [39, 43]

Some of the energetic electrons will escape the laser-affected volume into the sur-

[7] Theoretical approaches often use a two-temperature model to describe this situation [28, 45–51]. Initially the electrons do not follow the Maxwell-Boltzmann-distribution and the electron temperature is not clearly defined. The thermalization of the electron gas through electron-electron collisions takes place in a time-frame of several hundred femtoseconds [51] and in many cases the electron temperature can be considered to be defined at the onset of electron-phonon interactions.

[8] Though the term "ultra-short laser pulse" is not unambiguously defined and depends on the application field, in the context of laser ablation a pulse shorter than the electron-phonon coupling time constant for the material in question can safely be said to be "ultra-short".

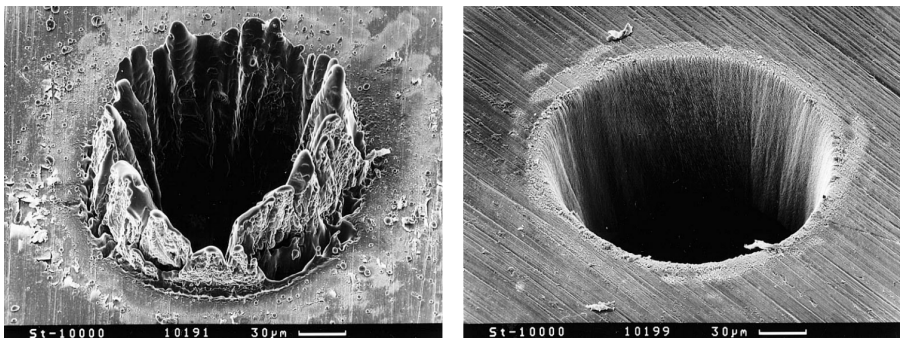

Figure 3.5: Craters produced on stainless steel after laser ablation with nanosecond (left) and femtosecond (right) laser pulse. [10]

rounding material and some are emitted from the material. With femtosecond pulses, a considerable amount of the electrons are emitted from the material almost instantaneously. The excess positive charge can lead to crystal instability due to elecrostatic repulsion and emission of positive particles through a mechanism called Coulomb explosion. [52–55] The mechanism is more common in dielectrics, where the neutralization of the laser-generated holes is slower, but it is also possible in semiconductors. [56, 57]

With very high intensities the generated electron-hole plasma can cause the crystal to become electrostatically unstable, which then leads to nonthermal melting in just a few hundred femtoseconds. [40]

It should be noted that in all of these cases the melting is very rapid compared to heat diffusion. Therefore, after the laser affected volume has melted or lost its crystalline structure, the surrounding bulk can still be relatively cool and unaffected.

3.4 Ablation of laser excited material

When the energy absorbed from the laser pulse is high enough to cause ablation, it is said to be above the *ablation threshold*[11]. The threshold is most commonly expressed as the total energy per area, *fluence* F_{th}, in the units J/cm^2. The mechanism of ablation,

[10] Fig. 3.5 has been reprinted from [58] with permission from Springer Science and Business Media.

[11] The ablation threshold and its dependence on laser parameters is discussed in more detail in section 3.6

like the mechanism of melting, depends on the length and the energy of the pulse. In this section we will inspect the ablation mechanisms assuming that the pulse energy is close to the ablation threshold, which typically is the case the in PLD and PLAL.

Another very important factor is the surrounding medium into which the evaporated material expands. Here we will start the discussion by considering a special example of ablation into vacuum and low-pressure gas atmospheres. Expansion into liquids is discussed in chapter 5.

The ablation process is in most cases a combination of mechanisms of various origins: thermal, electrostatic and mechanical. As a rule of thumb, thermal processes dominate ablation with nanosecond pulses and the other mechanisms start to become more important as the pulses get shorter and the intensities rise.

Ablation after excitation by nanosecond pulses

When the pulse duration is nanoseconds or longer, the experimental results can usually be explained through thermal mechanisms[12]. [28] The molten material starts to evaporate during the laser pulse and forms a so called *Knudsen layer* [59], a region near the surface of the material where the evaporating particles collide with each other and approach a thermal equilibrium. The atoms and ions emerging from the Knudsen layer can have kinetic energies in the range of 10-100 eV, corresponding to velocities of a few tens of kilometres per second, leading to a rapid expansion into vacuum. [60–62]

Nanosecond pulse lasers can interact with material in this initial layer, with two important consequences. First, the evaporated material absorbs more energy, leading to dissociation of molecules and small particles and ionization of some of the neutral atoms, which leads to formation of plasma. Second, absorption and scattering shields the target material underneath and lowers the ablation efficiency. Both of these effects are mostly absent in femtosecond pulse ablation with significant consequences that are discussed later.

The collisions during the early stages of the plasma formation and continuation of the absorption of the energy from the laser can lead to some back-scattering of the atoms

[12]Exceptions can arise due to very short wavelengths, pulse energies well above the ablation threshold or material properties.

and sputtering of the underlying material. However, this is not usually a major effect in laser ablation in low-pressure gas atmospheres near the ablation threshold.

In materials with atoms of more than one element, normal, thermal evaporation leads to a different evaporation rate for each element depending on its partial vapour pressure. In laser ablation however, the elements are typically evaporated congruently.

Increasing the laser intensity leads to higher temperatures and increases the rate of ablation quite consistently until the temperature approaches the thermodynamic critical temperature T_c. Around temperatures of $\sim 0.9T_c$ [63] homogeneous nucleation can lead to explosive relaxation into a mixture of vapour and liquid droplets in the so called *phase explosion* [64–67]. This is typically observed as a jump-like increase in the amount of evaporated material and is accompanied by observation of ejected droplets. The transition is typically observed with fluences on the order of $5 - 10 \times F_{th}$. [68–70]

Ablation after excitation by femtosecond pulses

The ablation process after femtosecond pulse excitation is more complicated than in the case of nanosecond pulses. The actual ablation takes place long after the pulse has ended and the thermal mechanisms no longer sufficiently describe the process.

Under low fluence conditions near or slightly below the F_{Th} most solid materials behave in a similar manner. [71, 72] The rapid melting of materials has been directly imaged with high temporal resolution in pump-probe experiments. [72]

Desorption of atoms and molecules from non-metallic materials can be observed in experiments and simulations. [73, 74] This low fluence behaviour is caused by the Coulomb explosion and it is characterized by ablation of a thin layer, with a thickness of a monolayer or a few nanometers. The Coulombic repulsion origin of the mechanism is manifested in the distinct charge dependent kinetic energies of the emitted ions. [54, 55, 75, 76] In metals, the charge-instability is rebalanced by the electrons from the bulk of the material too rapidly for Coulomb explosion to occur.

Above F_{Th} the rapid energy transfer from the electrons to the lattice can lead to temperatures well above T_c and to a superheated solid state. [77] The thickness of the evaporated layer grows rapidly to several tens of nanometers and higher.

The ablation is caused by a combination of several mechanisms. In addition to phase

explosion also observed with high-intensity nanosecond pulses, the rapid relaxation of the material leads to formation of a shock wave and tensile stress that can cause fragmentation[13]. [77–80] Femtosecond ablation thus inherently generates droplets and fragments.

The lack of interaction between the laser pulse and the evaporating material avoids the plasma shielding effect, but on the other hand inhibits the dissociation of molecules and clusters. This leads to a significant difference between nanosecond and femtosecond pulse ablation. Whereas the plume generated by a nanosecond pulse consists mostly of atoms and ions, the femtosecond generated plume has a significant fraction of clusters that can serve as nucleation centres for nanoparticles. [77, 81–86]

The absence of thermal processes near F_{Th} make femtosecond pulse ablation a very precise tool for micro-machining (Fig. 3.5). [58] However, due to the inherent generation of nano-particles, femtosecond lasers are not as well suited for PLD as nanosecond lasers.

Picosecond pulses

Typical picosecond pulse lasers produce pulses with durations from a few picoseconds up to a few tens of picoseconds, closely corresponding to τ_{e-p} of typical solids. Therefore the governing processes can vary considerably depending on the material and the exact parameters of the laser. Typically the intensity is not high enough for significant multi-photon ionization near F_{Th} and thus avalanche ionization with seed electrons provided by direct absorption and defect assisted absorption is the dominant absorption mechanism.

The heating and decomposition of the material starts during the laser pulse and thus the laser will interact with the initial phase of the decomposition. However, the pulse is over before significant ablation has time to occur and thus the evaporated clusters are not dissociated by the laser.

Therefore picosecond pulse ablation is a mixture of nanosecond and femtosecond pulse regimes. The absorption mechanisms are often typically those of nanosecond pulse ablation, melting and ablation processes have features of both regimes, and the emitted

[13] In soft materials like tissues, this can lead to spallation.

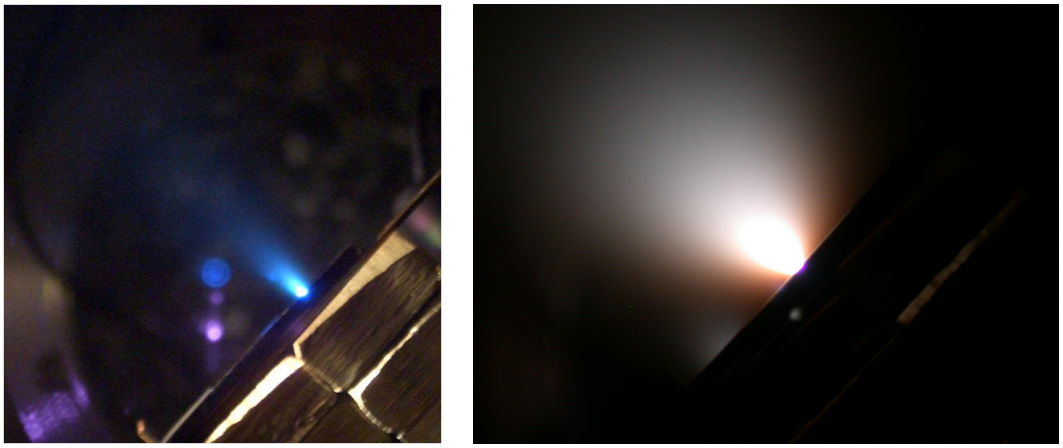

a) (b)

Figure 3.6: Analysis of the laser generated plasma yields a lot of information about the ablation process and the ablated material. (a) Atomic plasma from an aluminium target has a distinct blue color that results from the emission due to the fluorescence of the excited atoms and ions. (b) A plasma with nanoparticles emits a broad spectrum reminiscent of black body radiation. The analysis of the spectrum can be used to estimate the temperature of the particles.

plume has clusters similar to similar to those produced by femtosecond pulse ablation.

The pulse energy of picosecond pulses near the threshold is higher than that of a femtosecond pulses and thus enables more material to be evaporated per pulse. This makes picosecond lasers attractive for micro-machining as a compromise between precision and efficiency as long as the material properties are taken into account. In PLD the picosecond pulses tend to produce similar results as femtosecond lasers and thus are not as well suited for production of high-quality films as nanosecond lasers.

3.5 Laser generated plasma/plume

The laser excited, hot and dense material rapidly expands and forms a plume that characteristically emits light from the excited species and hot particles (Fig. 3.6). Under most conditions the plume includes a considerable fraction of ions and free electrons and is thus called a plasma.

The high density in the initial stages of the expansion induces collisions between the

particles. The number of collisions required to establish an equilibrium is low (approximately 3 to 5). [87] It can thus be estimated that the Knudsen layer is formed when more than one monolayer is evaporated within a few nanoseconds. [59, 88] This justifies the use of hydrodynamic expansion models to describe the behaviour of the plume. [88–93] After the possible initial interaction with a long laser pulse, the expansion into vacuum can be considered as adiabatic. In the most successful models the plume expansion is considered to be isentropic as well. [90,91] The model predicts a spatial distribution $Y(\theta)$ of the plasma that is strongly directed along the normal of the surface of the material and is of the form

$$Y(\theta) = A\cos^p\theta, \tag{3.3}$$

where θ is the angle from the normal, p depends on the aspect ratio of the plasma and A is a fluence dependent scaling factor. [60] This distribution agrees well with experiments, with values of p typically between 2 and 10. [94, 95]

Expansion into an inert background gas starts in a similar way to expansion into vacuum due to the high initial energy of the plasma, but the expansion is slowed down and confined by collisions between the plasma and the gas. The collisions typically lead to ”plume splitting” and the plume has a fast moving front, which is followed by particles slowed down by the collisions. This distribution evolves as the plasma expands, with the fast component decaying roughly exponentially. [96–98] With sufficiently high pressures, the collisions in the expansion front can lead to formation of nanoparticles and nanotubes. [97]

The plume will eventually stop when the internal pressure matches the pressure of the background gas. In typical PLD-setups, the plume will hit the substrate and form a thin film. Some particles recoil from the surface and in some cases bounce back and forth between the substrate and the target. [97,99] The most energetic particles can cause sputtering or even be implanted into the forming film or the substrate.

Various analysis techniques can be used to reveal information about the state of the plasma, the ablation process that created it and the ablated material. [88] Optical emission and absorption spectroscopy are well suited for characterization of the excited atoms, ions and molecules in the plasma. In laser-induced breakdown spectroscopy

(LIBS), the analysis of the laser generated plasma is used to determine the elemental composition of the material. [100–102] LIBS is for example used by NASA on the Mars rovers for elemental analysis. [103]

The temperature of the plasma can be approximated optically from the relative emission intensities of the spectral lines by using so called Boltzmann-plots or by measuring broadening of the individual lines. [104–106] The temperatures can be obtained only from relatively dense plasmas. As the plume expands and the particles are no longer interacting, the temperature is no longer defined. [107]

Time- and space-resolved imaging is a commonly used tool, which is especially powerful when it is coupled with spectroscopy. [97] Optical interferometry can be used to measure the density profiles of the plasma. [108–110]

Mass spectrometry can be used to identify the ionic species and the charged clusters and to measure their kinetic energies through time-of-flight (TOF) analysis. However, neutral species need to be ionized before the analysis. [111, 112] TOF measurements of the charged species can also be done with Faraday cups [113] and Langmuir probes [114].

Analysis of the laser generated plasma is of great interest in many fields including PLD, PLAL, X-ray and extreme ultra-violet generation [115, 116], laser ion accelerators [117], laser space propulsion [118] and laser ignition of fusion [119].

3.6 Ablation threshold

The discussion in the previous sections has covered various aspects of laser ablation and the different parameters that influence the process. To evaporate a material, the input of energy must exceed the binding energy of the material. Thus ablation thresholds can be expected to show predictable, material dependent behaviour. In femtosecond pulse ablation of oxide-materials F_{Th} was observed to depend on the band gap. [120] In nanosecond pulse ablation of metals the amount of evaporated atoms was found to agree well with the melting temperatures of the various metals at constant fluence, though F_{Th} values were not reported. [62]

The influence of wavelength on F_{Th} is not trivial as the different mechanisms can

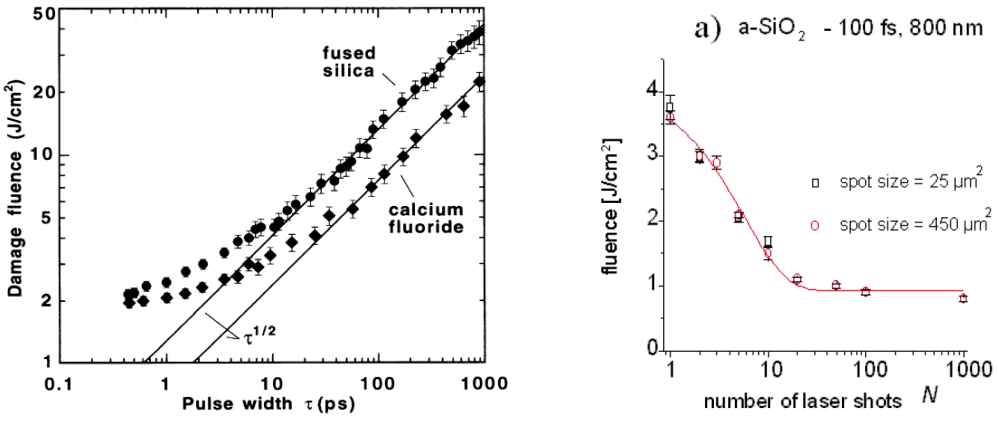

(a) (b)

Figure 3.7: (a) The ablation threshold fluence depends on the pulse duration τ. The dependence typically follows $\sqrt{\tau}$ at longer pulse durations, but as the absorption and ablation mechanisms change at shorter pulse lengths, for many wide band-gap insulators it approaches a constant. Picture taken from reference [121]. (b) Irradiation with sub-threshold pulses creates defects that lower the F_{Th} significantly. [122].[15]

have complex wavelength dependencies especially when shorter pulses are used.

The influence of the pulse length, τ, has been widely studied for many materials. [120, 121, 123–125] For nanosecond pulses, F_{Th} decreases as $\tau^{1/2}$ until τ_{e-p} of the material is approached (Fig. 3.7 (a)). For pulses shorter than τ_{e-p} the threshold approaches a constant value for most materials.

As previously discussed, even sub-threshold pulses can damage the material and create defects with long lifetimes, especially in dielectrics and semiconductors. In addition, above F_{Th} the surface after ablation is in most cases rough, which can change the absorption and the binding energy of the surface atoms. In most applications of laser ablation, the processed area of the material is irradiated several times and thus the interaction is no longer similar to what it is between the laser and a pristine material. The accumulating damage lowers F_{Th} for the subsequent pulses (Fig. 3.7 (b)) until the threshold saturates after a few tens or hundreds or pulses depending on the material and laser parameters. [122, 126, 127]

[15]Fig. 3.6 (a) reprinted with permission from [121] ©(1995) The American Physical Society. Fig. 3.6

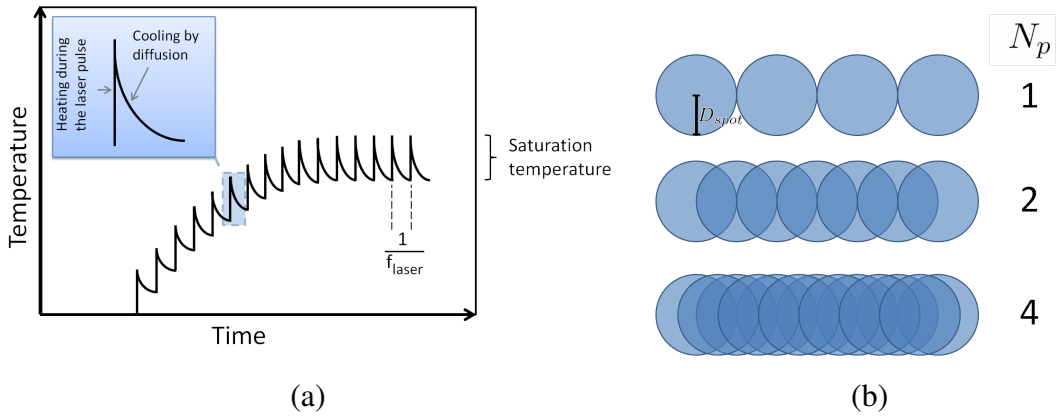

Figure 3.8: Visualization of the pulse overlapping N_p (a). Step-like heating by a high-repetition rate laser (b).

3.7 Laser ablation with high repetition rate lasers

With high repetition rate lasers the delay between the pulses hitting the same area gets so short that the dynamic effects can no longer be ignored. Defects with shorter lifetimes can influence the process and lower F_{Th}. In addition, each laser pulse will increase the local temperature. With low repetition rates, the irradiated area reaches the ambient temperature through heat diffusion before the next pulse arrives. For oxide materials, it was observed that F_{Th} is constant with repetition rates below 1 kHZ. [126] With sufficiently high repetition rates however, the temperature climbs in step-like fashion until a balance between input of energy and heat diffusion is achieved (Fig. 3.8 (a)). [128] The saturation temperature depends on the pulse energy, repetition rate and the rate of heat diffusion in the material. When the temperature rises, the rate of diffusion increases correspondingly as the temperature difference between the irradiated area and the surrounding material increases. If the surface temperature is above the melting temperature, evaporation of atoms further increases the cooling rate.

In experiments described in publications 1 and 2 the influence of the repetition rate was studied in the case of picosecond ablation of yttria-stabilized zirconium dioxide, YSZ. The ablated area was scanned continuously as described in [P1] and the measurements were made after the whole area was ablated several times. This was done to make

(b) reprinted from [122], with kind permission from Springer Science and Business Media.

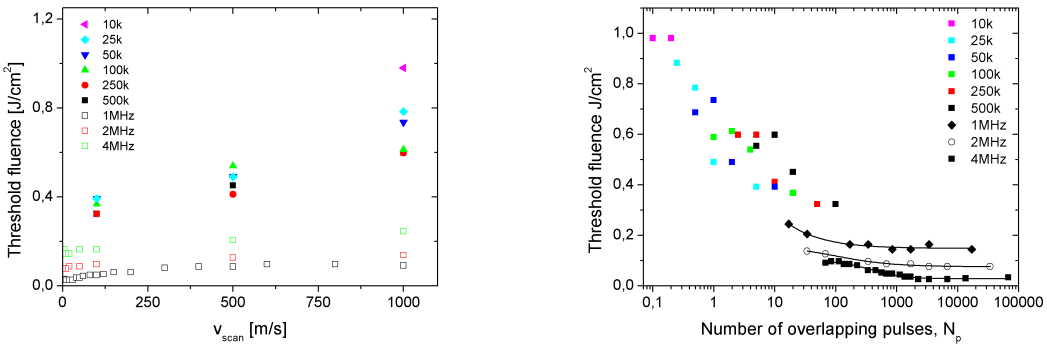

(a) (b)

Figure 3.9: The ablation threshold F_{Th} as a function of the scanning speed (a) and the number of overlapping laser pulses N_p (b). Increasing N_p lowers the threshold until a saturation region is reached at the equilibrium temperature.

sure that the contribution of the long life-time defects was included in the measured F_{Th} values and the observed behaviour was due to the increased temperature and possible short-life-time defects.

The ablation threshold was inspected as a function of the number of overlapping laser pulses, N_p, on a single scanning pass:

$$N_p = f_{laser}\frac{D_{spot}}{v_{scan}}, \tag{3.4}$$

where f_{laser} is the repetition rate of the laser, D_{spot} is the diameter of the laser focal point and v_{scan} is the speed at which the laser is scanned along the surface (Fig. 3.8 b).

The ablation threshold was observed to decrease as the repetition rate was increased from 10 kHz to 4 MHz (Fig. 3.9). Interestingly, the decrease of the threshold was observed already at values of $N_p < 1$. In this case the time between consecutive pulses is several tens of microseconds and significant heat diffusion over distances of several micrometers can occur. In the measurements D_{spot} was only 20 µm and thus the behaviour is attributed to heat diffusion. Another possible contributing factor is formation of short-lived defects.

In the megahertz repetition rate range F_{Th} was observed to saturate to a value that corresponds to approximately the same average power, suggesting that the vaporization

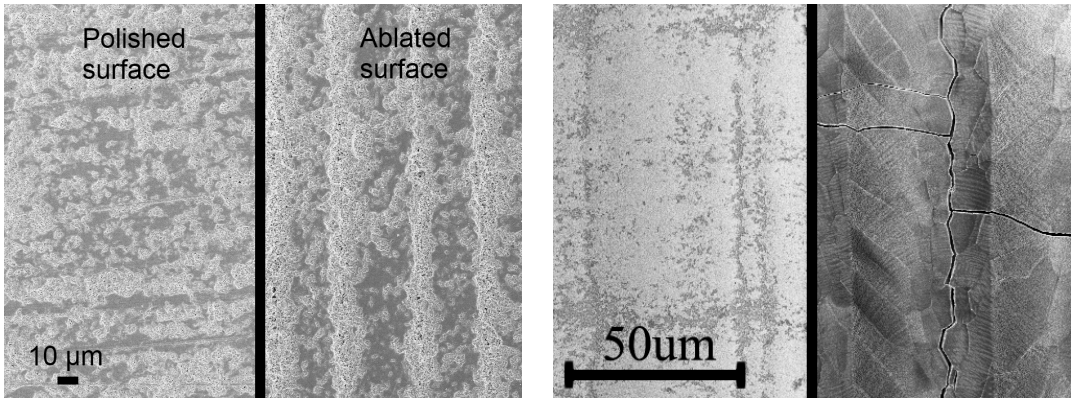

(a) (b) (c) (d)

Figure 3.10: The surface of the YZO target after ablation with low number of overlapping pulses shows no signs of melting (b) and (c) and is similar to the polished surface (a). The thermal nature of the saturation region with high N_p in Fig. 3.9 is evident from the surface that has molten and cracked during solidification (d).

mechanism has changed from ablation to thermal evaporation. The change in the ablation mechanism is observed in images of the ablated targets taken with a scanning electron microscope (SEM) (Fig. 3.10). Ablation with low N_p (Fig. 3.10 (b) and (c)) left the surface structure similar to a polished target surface (Fig. 3.10 (a)). After ablation in the saturation regime ($N_p \approx$14 000) with the repetition rate above 2 MHz, the surface had melted and cracked during solidification (Fig. 3.10 (d)).

The melting of the target is very local and is limited to the surface layer. The target surface is solidified between the laser scans and each sweep leaves a clearly identifiable track on the surface (Fig. 3.11 (a)). Closer inspection (Fig. 3.11 (c)) allows observation of small step-like structures along the scanning direction. This suggests that as the beam moves forward, only the small area directly beneath or very close to the pulsed laser beam is melted and the solidification takes place rapidly as the beam moves away.

Slightly higher pulse energy leads to ejection of droplets and exfoliation of the surface layer (Fig. 3.11 (b)). This indicates that the molten layer is very thin and suggests the possibility that the vaporization mechanism is actually pulsed ablation from a locally liquid surface rather than pure thermal evaporation.

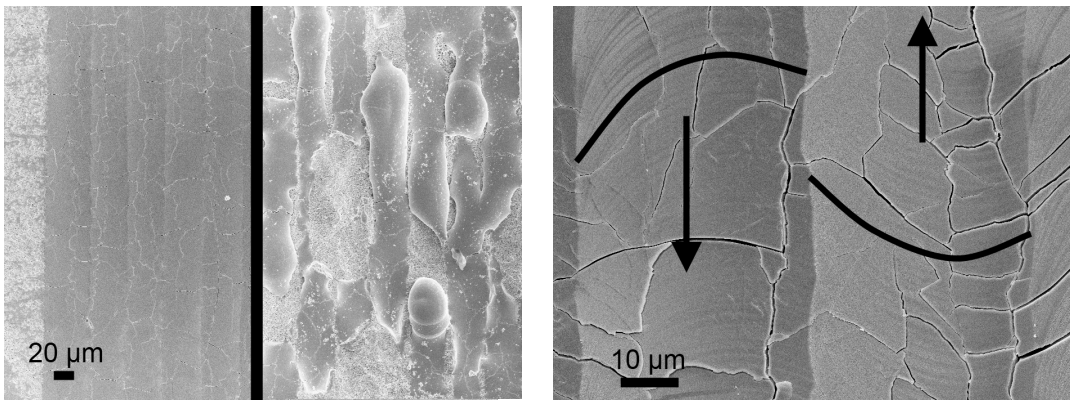

(a) (b) (c)

Figure 3.11: Locally melted YZO target solidifies between scanning sweeps leaving the scanning path clearly visible on the target surface (a). Too high pulse energies/average power leads to droplet ejection. Some droplets have solidified before ejection (b). This also shows the local nature of the melting as only the thin surface layer has melted. The scanning direction can also be observed from the curved ”solidification steps” (c).

Further results on the effects of the change in the ablation mechanism on the quality of the deposited films are presented in chapter 4.

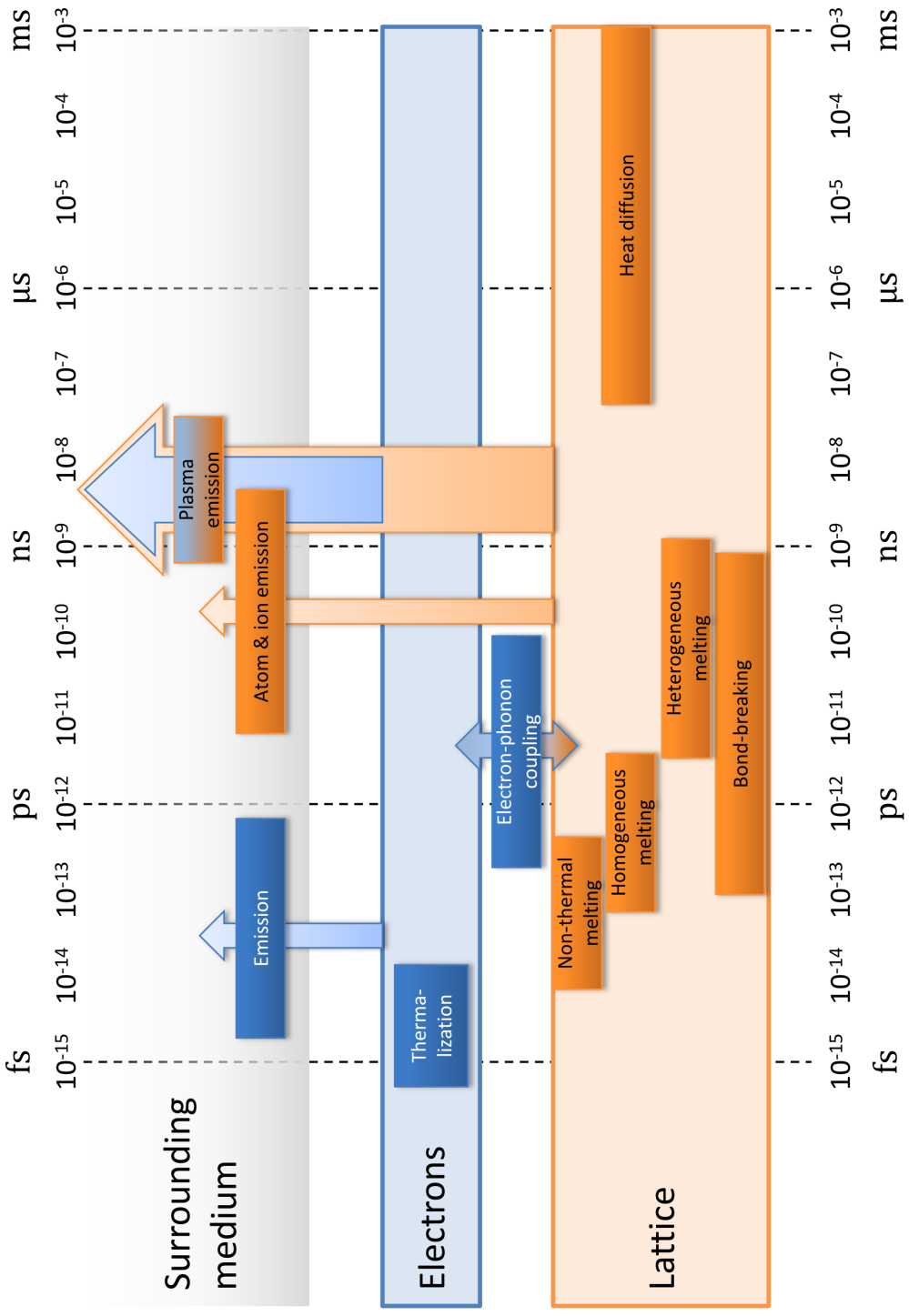

Figure 3.12: A summary of the timescale of the processes related to laser ablation.

Chapter 4

Pulsed Laser Deposition

In Pulsed Laser Deposition (PLD), laser ablation is used to deposit thin films under low-pressure conditions. The first experiments on PLD with ruby lasers were reported in 1965, only 5 years after the demonstration of the first laser [5]. During the following 20 years, many of the key features of PLD were demonstrated, including congruent evaporation and preservation of stoichiometry.[1] Though some important proof-of-concept level experiments were performed, the reported experiments were rather sporadic and closely followed the advances achieved in the development of lasers.

Especially important milestones were the development of reliable Q-switching and efficient frequency doubling in the 1970's, which allowed short pulses with high pulse energies and short wavelengths. In the early 1980's the number of research groups working on PLD steadily increased and results achieved with epitaxial semiconductor films were comparable to those achieved with molecular beam epitaxy (MBE). [131–134]

The versatility of the method and the sheer number of materials that can be deposited with PLD lead to a lack of common focus in the research, which slowed down the progress in the field. Things changed after successful fabrication of high-temperature superconducting thin-films by Dijkkamp and Venkatesan in 1987. [6] This started a boom in the research-field and lead to rapid progress of the technology.

The term *Pulsed Laser Deposition* is easily perceived as a name of a single technique,

[1] A good review of the history and development of PLD can be found *e.g.* in the reference [129]. General reviews can be found in references [129, 130].

though, in many ways it is a common denominator for a collection of several different techniques. PLD-methods can be classified by the laser pulse duration, the wavelength, the applied pressure range and, as shown also in this work, by the repetition rate of the pulses. Depending on the process parameters, PLD can be used to produce smooth or even epitaxial thin films, nanostructures or nanoparticles.

The straightforward operation of modern lasers makes working with PLD misleadingly simple. The lasers are often complex and sophisticated devices and the related processes are complicated, as described in the previous chapter.

PLD is an excellent method for the study and fabrication of novel and complex materials. However, despite the excellent results in deposition of various materials, the method has not yet been widely commercialized. One hindrance to commercialization is the fact that the material evaporated in laser ablation forms a strongly directed plume. This allows efficient collection of the material, but the films deposit only on small areas. In typical experimental setups this leads to non-uniform films. However, this issue is relatively easily solved as will be shown later in this chapter.

Possibly a larger obstacle in the way of commercialization of PLD is the lack of breakthrough applications. High-temperature superconductors are interesting materials, but they still require too low operating temperatures for applications that would require up-scaling of the fabrication methods.

This chapter starts with a brief comparison between PLD and other common thin-film deposition techniques, followed by a description of typical PLD systems and a discussion of the film growth mechanisms. The discussion started in the previous chapter on the impact of the pulse length on the ablation process is expanded with an inspection of its effects on the deposited films. PLD results achieved in this work with high repetition rate lasers related to publications 1 and 2 will be discussed and expanded with a discussion of methods for monitoring and optimization of film growth in sections 4.3-4.5.

4.1 Comparison to other thin-film deposition techniques

Due to the nature of the involved processes, PLD is a physical vapour deposition (PVD) method. The most obvious difference when compared to other common PVD-methods,

e.g. electron beam evaporation, sputtering or cathodic arc evaporation, is that the power source, the laser, is outside the vacuum chamber. This allows very simple chamber designs which enable the use of reactive gases that might damage complex power sources and mechanics.

A less obvious, but more profound difference to thermal evaporation methods, such as electron beam evaporation, is the approach to the delivery of the energy. In e-beam evaporation the whole target material is melted and subsequently evaporated from the molten state. In the case of compound materials, this leads to a different evaporation rate for each element in the compound, depending on their respective partial vapour pressures. Therefore, the resulting films are not stoichiometric without corrective measures. In PLD the energy is delivered locally during a very short pulse. As discussed in the previous chapter, the typical pulse lengths are shorter than or of the same order of magnitude as the characteristic heat diffusion times of materials. This leads to congruent evaporation of the material, which has been observed to transfer the stoichiometry of the complex target materials onto the formed thin films [6, 135–139]

During the early years of PLD, successful experiments were also performed with continuous wave (CW) lasers. [140–142] Though the results were good and often surpassed those achieved with *e.g.* electron beam evaporation, the research in this field all but stopped after the breakthrough of PLD. Only few reports have been published during the last few years. [143]. CW-laser evaporation allows the use of reactive gases, but unlike with PLD, the evaporated material consists almost solely of neutral atoms rather than ions. This can be an advantage for the deposition of some materials. However, the evaporation and deposition process does not necessarily transfer the stoichiometry of the target to the deposited films.

In deposition of semiconductors by PLD, the kinetic energies of the incoming particles are higher than in *e.g.* MBE. This allows the use of lower substrate temperatures. For example the heteroepitaxy of germanium is possible at a substrate temperature of 300 °C, whereas in MBE, the temperatures are typically higher than 700 °C. [144, 145] However, PLD has struggled to compete with the crystal quality enabled by the established epitaxial growth techniques. In addition, the possible advantages and improved flexibility over established manufacturing methods are not necessarily big enough to

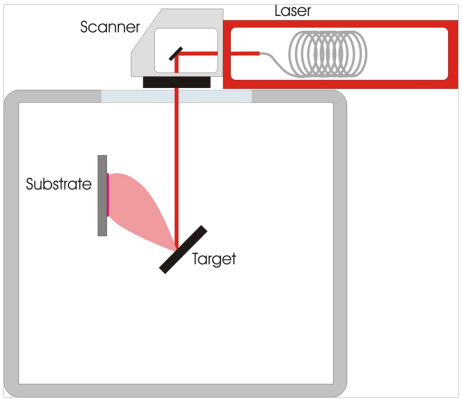

Figure 4.1: A PLD setup consists of the laser, the vacuum chamber, and the holders for the target and the substrate. Typically the surface of the target is raster-scanned for smooth ablation of the whole target surface. This can be done either by moving the target mechanically or by scanning the laser beam.

offset the risks related to migration to a new technique.

4.2 PLD systems

The key features of typical PLD systems are very similar. The system consists of a laser, a vacuum chamber, holders for the target-material(s) and holders for the substrates that the film is deposited on (Fig. 4.1). The equipment used in this work is described in publications 1 and 2.

Vacuum chambers

The pressure ranges used in PLD vary from ultra-high vacuum (UHV) levels applied in deposition of epitaxial films to the nearly atmospheric pressures applied in production of nanoparticles and nanotubes. Depending on the application, the chamber can also include gas feeds for inert or reactive gases. Therefore, it is understandable that the chambers and the required pumping systems vary from very expensive and complex to relatively simple and cheap.

The chamber needs at least one window for the laser and the window can be heated to

protect it from the depositing material that could absorb the laser power. Typical setups have several windows to allow *in situ* monitoring of the process.

Target holders

Laser ablation is typically carried out with pulses focused on a small spot on the surface of the target and thus, to avoid cratering, the beam is raster-scanned over the surface. This can be accomplished by moving the target, the beam or both. The motion of the target is typically done mechanically with mechanical feedthroughs or by vacuum compatible motors. The beam scanning is done by using a 1-, 2- or 3-dimensional mirror scanner or lenses. The target holders can also be designed to hold multiple targets that can be exchanged without breaking the vacuum to allow the deposition of multilayered films.

Another approach to avoid craters and droplets is to use molten targets, though this approach is limited to materials with low evaporation rates near their melting point under the applied pressure conditions (*e.g.* germanium). [144, 146]

Substrate holders

The substrate holders can be static, but homogeneous deposition on larger substrates typically requires controlled movement. In typical systems the target-substrate distance is adjustable to allow optimization of the energy of the arriving material. Depending on the application, the substrates can be at room temperature or at considerably higher temperatures. Similarly to the target holders, multiple substrate holders can also be used.

Lasers

Since the first experiments performed with a ruby laser, a wide selection of lasers has been employed in PLD. The most widely used lasers are the nanosecond pulse excimer lasers, with wavelengths in the ultra-violet (typically 157 nm – 351 nm). Due to their short wavelength, the light is efficiently absorbed by most materials. As gas lasers, the excimer lasers require careful maintenance to guarantee stable operation. The beam quality of excimer lasers is also another issue that requires careful control and monitor-

ing. Some work has also been done with CO_2 based gas lasers with wavelengths near 10 µm.

Solid-state lasers require less maintenance, but typically operate at longer wavelengths that are not absorbed as efficiently. The most commonly used solid-state laser material has been the Nd:YAG, which emits at a wavelength of 1064 nm. To improve the absorption, nonlinear crystals are often used to decrease the wavelength of the laser through second or third harmonic generation.

PLD experiments with femto- and picosecond pulses are typically carried out with solid-state lasers, *e.g.* Nd:YAG or titanium sapphire lasers. Some work has also been done with the fibre laser used in publications 1 and 2 and a free-electron laser. [147]

4.3 Film growth in PLD

The growth mechanisms of the thin films depend on the material system in question and on the thermodynamic conditions during the process. In particular, the energy of the incoming particles and the substrate temperature play an important role. [148] In PLD the particles are typically very energetic with kinetic energies up to several tens of electron volts. This allows deposition of dense, high-quality thin-films at lower substrate temperatures than is required in most other methods.

In addition to deposition of smooth films, PLD can be used to produce nanomaterials. One approach is PLD in high background pressures, which produces nanoparticles and nanotubes. Furthermore, it can be used to deposit high surface area films. Femtosecond laser ablation offers another possibility as it inherently leads to formation of nanoparticles.

Effect of background gas pressure

The high kinetic energy can lead to recoiling of the incoming particles (atoms, ions) from the substrate [97, 99], implantation of the particles into the substrate and sputtering of the substrate or the deposited thin-film [149]. The energy of the particles can be controlled by increasing the background pressure or the distance between the target and the substrate.

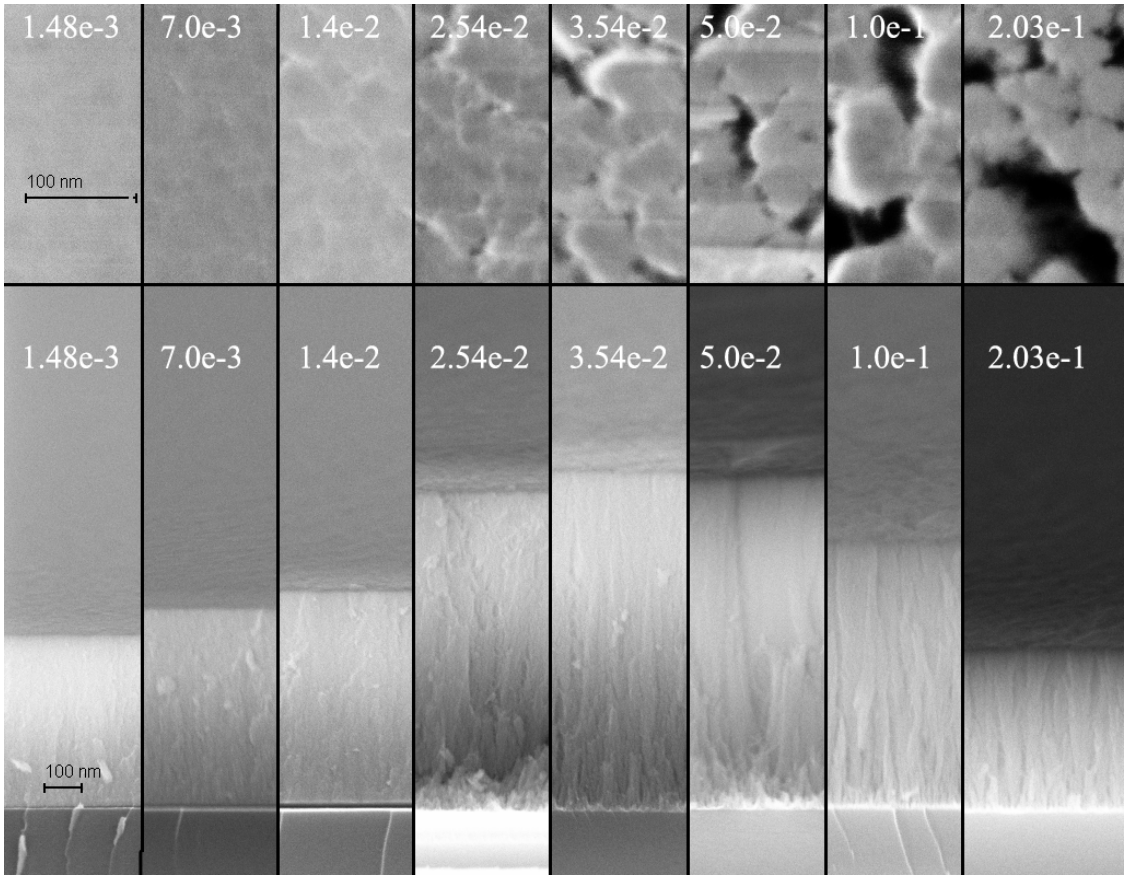

Figure 4.2: The increasing oxygen pressure slows down the particles in the plume, initially increasing the thickness of the grown YZO-films. This is caused by fewer particles recoiling away from the surface, reduced film-sputtering, increased incorporation of oxygen into the film and lower density of the formed film. The reduced density can be observed easily from the top-down perspective. At sufficiently high pressures the thickness of the film drops as fewer particles reach the substrate. The deposition time for all samples was 30 minutes. The pressure values in the picture are expressed in mbar.

At background pressures below 10^{-2} mbar the plume expansion is relatively unhindered by the background gas and is adequately described by the models of adiabatic expansion of a gas cloud into the vacuum. [130, 150] Higher pressures lead to increased collisions between the particles in the plume and the background gas, reducing the speed of expansion. The slightly decreased energy is typically observed as an increase in the growth rate of the film (Fig. 4.2). The increase can be attributed to fewer particles re-

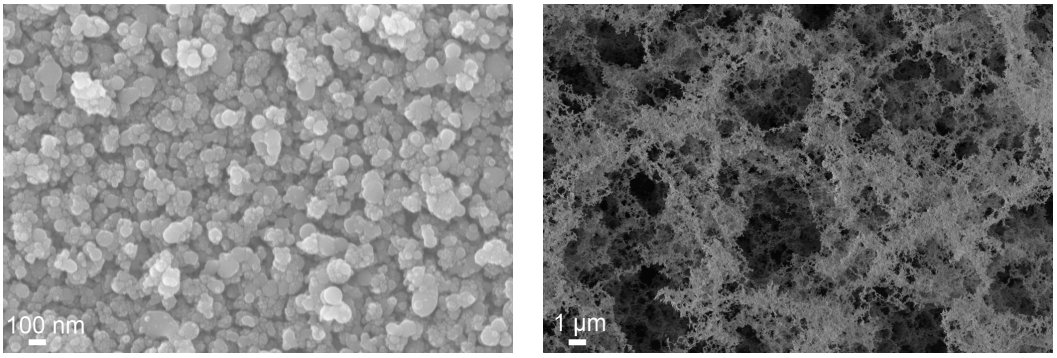

(a) (b)

Figure 4.3: PLD in high background pressures leads to formation and deposition of nanoparticles (a). With even higher pressures the slow nanoparticles form loose, foam-like deposits with very high specific areas suitable for catalytic applications (b). Titanium dioxide (a) and nickel (b) samples were both deposited with fibre laser PLD.

coiling from the substrate and reduced sputtering. With even higher pressures, the film thickness increases as the particle energy is no longer high enough to deposit as dense films as in vacuum. If the background gas is reactive, like oxygen in the case of zirconium dioxide (Fig. 4.2), the incorporation of gas can also lead to thicker films.

With pressures above 10^{-1} mbar the increased collisions of the particles with the background gas lead to diffusion of the material over a larger area, possibly away from the substrate. Therefore, the deposited films are thinner.[2]

Even higher pressures lead to formation of a "shock-front" at the plume-background gas interface and causes nucleation of nanoparticles (Fig 4.3 (a)). [97, 151–155] Increasing the pressure further slows down the nanoparticles and leads to deposition of foam-like structures with extremely high specific surface areas that are useful in *e.g.* catalytic applications (Fig. 4.3 (b)). [156, 157]

[2]Note that the films shown in Fig. 4.2 have been deposited with a high-repetition rate laser in the thermal evaporation mode (chapter 3, P1 and P2). However, the observations are similar to those obtained with nanosecond pulse excimer lasers [150] though the thermal evaporation mode itself in some respects is different.

Effect of the pulse length

PLD with nanosecond pulse lasers produces high quality films, but it requires precise control of the process parameters. The laser needs to be very stable and have sufficiently high beam quality. The surface of the target needs to be ablated evenly, yet the quality of the surface can still degrade during long depositions. Deviation from the optimal parameters can lead to production of droplets that deteriorate the quality of the film.

The ablation process with femtosecond pulses is almost free of thermal effects and thus is less prone to droplet formation. In addition, the surface quality of the target is higher after femtosecond pulse ablation, as shown by micro-machining studies. [58] It has indeed been shown that use of ultra-short pulses in PLD avoids the droplet problems, but unfortunately introduces a new problem: the evaporated material forms nanoparticles. [84, 85, 158–160]

The nanoparticles can be either evaporated directly from the material or formed through collisions in the dense plasma. In ablation with nanosecond pulses, the laser interacts strongly with the plume and dissociates the evaporated molecules and clusters. In the case of femtosecond (and in most cases picosecond) pulses the laser pulse is over before any significant ablation occurs. Thus, the formed nanoparticles remain intact and can serve as nucleation centres during gas expansion and increase in size. Nanoparticle creation is thus an inherent feature of ultra-short pulse PLD.

Improvement of the homogeneity of the film thickness

Due to the directed nature of the plume, the films are deposited over relatively small areas and have considerable thickness variation. In an effort to improve the film homogeneity over the deposition area, a simulation model for the deposition process and resulting film appearance was developed using Matlab®. The effective plume profile and the deposition rate were estimated from the deposited film thickness profiles. The simulated thickness profile was transformed into the visual appearance of the transparent film by calculating the reflection spectra at each point and then converting the spectrum into the RGB-coordinates[3] (Fig. 4.4 (a) and (b)). A sample deposited on a two-inch silicon

[3]The conversion to RGB(Red-Green-Blue) was made by the Colorlab Toolbox collected by the University of Joensuu Color Group and coded by Tuija Jetsu. `http://cs.joensuu.fi/colorlab_toolbox/`

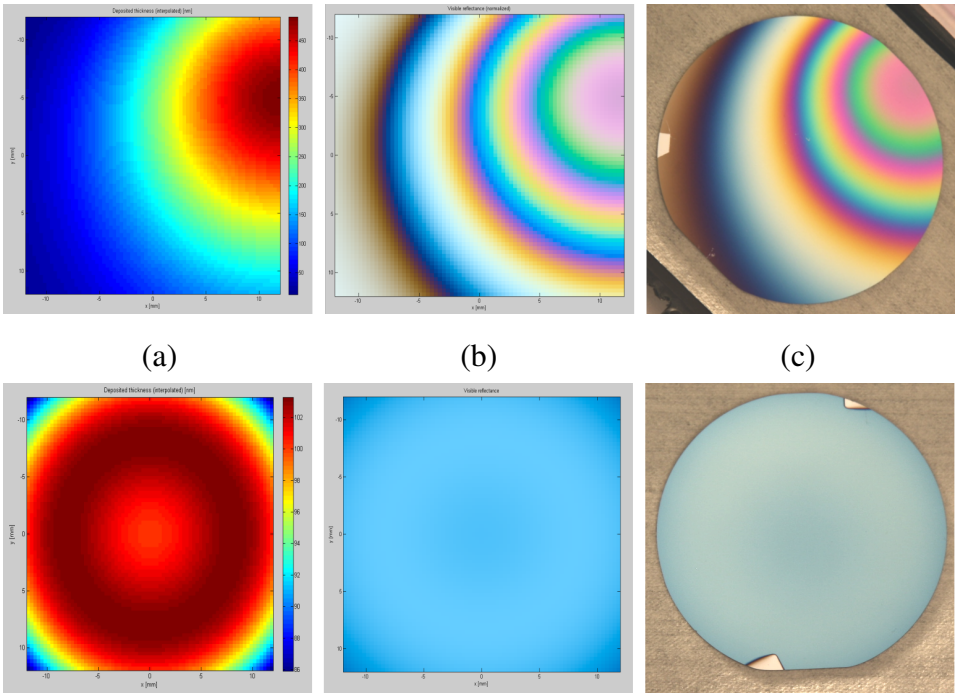

(a) (b) (c)

(d) (e) (f)

Figure 4.4: Results obtained with the model developed for the calculation of the deposited thickness profile (a) and the visual appearance of the film (b). A photograph of the real sample shows good agreement with the simulation results (c). The thickness (d), the simulated appearance (e) and the photo (f) for the optimized process.

wafer, with the simulated parameters was found to match the simulation well (Fig. 4.4 (c)).

The simulations were then used to optimize the rotation of the substrate in order to maximize the homogeneity of the film thickness and again, the simulation was found to agree well with the actual deposition. It correctly predicted both the optical thickness and the thickness profile of the film (Fig. 4.4 (d)-(f)). Thickness variation over the two-inch wafer was reduced from the initial 1600% down to 20%. The radius of the homogeneous area with less than 5% thickness variation was increased from 2 mm to 15 mm.

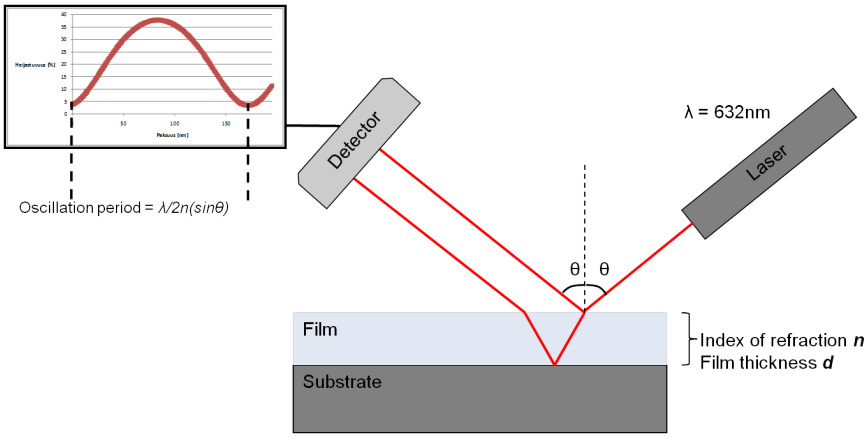

Figure 4.5: The growth of a transparent film can be monitored in real time by measuring the interference of a laser beam reflected from the surfaces of the substrate and the growing film.

Real-time monitoring of the film deposition

A real-time measurement system was built to complement the film homogeneity optimization (Fig. 4.5). [161] The thickness of a transparent oxide film can be measured during growth by measuring the reflectivity of the surface using a laser beam. The interference between the beams reflected from the surfaces of the substrate and the film causes the intensity of the reflected signal to oscillate as the film grows.

Comparison between the measurement and the simulated data allows the determination of the film thickness. In addition, the measurement can be used to monitor the film quality and changes in the growth rate. These can be caused *e.g.* by target deterioration or by absorption of the ablating laser power due to deposition on the chamber windows.

4.4 PLD with high-repetition rate lasers

Use of low-energy pulses with megahertz repetition rates for deposition of particle-free, high-quality films was first suggested by Gamaly *et al.*. [162, 163] Megahertz-range repetition rates lower F_{Th} and allow use of very low pulse energies as discussed in section 3.7 and publications P1 and P2. The decrease of the threshold was observed to saturate at high values of N_p (Fig. 3.9) and an inspection of the targets confirmed the thermal nature of the ablation process with repetition rates above 2 MHz (Fig. 3.10).

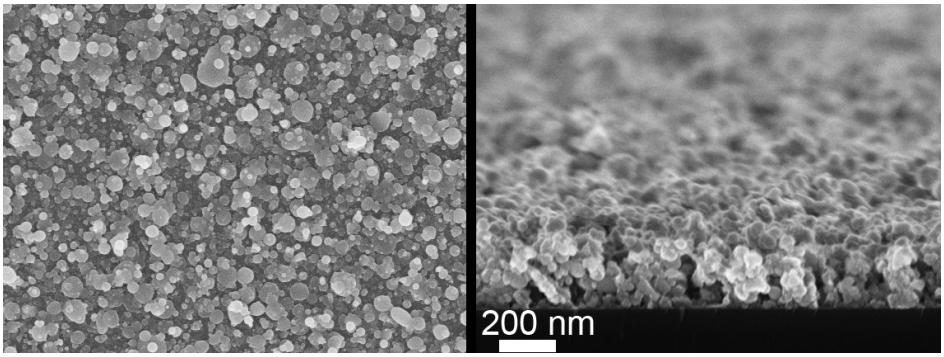

(a)

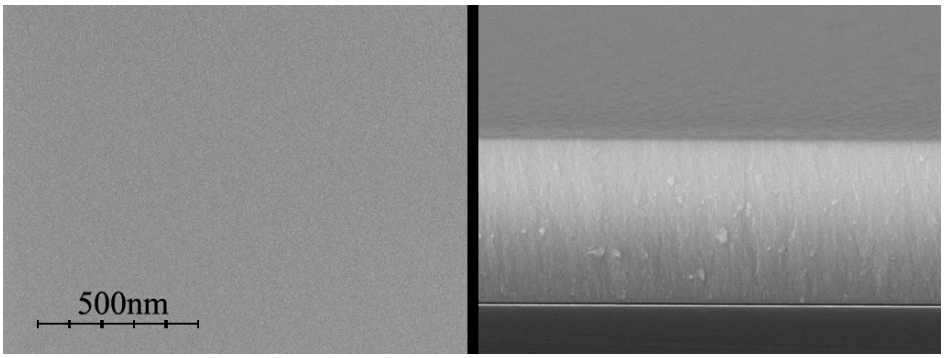

(b)

Figure 4.6: The films deposited with low N_p consist of nanoparticles (a). High N_p and repetition rate of 2 MHz or above changes the ablation mechanism into thermal evaporation, which yields smooth films (b).

The transition into the saturation regime was accompanied by a significant change in the deposited film quality. Picosecond pulse PLD of oxides (*e.g.* YZO and titanium dioxide, TiO_2) with repetition rates of 1MHz and below yields films that are similar to those deposited with femtosecond PLD (Fig. 4.6 (a)). [84, 85, 158–160]

The films deposited at higher repetition rates in the saturation regime are smooth and free from particles (Fig. 4.6 (b)). The notable change is caused by the local melting of the target due to accumulated heat. The ablation mechanism then changes from single pulse ablation to thermal evaporation and pulsed ablation from a liquid surface.

The saturation values for F_{Th} were 0.16 J/cm^2, 0.08 J/cm^2 and 0.03 J/cm^2 for 1 MHz, 2 MHz and 4 MHz, respectively (P1). It is worth noting that the average power in each case is almost identical. It was found for 2 MHz and 4 MHz repetition rates, that

Table 4.1: XPS measurements of YZO films

Sample	λ[nm]	f_{laser}[MHz]	N_p	$Y/(Y+Zr)\%$
Target				5.1%
1	1064	0.5	10	5.2%
2	355	0.5	10	5.8%
3	1064	1	17	5.3%
4	1064	4	68	4.8%
5	1064	4	13600	3.8%
6	1064	4	13600	4.2%

ablation with fluences above 0.1 J/cm^2 leads to the onset of single pulse ablation and deposition of particles even with N_p in the saturation regime. The saturation threshold for 1 MHz is above this value and thus single pulse ablation dominates and the purely thermal ablation regime is not reached.

The two ablation regimes can be distinguished by the visual appearance of the generated plume. The plume generated by ablation with low N_p has a bright, jet-like core similar to femtosecond pulse generated plasmas. In the thermal regime the plume is much broader and diffuse.

The high quality of the films is achieved at the cost of losing the stoichiometry. X-ray photoelectron spectroscopy (XPS) measurements of the target and the deposited films (Table 4.1, P2) show that the stoichiometry of the films deposited with low N_p have an yttrium and zirconium ratio close to that of the target. Films deposited in the thermal regime are zirconium-rich. Quite surprisingly, the films deposited with a shorter wavelength were found to be yttrium rich. All of the studied films were deposited with fluences very close to F_{Th}.

For PLD with nanosecond pulses it was reported that the Y/Zr-ratio is preserved only when the fluence is approximately two times higher than F_{Th}. [164] Deposition close to the ablation threshold led to deposition of yttrium deficient films. Purely thermal methods have been reported to cause yttrium losses of up to 30%. [165]

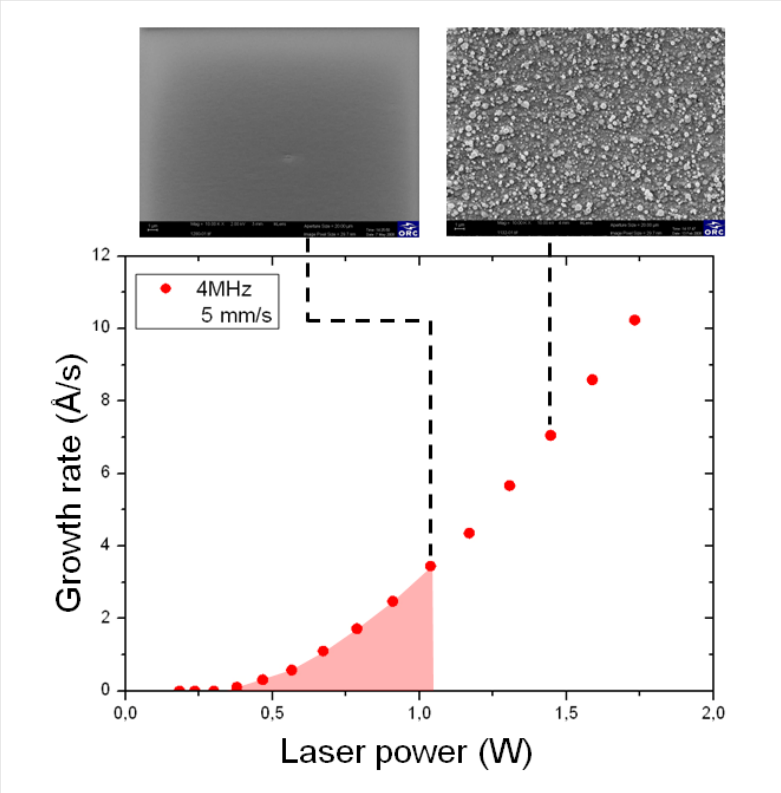

Figure 4.7: Growth rates for YZO measured at 4 MHz repetition rate. The shaded area marks the thermal evaporation zone that yields smooth films. The left SEM-image shows a smooth film deposited at 1.07 W and the right image shows a film formed of nanoparticle deposited at 1.46 W.

4.5 Upscaling of the deposition rates

The growth rates of the smooth films were studied as a function of the repetition rate. The scanning speed of the beam was kept constant, at 5 mm/s, corresponding to the thermal evaporation regime for megahertz-range repetition rates. For 4 MHz, the transition from thermal evaporation to pulsed ablation occurs at slightly above 1 W, corresponding to a growth rate of 3.5 $Å/s$. Figure 4.7 includes SEM-images of the films deposited in the different regimes.

Increasing the repetition rate to 20 MHz increases the growth rates already at lower powers by keeping the local temperature above the melting temperature more consis-

Table 4.2: Maximum deposition rates achieved for smooth YZO-films

Repetition rate	Maximum deposition rate [Å/s]	Optical power [W]
4 MHz	3.5	1.1
20 MHz	12	1.5
CW	10	2.0

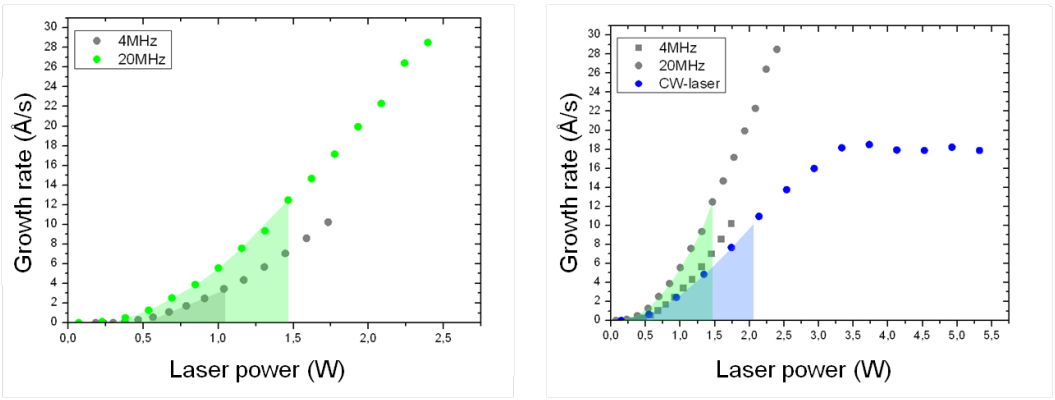

(a) (b)

Figure 4.8: Growth rates can be increased with higher repetition rate lasers. The maximum growth rate for YZO with a 20 MHz laser without deterioration of film quality was four times larger than for 4 MHz (a). In comparison to CW-lasers, 20% higher maximum growth rate can be achieved with 50% of the optical power with 20 MHz repetition rate (b).

tently (Fig. 4.8 (a)). In addition, as the pulse energy is lower, the transition to the particulate ablation regime does not occur until at approximately 1.5 W power, corresponding to a maximum growth rate of 12 Å/s.

For comparison, the deposition was tested with a CW-laser. The growth rates at low powers are only slightly below those achieved with 4 MHz (Fig. 4.8 (b)). When the power is increased above 2 W the films include small droplets and particles. It is noteworthy that the maximum achievable growth rate under these conditions was 20% lower (10 Å/s) when compared to the 20 MHz repetition rate. In addition, the required optical power to achieve the maximum rate was 50% lower for the pulsed laser .

Chapter 5

Pulsed Laser Ablation in Liquids

Pulsed laser ablation in liquids (PLAL) is a versatile and clean method for production of nanoparticle colloids. The produced particles are pure, very well suited for further functionalization [166, 167] and can easily be incorporated into *e.g.* polymer matrices [168–171]. The process can be run continuously and recently production rates of several grams per hour have been demonstrated. [172]

The interaction of laser pulses at a solid-liquid interface was first studied for modification of iron to create a surface-layer of metastable oxide phases. [173] PLAL for nanoparticle generation was first reported in the early 1990's. The first report was the observation of diamond particulates after pulsed ruby-laser irradiation of a graphite target in benzene. [7] Two other pioneering groups reported nanoparticle generation during the next year. [174, 175] Each of these reports has also been cited as the first PLAL experiment in various sources.

Typically PLAL-experiments are performed under ambient conditions (room temperature, atmospheric pressure) with the target immersed in static or flowing liquid, which is transparent at the applied laser wavelength. The liquid confines the expansion of the laser-produced plasma, which induces nucleation and growth of nanoparticles. The produced nanoparticles are typically electrically charged and thus form stable colloids in suitable liquids. The most extensively studied materials are the noble metals. However, experiments have been performed with most stable and solid elements either in elemental form or as part of a compound (Fig. 5.1).

In clear contrast to PLD research, in PLAL, there is no clear wavelength of choice. Most experiments are performed using lasers with visible or near-infrared wavelengths. [176] Recently some work has also been done with CW-lasers. [177]

Some of the more exotic PLAL experiments include ablation in high pressure liquids to produce carbon nanotubes [178] and ablation in supercritical liquids [179]. The results achieved in size-reduction and size-control of gold nanoparticles in supercritical water are especially promising. [180] Ablation in liquid helium was used to produce neutral atoms by ablating the produced nanoparticles and clusters with a second laser. [181] Ablation in liquid nitrogen was studied for production of titanium nitride and silicon nanoparticles. [182]

Due to the complex nature of the process and relative novelty of the technique, no theoretical model covers the whole process. Efforts to describe the different aspects of the process have been made with varying success and the general processes are relatively well understood for the most studied material systems. For the interested reader, there are several reviews available covering different aspects of the PLAL process and the achieved results. [176, 183–187][1]

This chapter will begin with a short comparison of PLAL with some other methods of nanoparticle fabrication, especially to the chemical synthesis of nanoparticles. The advantages and disadvantages of PLAL are described.

The discussion is then continued with the mechanisms of nanoparticle generation by laser ablation in liquids and behaviour of the particles in the liquids. The end of this chapter focuses on research towards combination of PLAL with chemical synthesis of luminescent gallium arsenide (GaAs) nanoparticles (publication 3) and single-step PLAL synthesis of gold nanoparticles with silica-shells (publication 4). Finally, the graphical summary of the timescales related to laser ablation from chapter 3 is extended to cover the timescales related to PLAL (Fig. 5.12).

[1]None of the reviews is comprehensive. For a good introduction to the benefits and prospects of the method reference [186] is recommended. For a review of the processes and theory of PLAL the suggested reference is [176] and finally for a review of the results achieved with PLAL references [176, 184, 187] are suggested.

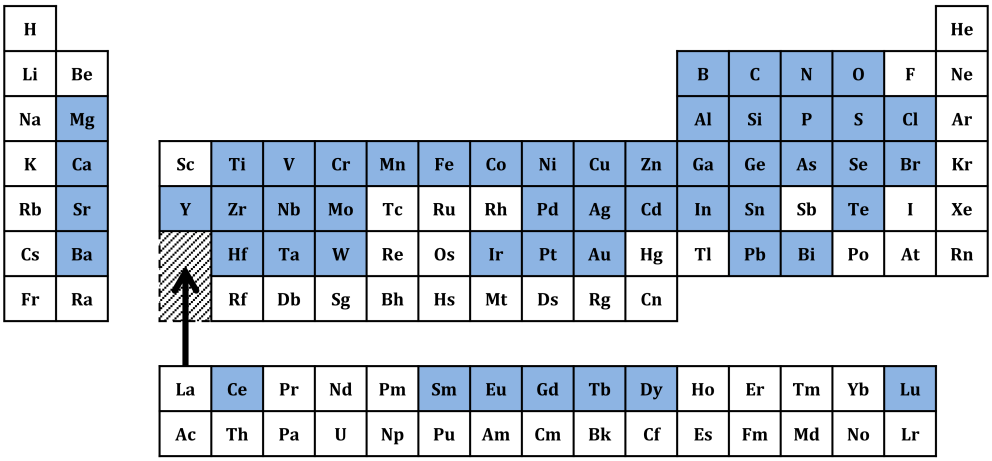

Figure 5.1: The periodic table of elements. Nanoparticles consisting of the elements that are shaded blue have been produced with PLAL, either in elemental form or as part of a compound. The figure is adapted from references [187] and [188], where the references for the related experiments can be found.

5.1 Comparison of methods to produce nanoparticles

There are various techniques for the production of nanoparticles. The techniques can be classified into top-down approaches, where macroscopic materials are divided into smaller particles, and bottom-up, where the nanoparticles are formed from atoms or molecules.

The top-down approaches are typically milling or fragmentation processes, where larger particles are ground to create smaller particles. The resulting particles are typically rather large with broad size distributions. Other examples of top-down methods are laser fragmentation and production of nanodiamonds in explosion chambers.

The bottom-up approaches include various heat-induced gas phase techniques, where the heat can be delivered *e.g.* by a flame, plasma, laser or electron beam. The liquid phase methods are typically chemical in nature.

Chemical synthesis of nanoparticle solutions

The prevalent method for preparation of nanoparticle solutions is chemical synthesis from precursor molecules. The method enables excellent control of the nanoparticle size and size distribution, which are typically much harder to control in PLAL. This makes chemical synthesis the method of choice for applications that require monodisperse nanoparticles. The production rates achievable through chemical synthesis are considerably higher than those reachable with currently available PLAL systems.

The largest pitfall of the method lies in the precursor chemicals which can be toxic and detrimental for the intended application. It can be very difficult and time consuming to remove these residues from the nanoparticles. [189, 190] In addition, the stability of the nanoparticle-colloids produced chemically is typically achieved through stabilizing surfactants and ligands, which can hinder further functionalization of the particles.

In PLAL, the ability to produce nanoparticles directly from the desired compounds allows production of pure nanoparticles.[2] The ability to produce nanoparticles that are stable due to their electrical charge in carefully selected solvents removes the need for stabilizing agents and makes particles produced by PLAL especially suitable for further functionalization. [166, 167] It has also been shown that PLAL generated nanoparticles incorporate easily into polymer matrices. [168–171] Furthermore, a wider variety of materials can be produced with PLAL and the raw materials are typically an order of magnitude cheaper than the precursor chemicals. PLAL can also be adapted for continuous production, whereas chemical synthesis is typically a batch-process.

Though the size control with PLAL is not up to par with chemical synthesis, the average size and the width of the size-distribution of nanoparticles produced in PLAL can be controlled and improved by surfactants [191], laser fluence [192], choice of solvent [193], wavelength [194] or by quenching the growth by conjugating molecules in liquid flow [195]. Another approach to produce nanoparticle-solutions with pulsed lasers is laser fragmentation. [180, 196–198] In this method, a solution of larger clusters is fragmented into nanoparticles. The two approaches can be used in combination to control

[2] The interaction of the liquid with the laser, the produced free ions and atoms and the laser-induced plasma can potentially lead to production of undesired compounds in certain material systems and thus great care needs to be taken during the analysis of the produced solutions.

the size-distribution of PLAL-produced nanoparticles. [199, 200]

Flame spray pyrolysis

Flame spray pyrolysis is a continuous process capable of producing very high quantities of nanoparticles rapidly. The method can be used in ambient conditions and is already implemented into mass production in *e.g.* paper mills. The nanoparticles are produced into an aerosol and this makes the method more suitable for deposition directly on the desired substrate than preparation of transferable nanoparticles.

Similarly to PLAL, the size distribution is wide and in addition, size control is inefficient and typically based on selection of suitably sized particles. The raw materials in flame pyrolysis need to be soluble and thus the selection is more limited than in PLAL. The production of nanoparticles directly into air creates an occupational hazard that is mostly avoided in synthesis in liquids.

5.2 Pulsed laser ablation in liquids

Progression of the ablation process in a liquid

The initial stages of the ablation process are similar to those described in chapter 3 and lead to the formation of a plasma. Absorption and non-linear effects in the liquid need to be taken into account especially in the case of femtosecond pulses or slightly absorbing liquids. [201]

Addition of a liquid complicates the process in many ways. First, the liquid confines the laser-produced plasma and strongly limits its expansion. Second, the sudden expansion of the plasma and (super-)heating of the liquid can lead to the formation of a shock wave and a bubble into which the plasma then expands (Fig. 5.2 (2)). [202, 203] The confined expansion and the rapid cooling of the plasma enhance nanoparticle nucleation (Fig. 5.2 (3)). Some of the formed nanoparticles, atoms and ions can escape from the bubble into the liquid, but most of the particles are trapped within. [204]

The eventual collapse of the bubble quenches the nucleation and growth of the nanoparticles (Fig. 5.2 (4)), but also enhances the production of agglomerates. [205]

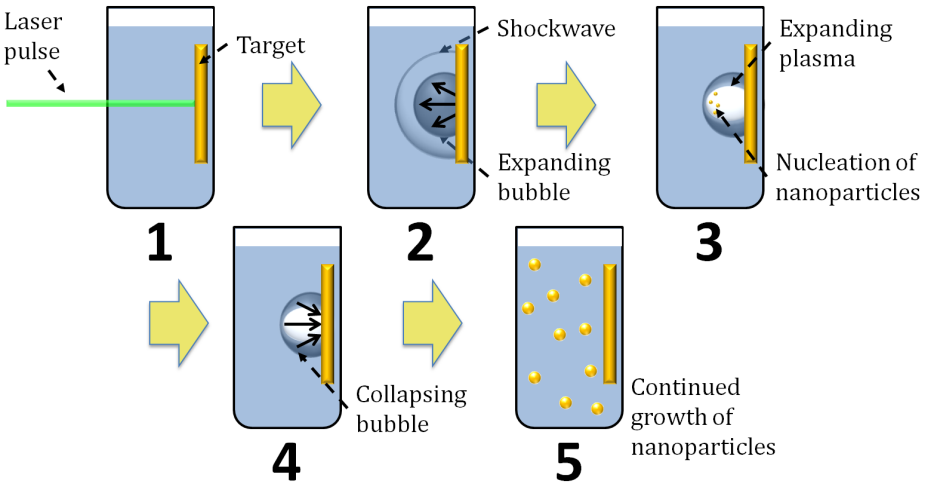

Figure 5.2: The simplified progression of a PLAL-process. Laser ablation generates (1) a hot plasma which causes a shock wave and an expanding bubble (2) through phase explosion or cavitation. Plasma then expands into this bubble (3), and rapidly cools down which causes nucleation of nanoparticles. The collapse of the bubble (4) quenches the nucleation process and releases the particles into the liquid (5). In the liquid the particles continue to grow through the condensation of atoms and ions released into the liquid during ablation or through the incorporation of smaller nanoparticles.

In the collapse, the temperature and the pressure are again increased close to the conditions of the initial, laser-induced plasma, which can cause cratering of the target. [206] The collapse can cause a new shock wave and another, albeit smaller, bubble. [202–204] The number of oscillations of expanding and collapsing bubbles depends on the pulse energy, the size of the ablated area and the properties of the liquid. The bubble dynamics and the high energies related to the collapse of the bubble can have a significant impact on the properties of the produced nanoparticles. [203, 205] In the case of higher repetition rate lasers, the bubbles can limit the productivity of the method by scattering the laser pulses. [207]

After the collapse of the bubble, the nanoparticles are released into the liquid. The growth continues for several seconds by condensation of ablated atoms and ions and possibly by Ostwald ripening as smaller particles are incorporated into larger ones. [191, 195, 208]

Because the plasma expansion takes place within the bubble and the surrounding liquid is pushed away, the reactions in the plasma and the nucleation occur almost solely between elemental species that originate from the target. However, in the initial phases of the process, some molecules from the liquid can be caught inside the plasma and the forming bubble. This can lead to the inclusion of the elements present in the solvent into the nanoparticles as impurities, especially if the elements are reactive and readily form compounds with the elements present in the target.

Most of the interaction between the nanoparticles and the solvent occurs after the bubble has collapsed. Possible surfactants and ligands in the solvent attach to the nanoparticles on a sub-second timescale, which allows size tailoring by performing PLAL in a flow-chamber and controlling the time-delay of the addition of the surfactants. [195] Chemical reactions between the nanoparticles and the liquid *e.g.* oxidation occur at varying rates depending on the materials in question.

During the ablation process the emitted, reactive material is confined close to the target surface, and thus the target related effects like redeposition, sputtering and fragmentation are enhanced, especially during the bubble collapse. This increases the ablation rate compared to ablation in a gas atmosphere or vacuum. In addition, the laser can decompose the molecules of the liquid, creating reactive species. The interplay of laser activation and chemical etching is used in laser-induced etching [209] and laser-induced backside wet-etching (LIBWE) [210].

5.3 Bubble dynamics

The dynamics of cavitation bubbles and laser-induced bubbles have been studied extensively. [211, 212] The bubbles formed in PLAL differ from the ideal, spherical bubbles formed within a liquid in a few important ways. First, the bubbles are attached to the target surface. Therefore the bubbles are hemispheres and collapse towards the surface. Second, the bubble is not empty or filled with vapour of the liquid, but holds the energetic plasma in the initial stages and a gas-nanoparticle mixture during the collapse. Third, a high-repetition rate laser can influence the bubble dynamics due to ablation by subsequent pulses or by interacting with the material inside the bubble. [213]

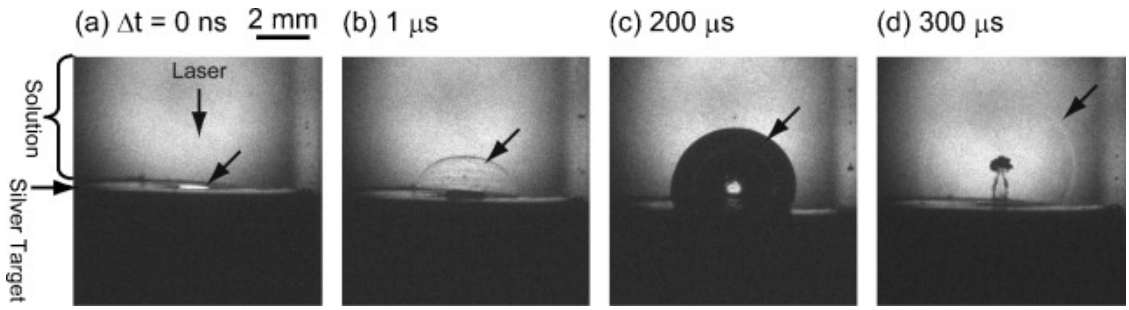

Figure 5.3: Shadowgraph images with 10 ns resolution show the bubble dynamics during laser ablation in liquid. The emitted shock wave can be seen in picture (b). [194][4]

The role of the bubble dynamics in PLAL have been studied by emission spectroscopy [214], shadowgraphy [202, 203, 215], light scattering [204] and small angle x-ray scattering [205, 216], but more work is required to fully understand the influence of the bubble dynamics on the properties of the produced nanoparticles. Many of the studies focusing on the dynamics of the bubbles have been done with high pulse energies and fluences well above F_{Th}, therefore it is important to keep in mind that the processes during ablation close to F_{Th} can be somewhat different.

In addition, when using very high repetition rates, such as those in publication 3, each pulse will not form an individual bubble. Instead, the ablation from subsequent pulses occurs into the bubble formed by previous pulses and the bubble dynamics become much more complex. [213]

Laser ablation causes emission of two shock waves, one into the liquid (Fig. 5.3 (b)) and one into the target material. [217] In water, the shockwave can initially expand at speeds in excess of 2500 m/s. [202] When the laser is focused directly into the liquid, as in laser-induced bubble generation, the shock wave dissipates a considerable fraction of the total absorbed laser pulse energy. [218] In PLAL, however, the laser pulse is first absorbed by the solid target and the shock wave is a consequence of the ablation and the formation of the plasma. Therefore, the results and conclusions are not directly transferable.

[4]Reprinted from Applied surface science, Vol. 254, T. Tsuji, D. Thang, Y. Okazaki, M. Nakanishi, Y. Tsuboi and M. Tsuji, "Preparation of silver nanoparticles by laser ablation in polyvinylpyrrolidone solutions," pp.5224-5230, Copyright (2008), with permission from Elsevier

The expansion of the cavitation bubble is slower than the shock wave (Fig. 5.3 (c)) and a simple estimation for the radius of the bubble, $R(t)$ can be calculated by the Rayleigh-Plesset equation [211]:

$$R(t)\frac{d^2R(t)}{dt^2}+\frac{3}{2}\left(\frac{dR(t)}{dt}\right)^2=\frac{1}{\rho_l}\left(P_B(t)-P_\infty-\frac{2\sigma}{R(t)}-\frac{4\eta}{R(t)}\frac{dR(t)}{dt}\right), \tag{5.1}$$

where P_∞ is the liquid pressure at infinity, σ is the surface tension of the liquid, ρ_l is the density of the liquid and η is the viscosity coefficient of the liquid. The driving force of the expansion is the bubble pressure $P_B(t)$ induced by the expansion of the plasma.

The Rayleigh-Plesset equation does not take into account the possible thermal effects or the fact that the bubble is not empty. In addition, it works well only for expansion speeds well below the speed of sound in the liquid. However, it fits experimental data relatively well and can thus be used to estimate the energy and the oscillation time of the bubble. [176]

The speed of the expansion of the laser generated plasma into vacuum is typically tens of kilometres per second. [60–62] The initial expansion into the liquid is also very fast, as evidenced by the emitted shock wave. The emission of sound becomes a significant energy-loss mechanism for a bubble when its expansion speed approaches or exceeds the velocity of sound in the liquid. Therefore, the use of the Rayleigh-Plesset equation becomes questionable. Sound emission is incorporated into the slightly more complex Keller-Miksis equation [219, 220]:

$$\begin{aligned}\left(1-\frac{1}{c_l}\frac{dR(t)}{dt}\right)\rho_l R(t)\frac{d^2R(t)}{dt^2}+\frac{3}{2}\left(\frac{dR(t)}{dt}\right)^2\rho_l\left(1-\frac{1}{3c_l}\frac{dR(t)}{dt}\right)\\ =\left(1+\frac{1}{c_l}\frac{dR(t)}{dt}\right)[P_B(t)-P_\infty]\\ +\frac{R(t)}{c_l}\frac{dP_B(t)}{dt}-\frac{4\eta}{R(t)}\frac{dR(t)}{dt}-\frac{2\sigma}{R(t)}\end{aligned} \tag{5.2}$$

where c_l is the speed of sound in the liquid.

Typically the life-time of the bubble is from 100 microseconds to a few hundred microseconds. [220] The bubble life-time can be considerably shortened in higher pressures. [203]

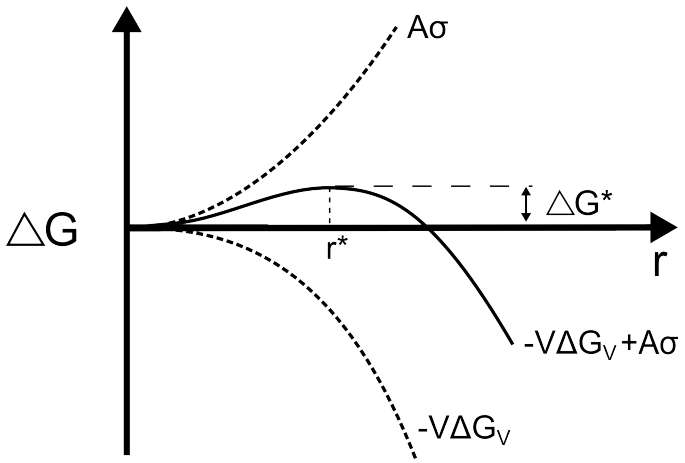

Figure 5.4: The free energy related to homogeneous nucleation of nanoparticles. The energy released in the formation of a particle ($-\Delta G_v^*$) is offset by the energy required to form its surface ($A\sigma$), creating an energy barrier ΔG^*. Thus particles below the critical size r^* are not stable and will dissolve.

5.4 Nucleation of nanoparticles

Nanoparticles can be formed from vapour or from atoms dissolved in a liquid. In either case the basis of the thermodynamical model used to describe the process of nucleation and subsequent growth is similar. A prerequisite for the nucleation is that the system is supercooled (vapour) or supersaturated (vapour or liquid). Formation of nanoparticles by PLD takes place in the vapour phase, but in PLAL the nucleation occurs primarily in the vapour phase, but the growth continues in the liquid.

The change in the Gibbs free energy, ΔG, associated with the nucleation of spherical nanoparticles of radius r is

$$\Delta G = -\frac{4\pi}{3} r^3 \Delta G_V + 4\pi r^2 \sigma, \tag{5.3}$$

where ΔG_V is the energy released in the formation of the particle per unit volume and σ is the energy per unit area required to form the interface between the particle and the surrounding medium, *i.e.* the surface of the particle. The surface tension of the bulk material can typically be used as σ for clusters larger than few tens of atoms.

Small clusters have a very high ratio of surface atoms and therefore the clusters are

not stable (Fig 5.4). The limit of stability can be calculated from the condition

$$\frac{d\Delta G}{dr} = 0, \tag{5.4}$$

to obtain the critical radius r^*

$$r^* = \frac{2\sigma}{\Delta G_V}, \tag{5.5}$$

below which the particles are not stable and will tend to dissolve. The energy required to form a nanoparticle of the critical size is ΔG^*

$$\Delta G^* = \frac{16\pi\sigma^3}{3\Delta G_V^2}. \tag{5.6}$$

In thermodynamical equilibrium the probability of nucleation, P^* for nanoparticles of the critical size can be estimated on the basis of the height of the energy barrier ΔG^* and the temperature T

$$P^* \propto e^{(-\Delta G^*/k_B T)}. \tag{5.7}$$

The rate of nucleation can be approximated from the Zeldovich-Raizer theory [221,222] which has been applied to model the formation of cosmic dust during vapour expansion after collisions between large meteorites and planets without atmospheres. The theory was adapted for the problem of nanoparticle formation in laser ablation plumes by Luk'yanchuk *et al.*. [223] This reference is highly recommended for a reader interested in a detailed discussion about the problem.

The rapid expansion and cooling of the ablated material leads to (super)saturation in the vapour, and the nucleation of the nanoparticles begins. Due to the formation of the Knudsen layer, the plasma produced in laser ablation into vacuum can be considered to be in thermal equilibrium. The assumption of thermal equilibrium is even more justified under the additional confinement induced by a surrounding medium, be it vapour or liquid. The equilibrium can break down in the later stages of ablation into vacuum as the particles in the rarified plume no longer interact.

The rate of nucleation can be estimated by assuming that the nucleation process follows the adiabat between the vapour and the liquid phase.[5] It is proportional to

$$\frac{dN}{dt} \propto exp\left(-\frac{16\pi\sigma^3 m^2}{3k_B^3 q\rho_l}\frac{T_{eq}}{T_v(T_{eq}-T_v)^2}\right), \tag{5.8}$$

where N is the number of nuclei in the vapour, T_v is the vapour temperature, T_{eq} is the equilibrium temperature along the adiabat, q is the heat of vaporization of the nucleating material, m is the atomic mass of the nucleating species, ρ_l is the density of the liquid phase and k_B is the Boltzmann constant.

The growth of the formed nuclei depends on the prevailing conditions. If the growth is limited by diffusion of atoms from the surrounding medium, the size distribution of the particles gets narrower during the growth. On the other hand, if the growth is governed by surface processes, *i.e.* reaction kinetics, the size distribution gets broader. In the initial nucleation and growth stage in the dense laser generated plume or plasma the nanoparticles are very hot. While atoms are deposited on the surface of a nanoparticle, some atoms are evaporated from the surface. Therefore this stage is controlled by the kinetics between condensation and evaporation of the atoms. The rate of growth of a nanoparticle with g atoms can be estimated by

$$\frac{dg}{dt} = \pi r^2 \rho_N v(T_v)\left[1 - exp\left(-\frac{q(T_{eq}-T_v)}{T_v T_{eq}}\left(1-\frac{r^*}{r}\right)\right)\right], \tag{5.9}$$

where ρ_N is the number density of atoms in the vapour phase and $v(T_v)$ is the mean velocity of the atoms in the vapour.

In the case of ablation into vacuum the growth of the nanoparticles is quenched when the plume has expanded so much that the vapour species no longer interact. When a background gas confines the expansion the growth continues until the vapour is no longer saturated.

The case of ablation into liquids is much more complicated. First, the confinement by the bubble can sustain higher density in the vapour phase and thus prolong the nucleation and growth phase. Second, the expansion and the collapse of the bubble controls the thermodynamic conditions in the vapour. The growth of the nanoparticles can be quenched

[5] Though it might be obvious to the reader, it should be emphasized that the nucleated particles are in liquid phase initially.

and restarted by the bubble collapse and rebound, respectively. After the nanoparticles and the remaining vapour are released into the liquid, the nanoparticles enter a diffusion limited growth which can narrow the broad size distribution created during the initial growth phase.

Therefore, from a thermodynamic viewpoint, to grow nanoparticles with a narrow size distribution by PLAL it would be beneficial to limit the life-time of the bubble, allowing only nucleation of the particles, and subsequently have the growth take place in the liquid. In the case of ablation of silicon into vacuum, the nucleation was estimated to occur in a few microseconds and the nucleation was quickly quenched due to the rapid expansion of the plasma. [223] The formed particles are therefore very small ($\approx$1.5 nm) and the size distribution is narrow.

However, the PLAL process is complicated and the bubble dynamics can cause rapid agglomeration and coagulation not predicted by the simple thermodynamic treatment. The nucleation time estimate is two orders of magnitude shorter than the reported life-times of the bubbles in PLAL. Only very recently, groundbreaking experiments have been able to study the processes within the bubble. [205, 216]

Two other features of laser ablation affect the size distribution. First, the plume is inhomogeneous. The differences in the density and the temperature of different plume regions cause different nucleation conditions and thus different critical nuclei sizes, and furthermore the growth conditions are different. Second, the charged species behave differently from the neutral atoms considered here.

5.5 Nanoparticles in the solvent

After the nucleation and initial growth in the plasma and in the bubble, the nanoparticles are released into the liquid. As already mentioned, the particles can grow by condensation of atoms and coalescence of smaller clusters. [195] The particles produced with PLAL tend to be electrically charged which leads to stable nanoparticle colloids after the initial coalescence.

In a study of PLAL-produced gold nanoparticles in water it was found that the gold surfaces are partially oxidized, which can be the cause of the charge on the surface of the

particles. [224] The addition of salts increases the amount of free charges in the solvent and it was found to decrease the initial coalescence, which led to considerably smaller nanoparticles.

Stabilization through electrostatic repulsion leaves the surfaces of noble metal particles reactive, which enables functionalization by conjugation of molecules. [166, 167]

Zeta-potential

The charged particle surface attracts the opposite charges creating an electrical double layer. The ions closest to the surface move with the particle and form a strongly bound Stern layer. The Coulombic attraction is masked further away from the surface and ions further than the so-called slipping plane do not move with the particle. The potential between the slipping plane and the bulk of the liquid is called the zeta-potential, ζ. [225, 226] The particles can be considered to be stable due to electrostatic repulsion when the zeta-potential is above 35 mV or below -35 mV.

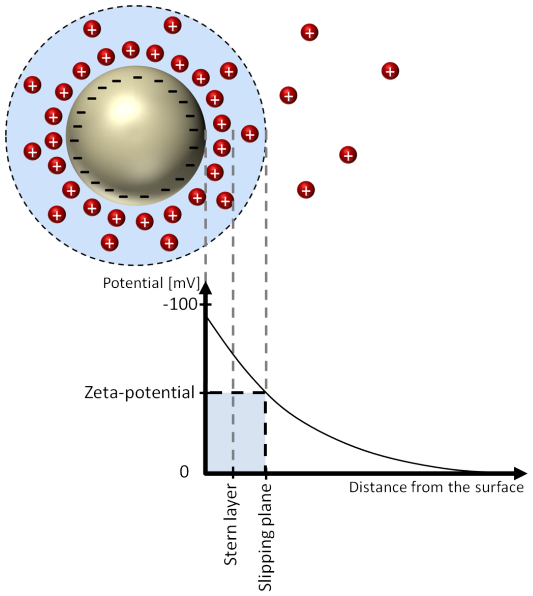

Figure 5.5: The zeta-potential is defined as the potential between the liquid and the slipping plane surrounding the charged particle. Adapted from reference [225].

The zeta-potential is strongly dependent on the pH of the solvent. Typically, the potential is more negative in alkaline solutions and more positive in acidic solutions. When the pH is adjusted continuously, the zeta-potential changes and typically goes to zero at the pH corresponding to the so-called isoelectric point and changes sign thereafter.

The charged particles can be controlled by electric fields and deposited through electrophoresis. This has been demonstrated by coating *e.g.* electrodes and stents with

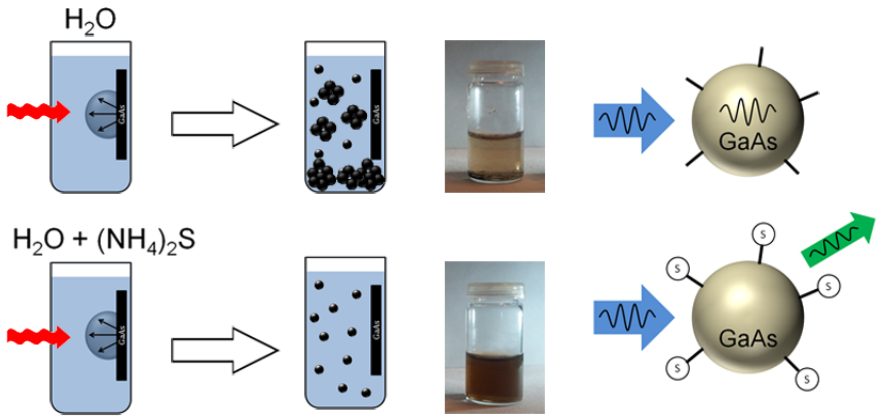

Figure 5.6: Laser ablation of GaAs in water leads to formation of large, oxidized clusters that rapidly form a sediment at the bottom of the container. Addition of small amounts of ammonium sulphide passivates the surfaces of the nanoparticles. Nanoparticles deposited from the stable and passivated solutions emit visible photoluminescence.

nanoparticles produced by PLAL. [227,228] The electrophoretic velocity v_E under electric field E is:

$$v = U_E E, \tag{5.10}$$

where U_E, is the electrophoretic mobility, which can be calculated from the Henry equation [229]:

$$U_E = \frac{2\varepsilon_r \varepsilon_0 \zeta f(\kappa a)}{3\eta}, \tag{5.11}$$

where ε_r is the relative dielectric constant of the solvent, ε_0 is the dielectric constant of vacuum, η is the viscosity of the solvent and $f(\kappa a)$ is Henry's function. The exact value of $f(\kappa a)$ depends on the size of the particles and on the concentration of electrolytes in the solvent. For nanoparticles, $f(\kappa a) \approx 1$ is typically a good approximation.

5.6 Production of GaAs nanoparticles

In the previous sections the unique features of PLAL have been described. The nucleation of the nanoparticles inside an expanding plasma and the bubble void of the liquid enables production of pure nanoparticles. The freshly nucleated nanoparticles are transferred into the solvent where they continue to grow. This allows the solvent and the molecules within it to influence the nanoparticles, enabling tailoring of the particle size and surface properties.

In experiments described in publication 3, a fibre laser ($\lambda \approx 1060$ nm) was used to produce GaAs-nanoparticles. The nanoparticles were surface-passivated with addition of ammonium sulphide into the ablation solvents.

The direct band gap of GaAs (1.42 eV at room temperature) can be tuned across the visible spectrum by quantum confinement effects. Due to the large Bohr exciton radius in GaAs of 19 nm [230] these effects can already be observed at quite large crystal sizes.

Prior art

GaAs nanoparticles have been produced chemically by several synthesis routes:

- from $GaCl_3$ and $As(SiMe_3)_3$ in quinoline [231, 232]
- from $GaCl_3$ and $(Na/K)_3As$ in toluene, monoglyme and diglyme [233]
- from $GaCl_3$ and $As(NMe_2)_3$ in 4-ethylpyridine [234]
- single organometallic precursor in hexadecylamine [235]

The chemically synthesized nanoparticles have been reported to show blue-shifted band gap absorption [231–236] and photoluminescence at visible wavelengths [232–236]. The reported chemical synthesis routes require several process steps and complex precursors. Therefore, the process can take several days to complete.

Laser ablation has been used to produce GaAs nanoparticles in a nitrogen flow and the crystals were reported to be luminescent at a temperature of 2 K. [237] GaAs nanoparticles produced by PLAL were reported by two groups. [238, 239] Lalayan reported visible luminescence, but the samples were not thoroughly characterized to confirm the source of the luminescence. [238] Ganeev *et al.* reported Ga-rich nanoparticles with no clear band-edge absorption and the photoluminescence was not examined. [239]

The surface of pure GaAs tends to oxidise, which can be detrimental for the properties of the nanoparticles. The thickness of the oxide can be comparable to the nanoparticle size and in some cases the nanoparticles can be completely oxidized. In addition, the surface defects affect the electronic and the optical properties of the nanoparticles. In the particular case of photoluminescence, the (surface) defects can enhance non-radiative transition, reducing the photoluminescence. Traub *et al.* etched the surface oxide of chemically prepared nanoparticles and subsequently passivated the surface with sulphur. [240] The photoluminescence intensity was reported to improve significantly, especially after thermal annealing. The nanoparticles in their study were larger than the Bohr exciton radius and thus behaved like bulk-GaAs.

5.6.1 GaAs nanoparticles produced by high-repetition rate fibre laser

The production of GaAs nanoparticles by PLAL was performed in ethanol, de-ionized water and aqueous solutions of ammonium sulphide, a well known surface passivation agent used for bulk GaAs. [241]

The nanoparticle colloids produced in de-ionized water aggregated rapidly and formed a sediment on the bottom of the container. The nanoparticles were stable in ethanol and in ammonium sulphide solutions with concentrations between 0.1 and 10 $mmol/l$. (Fig. 5.6)

Zeta-potential measurements show that the samples produced in ethanol (ζ= -41 mV) and 10 $mmol/l$ of ammonium sulphide (ζ= -48 mV) can be expected to be stable, whereas the low concentration samples (ζ= -20 mV) might sediment over time. The samples prepared in water were agglomerated too rapidly to allow the measurement of the zeta-potential.

Increasing the ammonium sulphide concentration well above 10 $mmol/l$ led to the nano-particles slowly dissolving into the liquid through continued formation of sulphides that subsequently oxidized. Concentration of 100 $mmol/l$ lead to formation of arsenolite (As_2O_3) crystals, which formed micrometer-sized octahedra (Fig. 5.7).

Analysis with a high-resolution transmission electron microscope (HRTEM) showed that the dried samples have formed larger clusters, with primary nanoparticle size typically between 3 and 6 nm (Fig. 5.8). Energy dispersive spectroscopy (EDS) revealed that

Table 5.1: EDS analysis of the nanoparticle cluster shown in figure 5.8.

Element	A - core	B - edge
Ga	45%	32%
As	40%	18%
O	10%	40%
S	5%	10%

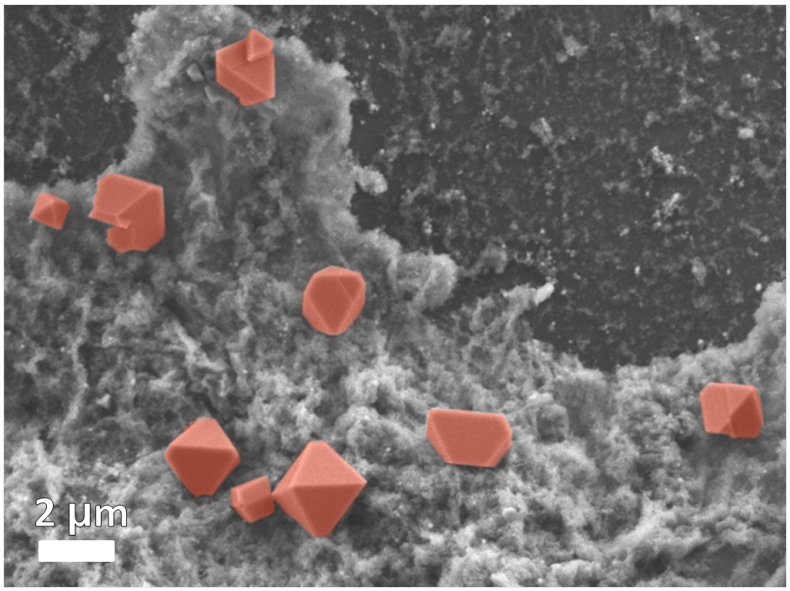

Figure 5.7: High ammonium sulphide concentration leads to formation of micron-sized arsenolite-crystals (As_2O_3).

the centre of the cluster (Fig. 5.8 A) is nearly stoichiometric GaAs, with some oxygen and sulphur. On the other hand, the surface (Fig. 5.8 B) is Ga-rich and mostly formed of oxides and sulphides (Table 5.1).

Raman spectroscopy was performed for samples dried on silicon wafers. The TO and LO phonons of GaAs can be observed in the spectra (Fig. 5.9), with contributions attributed to amorphous As and amorphous GaAs. The signal from the amorphous components decreased considerably after RTA treatment (Fig. 5.9 (b)), which allowed the use of the Gaussian confinement model [22, 23] for estimation of the size of the primary

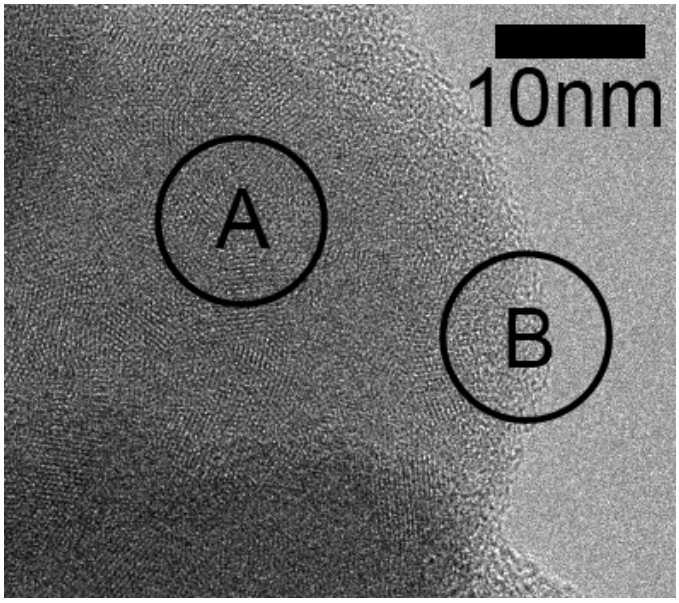

Figure 5.8: High-resolution transmission electron microscope image of a dried GaAs cluster. The primary nanocrystal size typically ranges from 3 to 6 nm. The EDS analysis reported in table 5.1 was performed on areas A and B.

nanocrystals[6].

The phonon dispersion curves were obtained from the neutron scattering experiments performed at a temperature of 12 K [21] and the adjustment to room temperature was done using the temperature dependence measured by Chang *et al.* [242].

The fitting of the TO and LO phonon peaks (blue dotted lines in Fig. 5.9) yields a crystal size of 4 nm. The best fit during the simultaneous fit of the TO and the LO phonon peaks was achieved with $\alpha = 8\pi^2$. Lower values of α typically failed to model the shape of the TO phonon.

X-ray photoelecton spectroscopy (XPS) results agreed with TEM and Raman results. The low penetration depth of the method did not allow probing of the inner parts of the clusters (Fig. 5.8 A) and the amorphous surface layers are thus emphasized in the measurement. The increasing sulphur concentration was observed to decrease the amount of the oxidized species, and the disappearance of the amorphous As and GaAs species

[6]The Raman scattering is influenced by the size of the crystal, not the total size of the nanoparticle and thus the terms crystal and nanocrystal are used in this context.

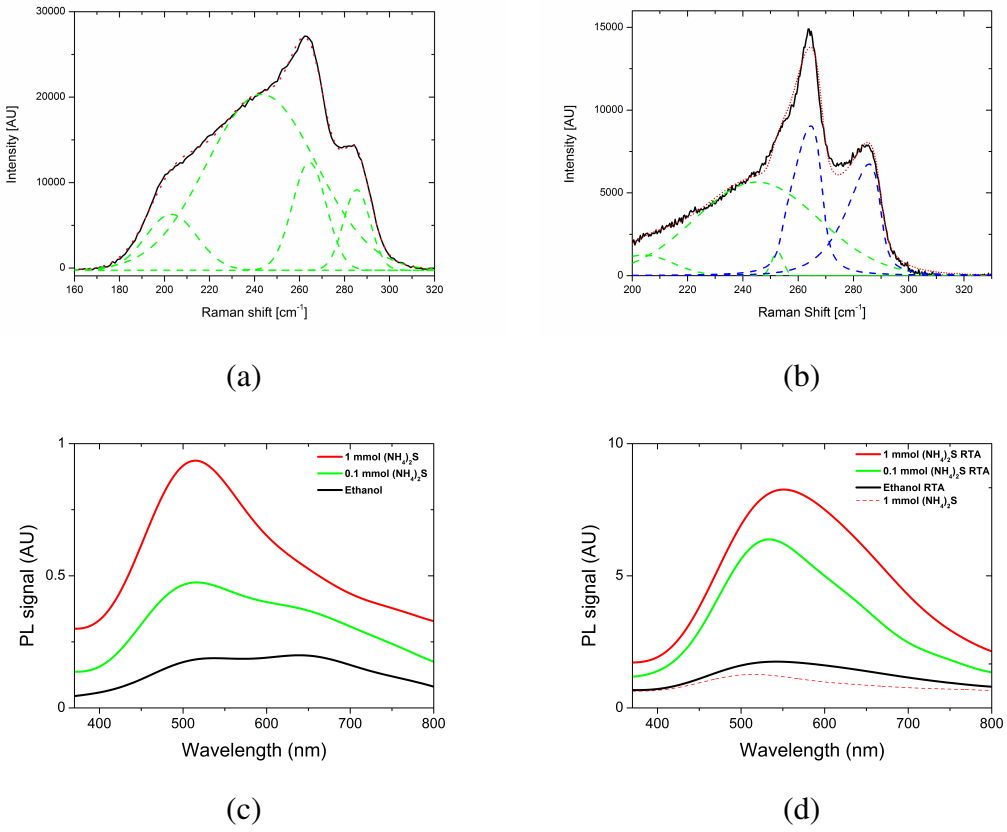

Figure 5.9: The Raman measurement of the dried GaAs samples before RTA (a) shows the peaks related to (from left to right): amorphous As, amorphous GaAs, GaAs TO and LO phonon modes. The signal from the amorphous components decreases due to RTA (b), leaving the TO and LO phonon modes clearly visible. The photoluminescence spectra of the GaAs samples before (c) and after RTA (d).

observed from the Raman spectra after RTA also supports these results.

The photoluminescence maximum of the sulphur passivated nanoparticles dried on silicon was near 530 nm and the intensity was approximately an order of magnitude higher than for samples prepared in ethanol (Fig. 5.9 (c)). The samples prepared in pure water were not luminescent. RTA-treatment further increased the photoluminescence by an order of magnitude (Fig. 5.9 (d)).

In addition to the band gap transitions, the photoluminescence of nanoparticles can be caused by defects and impurities. Therefore, one needs to be careful when claiming

Table 5.2: Size estimates for the produced GaAs nanoparticle

Method	Size estimate
TEM	3-6 nm
Raman-spectroscopy	4 nm
Photoluminescence	3.4 nm

that the source of photoluminescence is related to the band gap, which has blue-shifted due to quantum confinement. Here, the size estimates obtained by TEM and Raman spectroscopy agree well with the one estimated from the photoluminescence maximum wavelength (Table 5.2), supporting such claims.

5.7 Production of core/shell-nanoparticles of gold and silicon dioxide

Many of the potential applications require functionalization or coating of the nanoparticles. These coated core/shell-nanoparticles can be desirable due to their improved stability or new and enhanced properties. Silica is a one of the most common shell-materials since it is biocompatible and silica surfaces can be easily functionalized.

Most of the techniques to coat nanoparticles with silica shells are based on the Stöber-method. [243] The original method produces spheres of silica in selected solvents through hydrolysis of *e.g.* tetraethyl orthosilicate (TEOS) in the presence of a catalyst. The hydrolysis can take place on any oxide surface and thus the method can be applied to coat oxidized nanoparticles.

Gold is a very stable material and does not typically oxidize. Therefore the synthesis of gold/silica-core/shell-particles requires the use of coupling agents or primers, making it typically a two-phase process or a three-phase process if the synthesis of the gold nanoparticles is included.

The method described in publication 4 demonstrates a single-step method to produce gold/silica-core/shell-particles by laser ablation into 2-propanol including TEOS.

Prior art

The synthesis of gold/silica-core/shell-particles via the Stöber-method was first demonstrated by Liz-Marzán *et al.* by using silane molecules with an amino-group as the surface primer. [244, 245] Another approach is to use primer-molecules with thiol-groups. [246] The gold nanoparticles produced by chemical synthesis are often stabilized using citrate-molecules. It was shown by Mine *et al.* that the citrate molecule can also act as an initiator for the silica shell formation. [247] Though the chemical synthesis routes are not especially complex, they often require transferring of the nanoparticles from one solvent to another.

Barcikowski *et al.* reported PLAL in solvents containing TEOS and amine-functionalized TEOS. [248] They observed an increase of the hydrodynamic size of the particles, but the produced colloids were not thoroughly characterized.

5.7.1 Production of gold/silica-core/shell-nanoparticles by PLAL

The gold nanoparticles were produced by a 20 kHZ repetition rate laser with a pulse duration of 10 ns. Experiments were performed at a wavelength of 515 nm, close to the plasmon resonance of the gold nanoparticles, and at a wavelength of 1030 nm.

It was found that the production of silica coated gold nanostructures was successful when both TEOS and the catalyst, ammonia, were present in the solvent (2-propanol) during PLAL, and the laser wavelength was 515 nm (Fig. 5.10 (a), panels C and D). Addition of ammonia into the gold nanoparticle colloids prepared in pure 2-propanol lead to rapid agglomeration and sedimentation. PLAL in ammonia containing 2-propanol, however, produced stable colloids and subsequent addition of TEOS lead to the growth of partial silica shells (Fig. 5.10 (a), panel A).

A study of the surface chemistry of gold nanoparticles produced by PLAL revealed that the surfaces of the particles are oxidized. [224] This might explain the formation of silica on the particles produced with ammonia in the PLAL solution. However, the shells are incomplete, suggesting that the surface oxidation is incomplete at least in the presence of ammonia.

PLAL with a wavelength of 1030 nm produced only partially coated particles (Fig.

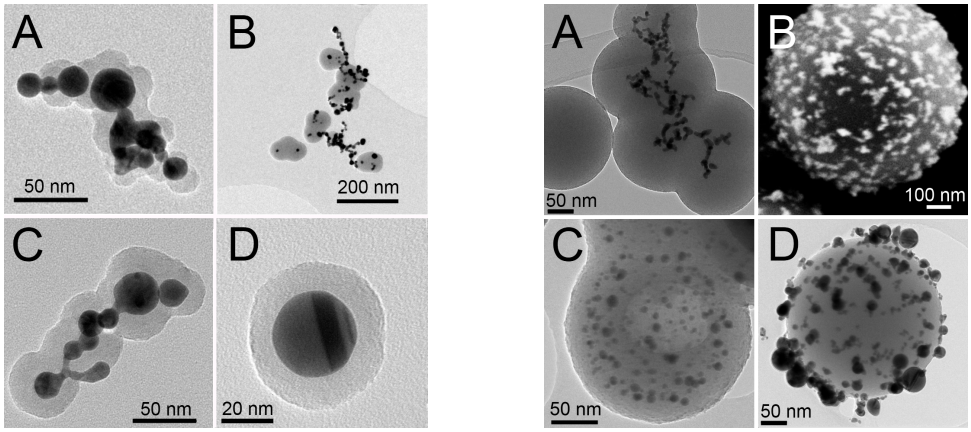

(a) (b)

Figure 5.10: TEM images of the silica coated gold produced by PLAL (a). TEM and SEM (B) images of the silica spheres with incorporated gold nanoparticles and nanoclusters (b).

5.10 (a), panel B). This suggests that the mechanism allowing single-step production of silica coated gold nanostructures is related to the heating of the nanoparticles by the laser. Most likely this occurs after the particles have been formed and are in the bulk of the solvent. Hot nanoparticles can decompose TEOS molecules and bind silicon atoms on their surface, which can then serve as centres for silica growth.

Calculations with a model for heating of nanoparticles by laser illumination [249] suggested that the 1030 nm wavelength laser heats particles that are not in the immediate proximity of the focal point by only a few degrees. For 515 nm the temperature is on the contrary increased by about 1000 degrees, even several millimetres from the focal point.

The plasmon peak was observed to slowly red shift for the samples that were seen to have shells in the TEM analysis (Fig. 5.11). Calculations with the MNPBEM toolbox [250] suggested that the shell thickness of 10 to 15 nm seen in TEM images would cause a red shift of 6 to 7 nm. The measured red shift was approximately 5 nm, which is in good agreement with the calculations, especially considering that the formed silica is no doubt less dense than bulk silica.

PLAL in higher concentrations of TEOS in 2-propanol and water-ethanol mixtures was observed to produce silica spheres with embedded gold nanostructures (Fig. 5.10 (b)). Depending on the exact process parameters, the particles were either individual or

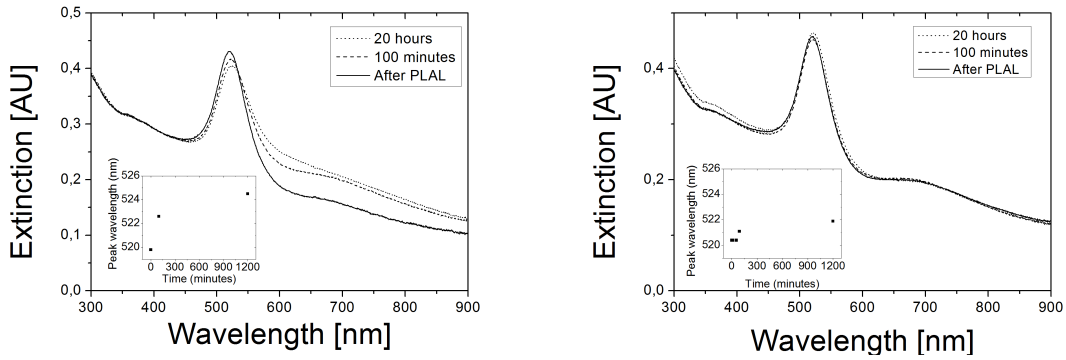

(a) (b)

Figure 5.11: The growth of the silica shells was observed to cause a red shift in the plasmon peak (a). The spectra of a sample with too low TEOS concentration for silica growth showed no change (b).

agglomerated, and either on the surface of or embedded within the sphere.

Though the production of silica coated nanoparticles was successful, a considerable fraction of the particles were agglomerates. This was most likely caused by the high repetition rate of the laser, and production of single core-shell particles should be successful using a lower repetition rate.

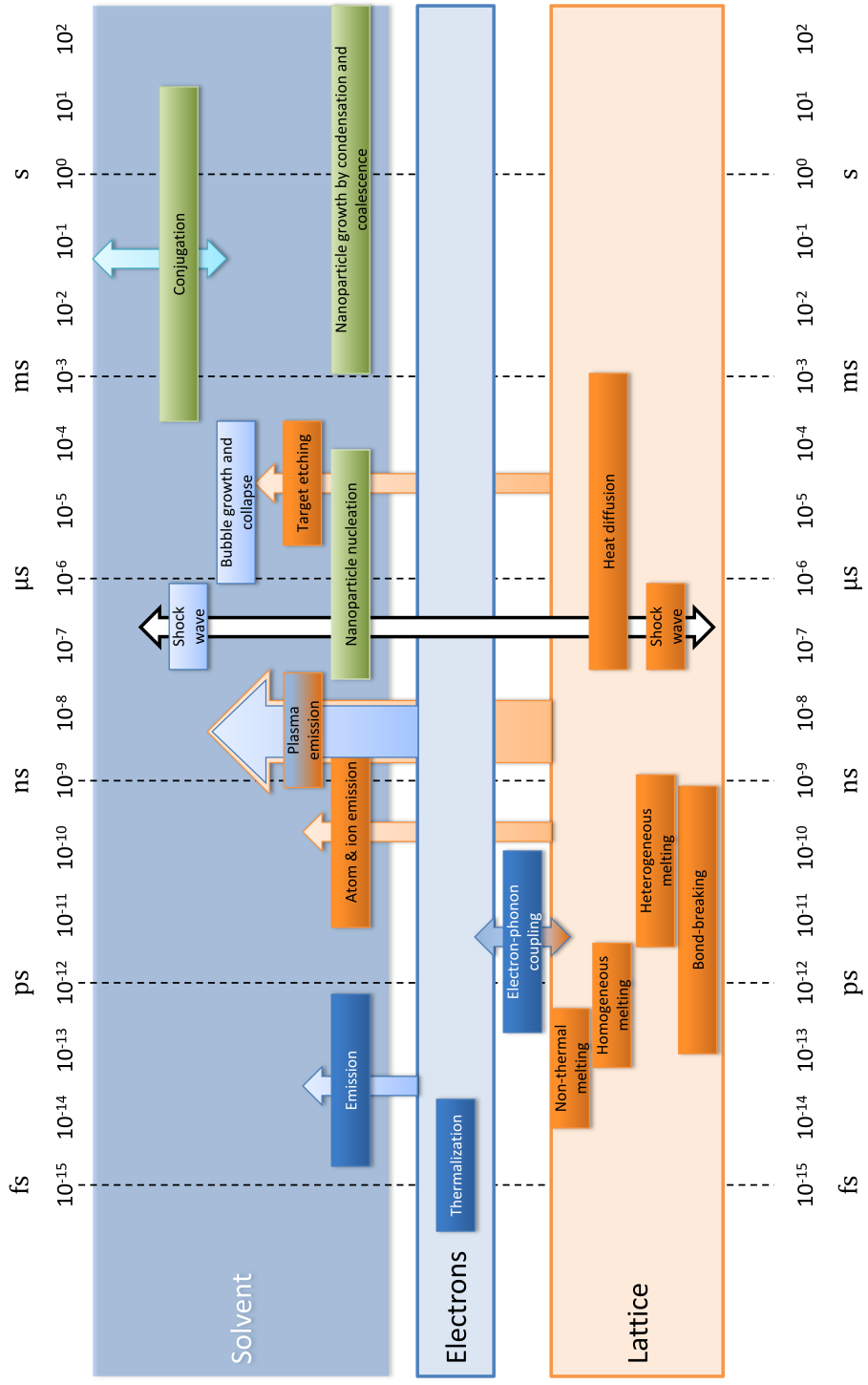

Figure 5.12: A summary of the timescales related to PLAL.

Chapter 6

Conclusion

In this work various types of nanomaterials were produced by pulsed laser ablation. The properties of the produced materials and the influence of the laser ablation parameters were characterized. In addition, the impact of the high repetition rate of the laser pulses on the ablation process was examined. The experiments conducted in this work demonstrate the suitability of PLAL for production of complex nanoparticles that can be further refined for various interesting applications.

In the PLD experiments, among the first ones reported with a high repetition rate fibre laser, it was discovered that the repetition rate and the beam scanning speed can be used to adjust the mode of ablation between pulsed laser ablation and thermal evaporation. This enabled film structures ranging from smooth films in the thermal evaporation mode to nanoparticle films and high surface area nanofoams in the pulsed laser ablation mode. Thermal evaporation was found to change the stoichiometry of the deposited films, as expected. In addition to the consequences for the evaporated thin films, this approach allows modification of the target surfaces.

This thesis includes previously unpublished work performed on the examination of the up-scaling of PLD. A model to optimize the film thickness homogeneity was developed and successfully implemented. Thermal evaporation with high repetition rate lasers was found to allow higher growth rates without loss in film quality and with lower optical average power than evaporation with CW lasers.

The PLAL experiments studied the combinatory approach of chemical treatment of

PLAL generated nanoparticles with the goal of enabling single-step production of complex materials.

The produced GaAs-nanoparticles were luminescent at visible wavelengths. Simultaneous surface passivation by sulphur was found to decrease the oxidation of the nanoparticles and to increase the luminescence intensity by an order of magnitude. The luminescence was further enhanced after RTA treatment. The peak of the photoluminescence was at approximately 530 nm and size analysis performed by TEM and Raman-spectrometry supports the conclusion that the luminescence originates from band gap transitions that are blue shifted due to quantum confinement.

Coating of gold nanostructures with shells typically requires the use of primer molecules since gold is inherently a very stable and non-reactive material. In this work a single-step method for production of gold nanoparticles with silica shells was developed. The process was found to be enabled by laser-induced heating of the formed nanoparticles. Therefore, the process required the use of a laser with a wavelength resonant with the localized surface plasmon of the gold nanoparticles.

Bibliography

[1] T. H. Maiman, "Stimulated optical radiation in ruby," *Nature*, vol. 187, no. 4736, pp. 493–494, Aug. 1960. [Online]. Available: http://dx.doi.org/10.1038/187493a0

[2] A. Einstein, "Zur Quantentheorie der Strahlung," *Physikalische Zeitschrift*, vol. 18, pp. 121–128, 1917.

[3] R. P. Feynman, "There's plenty of room at the bottom," *Engineering and Science*, vol. 23, pp. 22–36, 1960.

[4] F. Brech and L. Cross, "Optical microemission stimulated by a ruby laser," *Applied Spectroscopy*, vol. 16, p. 59, 1962.

[5] H. M. Smith and A. F. Turner, "Vacuum deposited thin films using a ruby laser," *Applied Optics*, vol. 4, no. 1, pp. 147–148, Jan 1965. [Online]. Available: http://ao.osa.org/abstract.cfm?URI=ao-4-1-147

[6] D. Dijkkamp, T. Venkatesan, X. D. Wu, S. A. Shaheen, N. Jisrawi, Y. H. Min-Lee, W. L. McLean, and M. Croft, "Preparation of Y-Ba-Cu oxide superconductor thin films using pulsed laser evaporation from high t[sub c] bulk material," *Applied Physics Letters*, vol. 51, no. 8, pp. 619–621, 1987. [Online]. Available: http://link.aip.org/link/?APL/51/619/1

[7] S. Ogale, A. Malshe, S. Kanetkar, and S. Kshirsagar, "Formation of diamond particulates by pulsed ruby laser irradiation of graphite immersed in benzene," *Solid state communications*, vol. 84, no. 4, pp. 371–373, 1992.

[8] R. Kostoff, R. Koytcheff, and C. Lau, "Global nanotechnology research literature overview," *Technological Forecasting and Social Change*, vol. 74, no. 9, pp. 1733–1747, 2007.

[9] T. Tsuzuki, "Commercial scale production of inorganic nanoparticles," *International journal of nanotechnology*, vol. 6, no. 5, pp. 567–578, 2009.

[10] H. Kroto, J. Heath, S. O'Brien, R. Curl, and R. Smalley, "C60: buckminsterfullerene," *Nature*, vol. 318, no. 6042, pp. 162–163, 1985.

[11] S. Maier, *Plasmonics: Fundamentals and Applications*. Springer Science+Business Media, LLC, 2007. [Online]. Available: http://books.google.fi/books?id=yT2ux7TmDc8C

[12] M. Kauranen and A. Zayats, "Nonlinear plasmonics," *Nature Photonics*, vol. 6, no. 11, pp. 737–748, 2012.

[13] J. Tsang, J. Kirtley, and J. Bradley, "Surface-enhanced raman spectroscopy and surface plasmons," *Physical Review Letters*, vol. 43, no. 11, pp. 772–775, 1979.

[14] K. Kneipp, Y. Wang, H. Kneipp, L. Perelman, I. Itzkan, R. Dasari, and M. Feld, "Single molecule detection using surface-enhanced raman scattering (sers)," *Physical Review Letters*, vol. 78, no. 9, pp. 1667–1670, 1997.

[15] E. Bailo and V. Deckert, "Tip-enhanced raman scattering," *Chem. Soc. Rev.*, vol. 37, no. 5, pp. 921–930, 2008.

[16] G. Mie, "Beiträge zur optik trüber medien, speziell kolloidaler metallösungen," *Annalen der Physik*, vol. 330, no. 3, pp. 377–445, 1908. [Online]. Available: http://dx.doi.org/10.1002/andp.19083300302

[17] C. Raman and K. Krishnan, "A new type of secondary radiation," *Nature*, vol. 121, no. 3048, pp. 501–502, 1928.

[18] Y. Cao, R. Jin, and C. Mirkin, "Nanoparticles with raman spectroscopic fingerprints for dna and rna detection," *Science*, vol. 297, no. 5586, pp. 1536–1540, 2002.

[19] J. Kim, J. Kim, H. Choi, S. Lee, B. Jun, K. Yu, E. Kuk, Y. Kim, D. Jeong, M. Cho, *et al.*, "Nanoparticle probes with surface enhanced raman spectroscopic tags for cellular cancer targeting," *Analytical chemistry*, vol. 78, no. 19, pp. 6967–6973, 2006.

[20] M. Meneghetti, A. Scarsi, L. Litti, G. Marcolongo, V. Amendola, M. Gobbo, M. Di Chio, A. Boscaini, G. Fracasso, and M. Colombatti, "Plasmonic nanostructures for serrs multiplexed identification of tumor-associated antigens," *Small*, 2012.

[21] D. Strauch and B. Dorner, "Phonon dispersion in gaas," *Journal of Physics: Condensed Matter*, vol. 2, no. 6, p. 1457, 1999.

[22] H. Richter, Z. Wang, and L. Ley, "The one phonon raman spectrum in microcrystalline silicon," *Solid State Communications*, vol. 39, no. 5, pp. 625–629, 1981.

[23] A. Arora, M. Rajalakshmi, T. Ravindran, and V. Sivasubramanian, "Raman spectroscopy of optical phonon confinement in nanostructured materials," *Journal of Raman Spectroscopy*, vol. 38, no. 6, pp. 604–617, 2007.

[24] J. Zi, K. Zhang, and X. Xie, "Comparison of models for Raman spectra of Si nanocrystals," *Physical Review B*, vol. 55, pp. 9263–9266, 1997.

[25] I. Campbell and P. Fauchet, "The effects of microcrystal size and shape on the one phonon Raman spectra of crystalline semiconductors," *Solid State Communications*, vol. 58, no. 10, pp. 739–741, 1986.

[26] A. Lyachev, O. Chekhlov, J. Collier, R. Clarke, M. Galimberti, C. Hernandez-Gomez, P. Matousek, I. Musgrave, D. Neely, P. Norreys, *et al.*, "The 10PW OPCPA Vulcan laser upgrade," in *High Intensity Lasers and High Field Phenomena*. Optical Society of America, 2011.

[27] E. Moses and C. Wuest, "The national ignition facility: laser performance and first experiments," *Fusion science and technology*, vol. 47, no. 3, 2005.

[28] S. Anisimov and B. Luk'yanchuk, "Selected problems of laser ablation theory," *Physics-Uspekhi*, vol. 45, no. 3, pp. 293–324, 2002.

[29] A. Djurisic and E. Li, "Modelling the optical constants of GaAs: excitonic effects at E1, E1+1 critical points," *Semiconductor science and technology*, vol. 14, no. 11, p. 958, 1999. [Online]. Available: http://dx.doi.org/10.1088/0268-1242/14/11/302

[30] A. Kaiser, B. Rethfeld, M. Vicanek, and G. Simon, "Microscopic processes in dielectrics under irradiation by subpicosecond laser pulses," *Physical Review B*, vol. 61, pp. 11 437–11 450, May 2000. [Online]. Available: http://link.aps.org/doi/10.1103/PhysRevB.61.11437

[31] M. Göppert-Mayer, "Über Elementarakte mit zwei Quantensprüngen," *Annalen der Physik*, vol. 401, pp. 273–294, 1931.

[32] P. So, C. Dong, B. Masters, and K. Berland, "Two-photon excitation fluorescence microscopy," *Annual review of biomedical engineering*, vol. 2, no. 1, pp. 399–429, 2000.

[33] F. Helmchen and W. Denk, "Deep tissue two-photon microscopy," *Nature methods*, vol. 2, no. 12, pp. 932–940, 2005.

[34] S. Maruo, O. Nakamura, and S. Kawata, "Three-dimensional microfabrication with two-photon-absorbed photopolymerization," *Opt. Lett.*, vol. 22, no. 2, pp. 132–134, Jan 1997. [Online]. Available: http://ol.osa.org/abstract.cfm?URI=ol-22-2-132

[35] L. V. Keldysh, "Ionization in the field of a strong electromagnetic wave," *Zhurnal Eksperimental'noi i Teoreticheskoi fiziki*, vol. 47, pp. 1945–1957, Nov. 1964.

[36] C. Schaffer, A. Brodeur, and E. Mazur, "Laser-induced breakdown and damage in bulk transparent materials induced by tightly focused femtosecond laser pulses," *Measurement Science and Technology*, vol. 12, no. 11, p. 1784, 2001.

[37] D. Simanovskii, H. Schwettman, H. Lee, and A. Welch, "Midinfrared optical breakdown in transparent dielectrics," *Physical review letters*, vol. 91, no. 10, p. 107601, 2003.

[38] J. Martan, O. Cibulka, and N. Semmar, "Nanosecond pulse laser melting investigation by IR radiometry and reflection-based methods," *Applied Surface Science*, vol. 253, no. 3, pp. 1170 – 1177, 2006. [Online]. Available: http://www.sciencedirect.com/science/article/pii/S0169433206001437

[39] K. Sokolowski-Tinten, J. Bialkowski, M. Boing, A. Cavalleri, and D. von der Linde, "Thermal and nonthermal melting of gallium arsenide after femtosecond laser excitation," *Physical Review B*, vol. 58, pp. R11 805–R11 808, Nov 1998. [Online]. Available: http://link.aps.org/doi/10.1103/PhysRevB.58.R11805

[40] P. Stampfli and K. H. Bennemann, "Time dependence of the laser-induced femtosecond lattice instability of Si and GaAs: Role of longitudinal optical distortions," *Physical Review B*, vol. 49, pp. 7299–7305, Mar 1994. [Online]. Available: http://link.aps.org/doi/10.1103/PhysRevB.49.7299

[41] N. Fabricius, P. Hermes, D. von der Linde, A. Pospieszczyk, and B. Stritzker, "Observation of superheating during picosecond laser melting," *Solid State Communications*, vol. 58, no. 4, pp. 239 – 242, 1986. [Online]. Available: http://www.sciencedirect.com/science/article/pii/0038109886902097

[42] P. Hermes, B. Danielzik, N. Fabricius, D. von der Linde, J. Kuhl, J. Heppner, B. Stritzker, and A. Pospieszczyk, "Evaporation of atoms from femtosecond laser-heated gallium arsenide," *Applied Physics A*, vol. 39, pp. 9–11, 1986, 10.1007/BF01177158. [Online]. Available: http://dx.doi.org/10.1007/BF01177158

[43] B. Rethfeld, V. V. Temnov, K. Sokolowski-Tinten, P. Tsu, D. von der Linde, S. I. Anisimov, S. I. Ashitkov, and M. B. Agranat, "Superfast thermal melting of solids under the action of femtosecond laser pulses," *J. Opt. Technol.*, vol. 71, no. 6, pp. 348–352, Jun 2004. [Online]. Available: http://jot.osa.org/abstract.cfm?URI=jot-71-6-348

[44] F. Seitz and D. Turnbull, *Solid State Physics: Advances in Research and Applications*. Academic Press, 1956, vol. 3.

[45] S. Anisimov, "Effect of powerful light (laser) fluxes on metals," *Zhur. Tekhn. Fiziki*, vol. 36, no. 7, pp. 1273–83, 1966.

[46] S. Anisimov, B. Kapeliovich, and T. Perelman, "Electron emission from metal surfaces under the action of ultrashort laser pulses," *Zhurnal Eksperimental'noi i Teoreticheskoi Fiziki*, vol. 66, pp. 776–781, 1974.

[47] J. Fujimoto, J. Liu, E. Ippen, and N. Bloembergen, "Femtosecond laser interaction with metallic tungsten and nonequilibrium electron and lattice temperatures," *Physical Review Letters*, vol. 53, no. 19, pp. 1837–1840, 1984.

[48] X. Y. Wang, D. M. Riffe, Y.-S. Lee, and M. C. Downer, "Time-resolved electron-temperature measurement in a highly excited gold target using femtosecond thermionic emission," *Physical Review B*, vol. 50, pp. 8016–8019, Sep 1994. [Online]. Available: http://link.aps.org/doi/10.1103/PhysRevB.50.8016

[49] C.-K. Sun, F. Vallée, L. H. Acioli, E. P. Ippen, and J. G. Fujimoto, "Femtosecond-tunable measurement of electron thermalization in gold," *Physical Review B*, vol. 50, pp. 15 337–15 348, Nov 1994. [Online]. Available: http://link.aps.org/doi/10.1103/PhysRevB.50.15337

[50] R. Groeneveld, R. Sprik, and A. Lagendijk, "Femtosecond spectroscopy of electron-electron and electron-phonon energy relaxation in Ag and Au," *Physical Review B*, vol. 51, no. 17, p. 11433, 1995.

[51] J. Hohlfeld, J. Müller, S. Wellershoff, and E. Matthias, "Time-resolved thermoreflectivity of thin gold films and its dependence on film thickness," *Applied Physics B: Lasers and Optics*, vol. 64, no. 3, pp. 387–390, 1997.

[52] J. Reif, "High power laser interaction with the surface of wide bandgap materials," *Optical Engineering*, vol. 28, no. 10, pp. 281 122–281 122–, 1989. [Online]. Available: +http://dx.doi.org/10.1117/12.7977097

[53] J. Reif, M. Henyk, and D. Wolfframm, "Explosive femtosecond ablation from ionic crystals," pp. 26–33, 2000. [Online]. Available: +http://dx.doi.org/10.1117/12.387576

[54] R. Stoian, A. Rosenfeld, D. Ashkenasi, I. V. Hertel, N. M. Bulgakova, and E. E. B. Campbell, "Surface charging and impulsive ion ejection during ultrashort pulsed laser ablation," *Physical Review Letters*, vol. 88, p. 097603, Feb 2002. [Online]. Available: http://link.aps.org/doi/10.1103/PhysRevLett.88.097603

[55] R. Stoian, D. Ashkenasi, A. Rosenfeld, and E. E. B. Campbell, "Coulomb explosion in ultrashort pulsed laser ablation of Al_2O_3," *Physical Review B*, vol. 62, pp. 13 167–13 173, Nov 2000. [Online]. Available: http://link.aps.org/doi/10.1103/PhysRevB.62.13167

[56] M. Terasawa, Z. Insepov, T. Sekioka, A. Valuev, and T. Mitamura, "Sputtering due to coulomb explosion in highly charged ion bombardment," *Nuclear Instruments and Methods in Physics Research Section B: Beam Interactions with Materials and Atoms*, vol. 212, pp. 436–441, 2003.

[57] W. Roeterdink, L. Juurlink, O. Vaughan, J. Dura Diez, M. Bonn, and A. Kleyn, "Coulomb explosion in femtosecond laser ablation of Si (111)," *Applied physics letters*, vol. 82, no. 23, pp. 4190–4192, 2003.

[58] B. Chichkov, C. Momma, S. Nolte, F. Von Alvensleben, and A. Tünnermann, "Femtosecond, picosecond and nanosecond laser ablation of solids," *Applied Physics A: Materials Science & Processing*, vol. 63, no. 2, pp. 109–115, 1996.

[59] R. Kelly, "On the dual role of the knudsen layer and unsteady, adiabatic expansion in pulse sputtering phenomena," *The Journal of Chemical Physics*, vol. 92, no. 8, pp. 5047–5056, 1990. [Online]. Available: http://link.aip.org/link/?JCP/92/5047/1

[60] S. Amoruso, "Modeling of uv pulsed-laser ablation of metallic targets," *Applied Physics A: Materials Science & Processing*, vol. 69, pp. 323–332,

1999, 10.1007/s003390051008. [Online]. Available: http://dx.doi.org/10.1007/s003390051008

[61] M. Ashfold, F. Claeyssens, G. Fuge, and S. Henley, "Pulsed laser ablation and deposition of thin films," *Chemical Society Reviews*, vol. 33, no. 1, pp. 23–31, 2004.

[62] B. Thestrup, B. Toftmann, J. Schou, B. Doggett, and J. Lunney, "Ion dynamics in laser ablation plumes from selected metals at 355 nm," *Applied surface science*, vol. 197, pp. 175–180, 2002.

[63] B. Garrison, T. Itina, and L. Zhigilei, "Limit of overheating and the threshold behavior in laser ablation," *Physical Review E*, vol. 68, no. 4, p. 041501, 2003.

[64] M. Martynyuk, "Role of the boiling and evaporation of molten metal during the electrical explosion of a wire," *Zhur. Tekhn. Fiziki*, vol. 44, no. 6, pp. 1262–1270, 1974.

[65] Q. Lu, S. S. Mao, X. Mao, and R. E. Russo, "Delayed phase explosion during high-power nanosecond laser ablation of silicon," *Applied Physics Letters*, vol. 80, no. 17, pp. 3072–3074, 2002. [Online]. Available: http://link.aip.org/link/?APL/80/3072/1

[66] A. Miotello and R. Kelly, "Laser-induced phase explosion: new physical problems when a condensed phase approaches the thermodynamic critical temperature," *Applied Physics A: Materials Science and Processing*, vol. 69, no. 7, pp. 67–73, 1999.

[67] J. H. Yoo, S. H. Jeong, X. L. Mao, R. Greif, and R. E. Russo, "Evidence for phase-explosion and generation of large particles during high power nanosecond laser ablation of silicon," *Applied Physics Letters*, vol. 76, no. 6, pp. 783–785, 2000. [Online]. Available: http://link.aip.org/link/?APL/76/783/1

[68] J. Yoo, S. Jeong, R. Greif, and R. Russo, "Explosive change in crater properties during high power nanosecond laser ablation of silicon," *Journal of Applied physics*, vol. 88, no. 3, pp. 1638–1649, 2000.

[69] C. Körner, R. Mayerhofer, M. Hartmann, and H. Bergmann, "Physical and material aspects in using visible laser pulses of nanosecond duration for ablation," *Applied Physics A: Materials Science & Processing*, vol. 63, no. 2, pp. 123–131, 1996.

[70] N. Bulgakova and A. Bulgakov, "Pulsed laser ablation of solids: transition from normal vaporization to phase explosion," *Applied Physics A: Materials Science & Processing*, vol. 73, no. 2, pp. 199–208, 2001.

[71] K. Sokolowski-Tinten, J. Bialkowski, A. Cavalleri, D. von der Linde, A. Oparin, J. Meyer-ter Vehn, and S. I. Anisimov, "Transient states of matter during short pulse laser ablation," *Physical Review Letters*, vol. 81, pp. 224–227, 1998. [Online]. Available: http://link.aps.org/doi/10.1103/PhysRevLett.81.224

[72] D. von der Linde and K. Sokolowski-Tinten, "The physical mechanisms of short-pulse laser ablation," *Applied Surface Science*, vol. 154, pp. 1–10, 2000.

[73] L. Zhigilei and B. Garrison, "Mechanisms of laser ablation from molecular dynamics simulations: dependence on the initial temperature and pulse duration," *Applied Physics A: Materials Science & Processing*, vol. 69, no. 7, pp. 75–80, 1999.

[74] J. Kanasaki, T. Ishida, K. Ishikawa, and K. Tanimura, "Laser-induced electronic bond breaking and desorption of adatoms on Si(111)- (7×7)," *Physical Review Letters*, vol. 80, pp. 4080–4083, 1998. [Online]. Available: http://link.aps.org/doi/10.1103/PhysRevLett.80.4080

[75] J. Reif, F. Costache, S. Eckert, and M. Henyk, "Mechanisms of ultra-short laser pulse ablation from ionic crystals," *Applied Physics A: Materials Science & Processing*, vol. 79, no. 4, pp. 1229–1231, 2004.

[76] M. Henyk, D. Wolfframm, and J. Reif, "Ultra short laser pulse induced charged particle emission from wide bandgap crystals," *Applied surface science*, vol. 168, no. 1, pp. 263–266, 2000.

[77] D. Perez and L. Lewis, "Molecular-dynamics study of ablation of solids under femtosecond laser pulses," *Physical Review B*, vol. 67, no. 18, p. 184102, 2003.

[78] ——, "Ablation of solids under femtosecond laser pulses," *Physical review letters*, vol. 89, no. 25, p. 255504, 2002.

[79] E. Leveugle, D. Ivanov, and L. Zhigilei, "Photomechanical spallation of molecular and metal targets: molecular dynamics study," *Applied Physics A: Materials Science & Processing*, vol. 79, no. 7, pp. 1643–1655, 2004.

[80] L. Zhigilei, Z. Lin, and D. Ivanov, "Atomistic modeling of short pulse laser ablation of metals: connections between melting, spallation, and phase explosion?" *The Journal of Physical Chemistry C*, vol. 113, no. 27, pp. 11 892–11 906, 2009.

[81] A. Bulgakov, I. Ozerov, and W. Marine, "Cluster emission under femtosecond laser ablation of silicon," *Thin Solid Films*, vol. 453, pp. 557–561, 2004.

[82] T. Glover, "Hydrodynamics of particle formation following femtosecond laser ablation," *JOSA B*, vol. 20, no. 1, pp. 125–131, 2003.

[83] S. Amoruso, R. Bruzzese, M. Vitiello, N. Nedialkov, and P. Atanasov, "Experimental and theoretical investigations of femtosecond laser ablation of aluminum in vacuum," *Journal of applied physics*, vol. 98, no. 4, pp. 044 907–044 907, 2005.

[84] S. Amoruso, G. Ausanio, R. Bruzzese, M. Vitiello, and X. Wang, "Femtosecond laser pulse irradiation of solid targets as a general route to nanoparticle formation in a vacuum," *Physical Review B*, vol. 71, no. 3, p. 033406, 2005.

[85] O. Albert, S. Roger, Y. Glinec, J. Loulergue, J. Etchepare, C. Boulmer-Leborgne, J. Perrière, and E. Millon, "Time-resolved spectroscopy measurements of a titanium plasma induced by nanosecond and femtosecond lasers," *Applied Physics A: Materials Science & Processing*, vol. 76, no. 3, pp. 319–323, 2003.

[86] S. Amoruso, G. Ausanio, A. Barone, R. Bruzzese, L. Gragnaniello, M. Vitiello, and X. Wang, "Ultrashort laser ablation of solid matter in vacuum: a comparison

between the picosecond and femtosecond regimes," *Journal of Physics B: Atomic, Molecular and Optical Physics*, vol. 38, no. 20, p. L329, 2005.

[87] I. NoorBatcha, R. Lucchese, and Y. Zeiri, "Effects of gas-phase collisions on particles rapidly desorbed from surfaces," *Physical Review B*, vol. 36, pp. 4978–4981, 1987.

[88] S. Amoruso, R. Bruzzese, N. Spinelli, and R. Velotta, "Characterization of laser-ablation plasmas," *Journal of Physics B: Atomic, Molecular and Optical Physics*, vol. 32, no. 14, p. R131, 1999. [Online]. Available: http://stacks.iop.org/0953-4075/32/i=14/a=201

[89] J. Kools, T. Baller, S. De Zwart, and J. Dieleman, "Gas flow dynamics in laser ablation deposition," *Journal of applied physics*, vol. 71, no. 9, pp. 4547–4556, 1992.

[90] S. Anisimov, D. Bäuerle, and B. Luk'Yanchuk, "Gas dynamics and film profiles in pulsed-laser deposition of materials," *Physical Review B*, vol. 48, no. l6, 1993.

[91] S. Anisimov, B. Luk'yanchuk, and A. Luches, "An analytical model for three-dimensional laser plume expansion into vacuum in hydrodynamic regime," *Applied Surface Science*, vol. 96, pp. 24–32, 1996.

[92] J. Schou, S. Amoruso, and J. Lunney, "Plume dynamics," *Laser Ablation and its Applications*, pp. 67–95, 2007.

[93] D. Marla, U. Bhandarkar, and S. Joshi, "Critical assessment of the issues in the modeling of ablation and plasma expansion processes in the pulsed laser deposition of metals," *Journal of Applied Physics*, vol. 109, no. 2, pp. 021 101–021 101, 2011.

[94] P. Dyer, "Electrical characterization of plasma generation in KrF laser Cu ablation," *Applied Physics Letters*, vol. 55, no. 16, pp. 1630–1632, 1989.

[95] C. Afonso, R. Serna, F. Catalina, and D. Bermejo, "Good-quality Ge films grown by excimer laser deposition," *Applied Surface Science*, vol. 46, no. 1, pp. 249–253, 1990.

[96] R. Wood, J. Leboeuf, K. Chen, D. Geohegan, and A. Puretzky, "Dynamics of plume propagation, splitting, and nanoparticle formation during pulsed-laser ablation," *Applied surface science*, vol. 127, pp. 151–158, 1998.

[97] D. Geohegan, A. Puretzky, G. Duscher, and S. Pennycook, "Time-resolved imaging of gas phase nanoparticle synthesis by laser ablation," *Applied physics letters*, vol. 72, no. 23, pp. 2987–2989, 1998.

[98] S. Harilal, C. Bindhu, M. Tillack, F. Najmabadi, and A. Gaeris, "Internal structure and expansion dynamics of laser ablation plumes into ambient gases," *Journal of Applied Physics*, vol. 93, no. 5, pp. 2380–2388, 2003.

[99] J. Gonzalo, J. Siegel, A. Perea, D. Puerto, V. Resta, M. Galvan-Sosa, and C. Afonso, "Imaging self-sputtering and backscattering from the substrate during pulsed laser deposition of gold," *Physical Review B*, vol. 76, no. 3, p. 035435, 2007.

[100] A. Miziolek, V. Palleschi, and I. Schechter, *Laser Induced Breakdown Spectroscopy*. Cambridge University Press, 2006.

[101] K. Song, Y. Lee, and J. Sneddon, "Applications of laser-induced breakdown spectrometry," *Applied Spectroscopy Reviews*, vol. 32, no. 3, pp. 183–235, 1997.

[102] D. Rusak, B. Castle, B. Smith, and J. Winefordner, "Fundamentals and applications of laser-induced breakdown spectroscopy," *Critical Reviews in Analytical Chemistry*, vol. 27, no. 4, pp. 257–290, 1997.

[103] A. Knight, N. Scherbarth, D. Cremers, and M. Ferris, "Characterization of laser-induced breakdown spectroscopy (LIBS) for application to space exploration," *Applied Spectroscopy*, vol. 54, no. 3, pp. 331–340, 2000.

[104] J. Hermann, C. Boulmer-Leborgne, and D. Hong, "Diagnostics of the early phase of an ultraviolet laser induced plasma by spectral line analysis considering self-absorption," *Journal of applied physics*, vol. 83, no. 2, pp. 691–696, 1998.

[105] Y. Yamagata, A. Sharma, J. Narayan, R. Mayo, J. Newman, and K. Ebihara, "Optical emission study of ablation plasma plume in the preparation of diamond-like carbon films by KrF excimer laser," *Journal of applied physics*, vol. 86, no. 8, pp. 4154–4159, 1999.

[106] N. Shaikh, S. Hafeez, B. Rashid, and M. Baig, "Spectroscopic studies of laser induced aluminum plasma using fundamental, second and third harmonics of a Nd:YAG laser," *The European Physical Journal D-Atomic, Molecular, Optical and Plasma Physics*, vol. 44, no. 2, pp. 371–379, 2007.

[107] I. Seppälä, "Emissiospektrimittauksia PLD-plasmasta," 2008.

[108] R. Walkup, J. Jasinski, and R. Dreyfus, "Studies of excimer laser ablation of solids using a Michelson interferometer," *Applied physics letters*, vol. 48, no. 24, pp. 1690–1692, 1986.

[109] R. Lindley, R. Gilgenbach, C. Ching, J. Lash, and G. Doll, "Resonant holographic interferometry measurements of laser ablation plumes in vacuum, gas, and plasma environments," *Journal of applied physics*, vol. 76, no. 9, pp. 5457–5472, 1994.

[110] J. Lash, R. Gilgenbach, and H. Spindler, "Ionization dynamics of iron plumes generated by laser ablation versus a laser-ablation-assisted-plasma discharge ion source," *Journal of applied physics*, vol. 79, no. 5, pp. 2287–2295, 1996.

[111] S. Amoruso, V. Berardi, R. Bruzzese, R. Capobianco, R. Velotta, and M. Armenante, "High fluence laser ablation of aluminum targets: Time-of-flight mass analysis of plasmas produced at wavelengths 532 and 355 nm," *Applied Physics A: Materials Science & Processing*, vol. 62, no. 6, pp. 533–541, 1996.

[112] W. Creasy and J. Brenna, "Formation of high mass carbon cluster ions from laser ablation of polymers and thin carbon films," *The Journal of chemical physics*, vol. 92, no. 4, pp. 2269–2279, 1990.

[113] R. Jordan, D. Cole, J. Lunney, K. Mackay, and D. Givord, "Pulsed laser ablation of copper," *Applied surface science*, vol. 86, no. 1, pp. 24–28, 1995.

[114] T. Hansen, J. Schou, and J. Lunney, "Langmuir probe study of plasma expansion in pulsed laser ablation," *Applied Physics A: Materials Science & Processing*, vol. 69, no. 7, pp. 601–604, 1999.

[115] H. Hertz, L. Rymell, M. Berglund, and L. Malmqvist, "Debris-free soft x-ray generation using a liquid droplet laser-plasma target," in *SPIE's 1995 International Symposium on Optical Science, Engineering, and Instrumentation*. International Society for Optics and Photonics, 1995, pp. 88–93.

[116] P. Jansson, B. Hansson, O. Hemberg, M. Otendal, A. Holmberg, J. De Groot, and H. Hertz, "Liquid-tin-jet laser-plasma extreme ultraviolet generation," *Applied physics letters*, vol. 84, no. 13, pp. 2256–2258, 2004.

[117] S. Bulanov and V. Khoroshkov, "Feasibility of using laser ion accelerators in proton therapy," *Plasma Physics Reports*, vol. 28, no. 5, pp. 453–456, 2002.

[118] C. Phipps and M. Michaelis, "LISP: Laser impulse space propulsion," *Laser and Particle Beams-Pulse Power and High Energy Densities*, vol. 12, no. 1, pp. 23–54, 1994.

[119] R. Kodama, P. Norreys, K. Mima, A. Dangor, R. Evans, H. Fujita, Y. Kitagawa, K. Krusheinick, T. Miyakoshi, N. Miyanaga, *et al.*, "Fast heating of ultrahigh-density plasma as a step towards laser fusion ignition," *Nature*, vol. 412, no. 6849, pp. 798–802, 2001.

[120] M. Mero, J. Liu, W. Rudolph, D. Ristau, and K. Starke, "Scaling laws of femtosecond laser pulse induced breakdown in oxide films," *Physical Review B*, vol. 71, no. 11, p. 115109, 2005.

[121] B. Stuart, M. Feit, A. Rubenchik, B. Shore, and M. Perry, "Laser-induced damage in dielectrics with nanosecond to subpicosecond pulses," *Physical Review Letters*, vol. 74, no. 12, pp. 2248–2251, 1995.

[122] A. Rosenfeld, M. Lorenz, R. Stoian, and D. Ashkenasi, "Ultrashort-laser-pulse damage threshold of transparent materials and the role of incubation," *Applied Physics A: Materials Science & Processing*, vol. 69, no. 7, pp. 373–376, 1999.

[123] B. Stuart, M. Feit, S. Herman, A. Rubenchik, B. Shore, and M. Perry, "Optical ablation by high-power short-pulse lasers," *JOSA B*, vol. 13, no. 2, pp. 459–468, 1996.

[124] A. Tien, S. Backus, H. Kapteyn, M. Murnane, and G. Mourou, "Short-pulse laser damage in transparent materials as a function of pulse duration," *Physical Review Letters*, vol. 82, no. 19, pp. 3883–3886, 1999.

[125] J. Jasapara, A. Nampoothiri, W. Rudolph, D. Ristau, and K. Starke, "Femtosecond laser pulse induced breakdown in dielectric thin films," *Physical Review B*, vol. 63, no. 4, p. 045117, 2001.

[126] M. Mero, B. Clapp, J. Jasapara, W. Rudolph, D. Ristau, K. Starke, S. Martin, W. Kautek, *et al.*, "On the damage behavior of dielectric films when illuminated with multiple femtosecond laser pulses," *Optical Engineering*, vol. 44, no. 5, pp. 051 107–051 107, 2005.

[127] D. Das, J. McDonald, S. Yalisove, and T. Pollock, "Femtosecond pulsed laser damage characteristics of $Y_2O_3 - ZrO_2$ thermal barrier coating," *Applied Physics A: Materials Science & Processing*, vol. 91, no. 3, pp. 421–428, 2008.

[128] B. Luther-Davies, A. Rode, N. Madsen, and E. Gamaly, "Picosecond high-repetition-rate pulsed laser ablation of dielectrics: the effect of energy accumulation between pulses," *Optical Engineering*, vol. 44, no. 5, pp. 051 102–051 102, 2005.

[129] D. Chrisey and G. Hubler, "Pulsed laser deposition of thin films," *Pulsed Laser Deposition of Thin Films, by Douglas B. Chrisey (Editor), Graham K. Hubler (Editor), pp. 648. ISBN 0-471-59218-8. Wiley-VCH, May 2003.*, vol. 1, 2003.

[130] P. Willmott and J. Huber, "Pulsed laser vaporization and deposition," *Reviews of Modern Physics*, vol. 72, no. 1, p. 315, 2000.

[131] J. Cheung, M. Khoshnevisan, and T. Magee, "Heteroepitaxial growth of CdTe on GaAs by laser assisted deposition," *Applied Physics Letters*, vol. 43, no. 5, pp. 462–464, 1983.

[132] J. Dubowski, D. Williams, P. Sewell, and P. Norman, "Epitaxial growth of (100) CdTe on (100) GaAs induced by pulsed laser evaporation," *Applied Physics Letters*, vol. 46, no. 11, pp. 1081–1083, 1985.

[133] N. Ong, J. Moyle, J. Bajaj, and J. Cheung, "Quantized Hall effect and weak localization effects in two-dimensional HgTe–CdTe superlattices," *Journal of Vacuum Science & Technology A: Vacuum, Surfaces, and Films*, vol. 5, no. 5, pp. 3079–3084, 1987.

[134] J. Cheung and J. Madden, "Growth of HgCdTe epilayers with any predesigned compositional profile by laser molecular beam epitaxy," *Journal of Vacuum Science & Technology B: Microelectronics and Nanometer Structures*, vol. 5, no. 3, pp. 705–708, 1987.

[135] C. Lange, M. Barsoum, and P. Schaaf, "Towards the synthesis of MAX-phase functional coatings by pulsed laser deposition," *Applied Surface Science*, vol. 254, no. 4, pp. 1232–1235, 2007.

[136] H. Tabata, H. Tanaka, and T. Kawai, "Formation of artificial $BaTiO_3/SrTiO_3$ superlattices using pulsed laser deposition and their dielectric properties," *Applied physics letters*, vol. 65, no. 15, pp. 1970–1972, 1994.

[137] D. Lowndes, D. Geohegan, A. Puretzky, D. Norton, and C. Rouleau, "Synthesis of novel thin-film materials by pulsed laser," *Science*, vol. 273, p. 16, 1996.

[138] J. Kim, H. Kim, D. Kim, Y. Ihm, and W. Choo, "Magnetic properties of epitaxially grown semiconducting ZnCoO thin films by pulsed laser deposition," *Journal of applied physics*, vol. 92, p. 6066, 2002.

[139] J. Lappalainen, J. Frantti, and V. Lantto, "Electrical and mechanical properties of ferroelectric thin films laser ablated from a PbNd(ZrTi)O target," *Journal of applied physics*, vol. 82, p. 3469, 1997.

[140] G. Hass and J. Ramsey, "Vacuum deposition of dielectric and semiconductor films by a CO_2 laser," *Applied Optics*, vol. 8, no. 6, pp. 1115–1118, 1969.

[141] N. Madani and K. Nichols, "The use of a carbon-dioxide laser for the deposition of MOS diodes," *Isr. J. Technol.*, vol. 9, p. 245, 1971.

[142] H. Sankur and J. Cheung, "Highly oriented ZnO films grown by laser evaporation," *Journal of Vacuum Science & Technology A: Vacuum, Surfaces, and Films*, vol. 1, no. 4, pp. 1806–1809, 1983.

[143] S. Yaginuma, J. Yamaguchi, M. Haemori, K. Itaka, Y. Matsumoto, M. Kondo, and H. Koinuma, "Continuous wave infrared laser deposition of organic thin films," in *Journal of Physics: Conference Series*, vol. 59, no. 1. IOP Publishing, 2007, p. 520.

[144] H. Sankur, W. Gunning, J. DeNatale, and J. Flintoff, "High-quality optical and epitaxial Ge films formed by laser evaporation," *Journal of Applied Physics*, vol. 65, no. 6, pp. 2475–2478, 1989.

[145] D. Brice, J. Tsao, and S. Picraux, "Partitioning of ion-induced surface and bulk displacements," *Nuclear Instruments and Methods in Physics Research Section B: Beam Interactions with Materials and Atoms*, vol. 44, no. 1, pp. 68–78, 1989.

[146] F. Rong, "Liquid target pulsed laser deposition," *Applied physics letters*, vol. 67, no. 7, pp. 1022–1024, 1995.

[147] A. Reilly, C. Allmond, S. Watson, J. Gammon, and J. Kim, "Pulsed laser deposition with a high average power free electron laser: Benefits of subpicosecond pulses with high repetition rate," *Journal of applied physics*, vol. 93, no. 5, pp. 3098–3101, 2003.

[148] J. Greene, "Physics of film growth from the vapor phase," *NATO ASI SERIES E APPLIED SCIENCES*, vol. 234, 1993.

[149] S. Fahler, K. Sturm, and H. Krebs, "Resputtering during the growth of pulsed-laser-deposited metallic films in vacuum and in an ambient gas," *Applied Physics Letters*, vol. 75, no. 24, pp. 3766–3768, 1999.

[150] T. Scharf and H. Krebs, "Influence of inert gas pressure on deposition rate during pulsed laser deposition," *Applied Physics A: Materials Science & Processing*, vol. 75, no. 5, pp. 551–554, 2002.

[151] A. Miotello and P. Ossi, *Laser-surface interactions for new materials production*. Springer, 2010, vol. 130.

[152] T. Makimura, T. Mizuta, and K. Murakami, "Formation dynamics of silicon nanoparticles after laser ablation studied using plasma emission caused by second-laser decomposition," *Applied Physics Letters*, vol. 76, no. 11, pp. 1401–1403, 2000.

[153] M. Tillack, D. Blair, and S. Harilal, "The effect of ionization on cluster formation in laser ablation plumes," *Nanotechnology*, vol. 15, no. 3, p. 390, 2004.

[154] F. Di Fonzo, A. Bailini, V. Russo, A. Baserga, D. Cattaneo, M. Beghi, P. Ossi, C. Casari, A. Li Bassi, and C. Bottani, "Synthesis and characterization of tungsten and tungsten oxide nanostructured films," *Catalysis today*, vol. 116, no. 1, pp. 69–73, 2006.

[155] D. Lowndes, C. Rouleau, T. Thundat, G. Duscher, E. Kenik, and S. Pennycook, "Silicon and zinc telluride nanoparticles synthesized by pulsed laser ablation: size distributions and nanoscale structure," *Applied surface science*, vol. 127, pp. 355–361, 1998.

[156] H. Kawasaki, J. Namba, K. Iwatsuji, Y. Suda, K. Wada, K. Ebihara, and T. Ohshima, "NO_x gas sensing properties of tungsten oxide thin films synthesized by pulsed laser deposition method," *Applied surface science*, vol. 197, pp. 547–551, 2002.

[157] A. Baserga, V. Russo, F. Di Fonzo, A. Bailini, D. Cattaneo, C. Casari, A. Li Bassi, and C. Bottani, "Nanostructured tungsten oxide with controlled properties: Synthesis and Raman characterization," *Thin Solid Films*, vol. 515, no. 16, pp. 6465–6469, 2007.

[158] T. Itina, K. Gouriet, L. Zhigilei, S. Noël, J. Hermann, and M. Sentis, "Mechanisms of small clusters production by short and ultra-short laser ablation," *Applied surface science*, vol. 253, no. 19, pp. 7656–7661, 2007.

[159] D. Scuderi, R. Benzerga, O. Albert, B. Reynier, and J. Etchepare, "Spectral and temporal characteristics of metallic nanoparticles produced by femtosecond laser pulses," *Applied surface science*, vol. 252, no. 13, pp. 4360–4363, 2006.

[160] R. Teghil, L. D'Alessio, A. De Bonis, A. Galasso, P. Villani, and A. Santagata, "Femtosecond pulsed laser ablation and deposition of titanium carbide," *Thin solid films*, vol. 515, no. 4, pp. 1411–1418, 2006.

[161] M. Hahtala, "Menetelmä pulssilaserilla höyrystettävien ohutkalvojen paksuuden reaaliaikaiseen mittaamiseen," 2008.

[162] A. Rode, B. Luther-Davies, and E. Gamaly, "Ultrafast ablation with high-pulse-rate lasers. part ii: Experiments on laser deposition of amorphous carbon films," *Journal of applied physics*, vol. 85, no. 8, pp. 4222–4230, 1999.

[163] E. Gamaly, A. Rode, and B. Luther-Davies, "Ultrafast ablation with high-pulse-rate lasers. part i: Theoretical considerations," *Journal of Applied Physics*, vol. 85, no. 8, pp. 4213–4221, 1999.

[164] F. Kokai, K. Amano, H. Ota, Y. Ochiai, and F. Umemura, "XeCl laser ablative deposition and characterization of yttria-stabilized zirconia thin films on glass and $CeO_2 - Sm_2O_3$," *Journal of applied physics*, vol. 72, no. 2, pp. 699–704, 1992.

[165] M. Hartmanova, M. Jergel, V. Navrátil, K. Navrátil, K. Gmucova, and F. Gandarilla, "Correlation between microscopic and macroscopic properties of yttria-stabilized zirconia thin films," in *Proceedings of the International Workshop on*

Physics and Technology of Thin Films: IWTF 2003, Tehran, Iran, 22 February-6 March 2003. World Scientific Publishing Company Incorporated, 2004, p. 158.

[166] W. Qian, M. Murakami, Y. Ichikawa, and Y. Che, "Highly efficient and controllable PEGylation of gold nanoparticles prepared by femtosecond laser ablation in water," *The Journal of Physical Chemistry C*, vol. 115, no. 47, pp. 23 293–23 298, 2011.

[167] S. Petersen and S. Barcikowski, "In situ bioconjugation: Single step approach to tailored nanoparticle-bioconjugates by ultrashort pulsed laser ablation," *Advanced Functional Materials*, vol. 19, no. 8, pp. 1167–1172, 2009.

[168] G. Compagnini, A. Scalisi, and O. Puglisi, "Ablation of noble metals in liquids: a method to obtain nanoparticles in a thin polymeric film," *Physical Chemistry Chemical Physics*, vol. 4, no. 12, pp. 2787–2791, 2002.

[169] A. Hahn, T. Stöver, G. Paasche, M. Löbler, K. Sternberg, H. Rohm, and S. Barcikowski, "Therapeutic window for bioactive nanocomposites fabricated by laser ablation in polymer-doped organic liquids," *Advanced Engineering Materials*, vol. 12, no. 5, pp. B156–B162, 2010.

[170] S. Stelzig, C. Menneking, M. Hoffmann, K. Eisele, S. Barcikowski, M. Klapper, and K. Müllen, "Compatibilization of laser generated antibacterial Ag-and Cu-nanoparticles for perfluorinated implant materials," *European Polymer Journal*, vol. 47, no. 4, pp. 662–667, 2011.

[171] G. Brandes, A. Schwenke, S. Barcikowski, *et al.*, "Impact of in situ polymer coating on particle dispersion into solid laser-generated nanocomposites," *Physical Chemistry Chemical Physics*, vol. 13, no. 11, pp. 5120–5126, 2011.

[172] C. Sajti, R. Sattari, B. Chichkov, and S. Barcikowski, "Gram scale synthesis of pure ceramic nanoparticles by laser ablation in liquid," *The Journal of Physical Chemistry C*, vol. 114, no. 6, pp. 2421–2427, 2010.

[173] P. Patil, D. Phase, S. Kulkarni, S. Ghaisas, S. Kulkarni, S. Kanetkar, S. Ogale, and V. Bhide, "Pulsed-laser–induced reactive quenching at liquid-solid interface:

Aqueous oxidation of iron," *Physical review letters*, vol. 58, no. 3, pp. 238–241, 1987.

[174] A. Fojtik and A. Henglein, "Laser ablation of films and suspended particles in a solvent: formation of cluster and colloid solutions," *Berichte der Bunsen-Gesellschaft*, vol. 97, no. 2, pp. 252–254, 1993.

[175] J. Neddersen, G. Chumanov, and T. Cotton, "Laser ablation of metals: a new method for preparing SERS active colloids," *Applied spectroscopy*, vol. 47, no. 12, pp. 1959–1964, 1993.

[176] Z. Yan and D. Chrisey, "Pulsed laser ablation in liquid for micro-/nanostructure generation," *Journal of Photochemistry and Photobiology C: Photochemistry Reviews*, 2012.

[177] A. Abdolvand, S. Khan, Y. Yuan, P. Crouse, M. Schmidt, M. Sharp, Z. Liu, and L. Li, "Generation of titanium-oxide nanoparticles in liquid using a high-power, high-brightness continuous-wave fiber laser," *Applied Physics A: Materials Science & Processing*, vol. 91, no. 3, pp. 365–368, 2008.

[178] A. De Giacomo, A. De Bonis, M. Dell?Aglio, O. De Pascale, R. Gaudiuso, S. Orlando, A. Santagata, G. S. Senesi, F. Taccogna, and R. Teghil, "Laser ablation of graphite in water in a range of pressure from 1 to 146 atm using single and double pulse techniques for the production of carbon nanostructures," *The Journal of Physical Chemistry C*, vol. 115, no. 12, pp. 5123–5130, 2011.

[179] K. Saitow, "Silicon nanoclusters selectively generated by laser ablation in supercritical fluid," *The Journal of Physical Chemistry B*, vol. 109, no. 9, pp. 3731–3733, 2005.

[180] D. Werner, T. Ueki, and S. Hashimoto, "Methodological improvement in pulsed laser-induced size reduction of aqueous colloidal gold nanoparticles by applying high pressure," *The Journal of Physical Chemistry C*, vol. 116, no. 9, pp. 5482–5491, 2012.

[181] A. Fujisaki, K. Sano, T. Kinoshita, Y. Takahashi, and T. Yabuzaki, "Implantation of neutral atoms into liquid helium by laser sputtering," *Physical Review Letters*, vol. 71, no. 7, pp. 1039–1042, 1993.

[182] N. Takada, T. Sasaki, and K. Sasaki, "Synthesis of crystalline TiN and Si particles by laser ablation in liquid nitrogen," *Applied Physics A: Materials Science & Processing*, vol. 93, no. 4, pp. 833–836, 2008.

[183] G. Yang, "Laser ablation in liquids: Applications in the synthesis of nanocrystals," *Progress in Materials Science*, vol. 52, no. 4, pp. 648–698, 2007.

[184] H. Zeng, X. Du, S. Singh, S. Kulinich, S. Yang, J. He, and W. Cai, "Nanomaterials via laser ablation/irradiation in liquid: A review," *Advanced Functional Materials*, vol. 22, no. 7, pp. 1333–1353, 2012.

[185] S. Barcikowski, F. Devesa, and K. Moldenhauer, "Impact and structure of literature on nanoparticle generation by laser ablation in liquids," *Journal of Nanoparticle Research*, vol. 11, no. 8, pp. 1883–1893, 2009.

[186] S. Barcikowski and G. Compagnini, "Advanced nanoparticle generation and excitation by lasers in liquids," *Physical Chemistry Chemical Physics*, 2013.

[187] V. Amendola and M. Meneghetti, "What controls the composition and the structure of nanomaterials generated by laser ablation in liquid solution?" *Physical Chemistry Chemical Physics*, 2012.

[188] A. Kruusing, *Handbook of liquids-assisted laser processing*. Elsevier Science, 2007.

[189] J. Dahl, B. Maddux, J. Hutchison, *et al.*, "Toward greener nanosynthesis," *Chemical Reviews-Columbus*, vol. 107, no. 6, pp. 2228–2269, 2007.

[190] R. Crist, J. Grossman, A. Patri, S. Stern, M. Dobrovolskaia, P. Adiseshaiah, J. Clogston, and S. McNeil, "Common pitfalls in nanotechnology: Lessons learned from ncis nanotechnology characterization laboratory," *Integrative Biology*, 2012.

[191] F. Mafuné, J. Kohno, Y. Takeda, T. Kondow, and H. Sawabe, "Formation and size control of silver nanoparticles by laser ablation in aqueous solution," *The Journal of Physical Chemistry B*, vol. 104, no. 39, pp. 9111–9117, 2000.

[192] A. Kabashin and M. Meunier, "Synthesis of colloidal nanoparticles during femtosecond laser ablation of gold in water," *Journal of applied physics*, vol. 94, no. 12, pp. 7941–7943, 2003.

[193] G. Compagnini, A. Scalisi, and O. Puglisi, "Production of gold nanoparticles by laser ablation in liquid alkanes," *Journal of applied physics*, vol. 94, no. 12, pp. 7874–7877, 2003.

[194] T. Tsuji, K. Iryo, N. Watanabe, and M. Tsuji, "Preparation of silver nanoparticles by laser ablation in solution: influence of laser wavelength on particle size," *Applied surface science*, vol. 202, no. 1, pp. 80–85, 2002.

[195] C. Sajti, A. Barchanski, P. Wagener, S. Klein, and S. Barcikowski, "Delay time and concentration effects during bioconjugation of nanosecond laser-generated nanoparticles in a liquid flow," *The Journal of Physical Chemistry C*, vol. 115, no. 12, pp. 5094–5101, 2011.

[196] H. Kurita, A. Takami, and S. Koda, "Size reduction of gold particles in aqueous solution by pulsed laser irradiation," *Applied physics letters*, vol. 72, no. 7, pp. 789–791, 1998.

[197] H. Fujiwara, S. Yanagida, and P. Kamat, "Visible laser induced fusion and fragmentation of thionicotinamide-capped gold nanoparticles," *The Journal of Physical Chemistry B*, vol. 103, no. 14, pp. 2589–2591, 1999.

[198] S. Link, C. Burda, M. Mohamed, B. Nikoobakht, and M. El-Sayed, "Laser photothermal melting and fragmentation of gold nanorods: energy and laser pulse-width dependence," *The Journal of Physical Chemistry A*, vol. 103, no. 9, pp. 1165–1170, 1999.

[199] F. Mafuné, J. Kohno, Y. Takeda, and T. Kondow, "Growth of gold clusters into nanoparticles in a solution following laser-induced fragmentation," *The Journal of Physical Chemistry B*, vol. 106, no. 34, pp. 8555–8561, 2002.

[200] S. Besner, A. Kabashin, and M. Meunier, "Fragmentation of colloidal nanoparticles by femtosecond laser-induced supercontinuum generation," *Applied physics letters*, vol. 89, no. 23, pp. 233 122–233 122, 2006.

[201] A. Mene?ndez-Manjo?n, P. Wagener, and S. Barcikowski, "Transfer-matrix method for efficient ablation by pulsed laser ablation and nanoparticle generation in liquids," *The Journal of Physical Chemistry C*, vol. 115, no. 12, pp. 5108–5114, 2011.

[202] T. Tsuji, Y. Okazaki, Y. Tsuboi, and M. Tsuji, "Nanosecond time-resolved observations of laser ablation of silver in water," *Japanese journal of applied physics*, vol. 46, p. 1533, 2007.

[203] K. Sasaki and N. Takada, "Liquid-phase laser ablation," *Pure and Applied Chemistry*, vol. 82, no. 6, p. 1317, 2010.

[204] W. Soliman, N. Takada, and K. Sasaki, "Growth processes of nanoparticles in liquid-phase laser ablation studied by laser-light scattering," *Applied physics express*, vol. 3, no. 3, p. 5201, 2010.

[205] S. Ibrahimkutty, P. Wagener, A. Menzel, A. Plech, and S. Barcikowski, "Nanoparticle formation in a cavitation bubble after pulsed laser ablation in liquid studied with high time resolution small angle x-ray scattering," *Applied Physics Letters*, vol. 101, no. 10, pp. 103 104–103 104, 2012.

[206] N. Takada, T. Nakano, and K. Sasaki, "Formation of cavitation-induced pits on target surface in liquid-phase laser ablation," *Applied Physics A: Materials Science & Processing*, vol. 101, no. 2, pp. 255–258, 2010.

[207] P. Wagener, A. Schwenke, B. Chichkov, and S. Barcikowski, "Pulsed laser ablation of zinc in tetrahydrofuran: Bypassing the cavitation bubble," *The Journal of Physical Chemistry C*, vol. 114, no. 17, pp. 7618–7625, 2010.

[208] F. Mafuné, J. Kohno, Y. Takeda, T. Kondow, and H. Sawabe, "Structure and stability of silver nanoparticles in aqueous solution produced by laser ablation," *The Journal of Physical Chemistry B*, vol. 104, no. 35, pp. 8333–8337, 2000.

[209] D. Ehrlich, R. Osgood, and T. Deutsch, "Laser-induced microscopic etching of GaAs and InP," *Applied Physics Letters*, vol. 36, no. 8, pp. 698–700, 1980.

[210] J. Wang, H. Niino, and A. Yabe, "One-step microfabrication of fused silica by laser ablation of an organic solution," *Applied Physics A: Materials Science & Processing*, vol. 68, no. 1, pp. 111–113, 1999.

[211] M. Plesset and A. Prosperetti, "Bubble dynamics and cavitation," *Annual Review of Fluid Mechanics*, vol. 9, no. 1, pp. 145–185, 1977.

[212] A. Shima, "Studies on bubble dynamics," *Shock Waves*, vol. 7, no. 1, pp. 33–42, 1997.

[213] A. Tamura, T. Sakka, K. Fukami, and Y. Ogata, "Dynamics of cavitation bubbles generated by multi-pulse laser irradiation of a solid target in water," *Applied Physics A: Materials Science & Processing*, pp. 1–5, 2012.

[214] T. Sakka, S. Iwanaga, Y. Ogata, A. Matsunawa, and T. Takemoto, "Laser ablation at solid–liquid interfaces: An approach from optical emission spectra," *The Journal of Chemical Physics*, vol. 112, p. 8645, 2000.

[215] T. Tsuji, D. Thang, Y. Okazaki, M. Nakanishi, Y. Tsuboi, and M. Tsuji, "Preparation of silver nanoparticles by laser ablation in polyvinylpyrrolidone solutions," *Applied Surface Science*, vol. 254, no. 16, pp. 5224–5230, 2008.

[216] P. Wagener, S. Ibrahimkutty, A. Menzel, A. Plech, and S. Barcikowski, "Dynamics of silver nanoparticle formation and agglomeration inside the cavitation bubble after pulsed laser ablation in liquid," *Physical Chemistry Chemical Physics*, 2012.

[217] T. Itina, "On nanoparticle formation by laser ablation in liquids," *Journal of Physical Chemistry C*, vol. 115, no. 12, p. 5044, 2011.

[218] Y. Tomita, M. Tsubota, and N. An-Naka, "Energy evaluation of cavitation bubble generation and shock wave emission by laser focusing in liquid nitrogen," *Journal of applied physics*, vol. 93, no. 5, pp. 3039–3048, 2003.

[219] M. Brenner, S. Hilgenfeldt, and D. Lohse, "Single-bubble sonoluminescence," *Reviews of modern physics*, vol. 74, no. 2, p. 425, 2002.

[220] A. De Giacomo, M. Dell'Aglio, O. De Pascale, and M. Capitelli, "From single pulse to double pulse ns-laser induced breakdown spectroscopy under water: elemental analysis of aqueous solutions and submerged solid samples," *Spectrochimica Acta Part B: Atomic Spectroscopy*, vol. 62, no. 8, pp. 721–738, 2007.

[221] Y. Raizer, "Condensation of a cloud of vaporized matter expanding in vacuum," *Sov. Phys. JETP*, vol. 37, pp. 1229–1235, 1960.

[222] Y. Zel'Dovich and Y. Raizer, *Physics of shock waves and high-temperature hydrodynamic phenomena*. Dover Publications, 2002.

[223] B. Luk'Yanchuk, W. Marine, and S. Anisimov, "Condensation of vapor and nanoclusters formation within the vapor plume, produced by ns-laser ablation of Si," *Laser Physics*, vol. 8, no. 1, pp. 291–302, 1998.

[224] J. Sylvestre, S. Poulin, A. Kabashin, E. Sacher, M. Meunier, and J. Luong, "Surface chemistry of gold nanoparticles produced by laser ablation in aqueous media," *The Journal of Physical Chemistry B*, vol. 108, no. 43, pp. 16 864–16 869, 2004.

[225] M. Instruments, "Zeta potential theory. 2008," *Malvern Instruments Ltd*.

[226] T. Doane, C. Chuang, R. Hill, and C. Burda, "Nanoparticle ζ-potentials," *Accounts of Chemical Research*, vol. 45, no. 3, pp. 317–326, 2011.

[227] J. Jakobi, A. Menéndez-Manjón, V. Chakravadhanula, L. Kienle, P. Wagener, and S. Barcikowski, "Stoichiometry of alloy nanoparticles from laser ablation of PtIr in acetone and their electrophoretic deposition on PtIr electrodes," *Nanotechnology*, vol. 22, no. 14, p. 145601, 2011.

[228] A. Neumeister, D. Bartke, N. Bärsch, T. Weingärtner, L. Guetaz, A. Montani, G. Compagnini, and S. Barcikowski, "Interface of nanoparticle-coated electropolished stents," *Langmuir*, 2012.

[229] D. Henry, "The cataphoresis of suspended particles. part i. the equation of cataphoresis," *Proceedings of the Royal Society of London. Series A*, vol. 133, no. 821, pp. 106–129, 1931.

[230] L. Brus, "Electron–electron and electron-hole interactions in small semiconductor crystallites: The size dependence of the lowest excited electronic state," *The Journal of Chemical Physics*, vol. 80, p. 4403, 1984.

[231] M. Olshavsky, A. Goldstein, and A. Alivisatos, "Organometallic synthesis of gallium-arsenide crystallites, exhibiting quantum confinement," *Journal of the American Chemical Society*, vol. 112, no. 25, pp. 9438–9439, 1990.

[232] H. Uchida, C. Curtis, and A. Nozik, "Gallium arsenide nanocrystals prepared in quinoline," *The Journal of Physical Chemistry*, vol. 95, no. 14, pp. 5382–5384, 1991.

[233] S. Kher and R. Wells, "A straightforward, new method for the synthesis of nanocrystalline GaAs and GaP," *Chemistry of materials*, vol. 6, no. 11, pp. 2056–2062, 1994.

[234] M. Malik, P. O'Brien, S. Norager, and J. Smith, "Gallium arsenide nanoparticles: synthesis and characterisation," *J. Mater. Chem.*, vol. 13, no. 10, pp. 2591–2595, 2003.

[235] M. Malik, M. Afzaal, P. O'brien, U. Bangert, and B. Hamilton, "Single molecular precursor for synthesis of GaAs nanoparticles," *Materials science and technology*, vol. 20, no. 8, pp. 959–963, 2004.

[236] H. Uchida, C. Curtis, P. Kamat, K. Jones, and A. Nozik, "Optical properties of gallium arsenide nanocrystals," *The Journal of Physical Chemistry*, vol. 96, no. 3, pp. 1156–1160, 1992.

[237] J. Perrière, E. Millon, M. Chamarro, M. Morcrette, and C. Andreazza, "Formation of GaAs nanocrystals by laser ablation," *Applied Physics Letters*, vol. 78, no. 19, pp. 2949–2951, 2001.

[238] A. Lalayan, "Formation of colloidal GaAs and CdS quantum dots by laser ablation in liquid media," *Applied surface science*, vol. 248, no. 1, pp. 209–212, 2005.

[239] R. Ganeev, M. Baba, A. Ryasnyansky, M. Suzuki, and H. Kuroda, "Laser ablation of GaAs in liquids: structural, optical, and nonlinear optical characteristics of colloidal solutions," *Applied Physics B: Lasers and Optics*, vol. 80, no. 4, pp. 595–601, 2005.

[240] M. Traub, J. Biteen, B. Brunschwig, and N. Lewis, "Passivation of GaAs nanocrystals by chemical functionalization," *Journal of the American Chemical Society*, vol. 130, no. 3, pp. 955–964, 2008.

[241] Y. Nannichi, J. Fan, H. Oigawa, and A. Koma, "A model to explain the effective passivation of the GaAs surface by $(NH_4)_2S_x$ treatment," *Jpn. J. Appl. Phys*, vol. 27, no. 12, pp. 2367–2369, 1988.

[242] R. Chang, J. Ralston, D. Keating, and G. Wright, "Light scattering spectra of solids," *by GB Wright) Springer, New York*, p. 369, 1969.

[243] W. Stöber, A. Fink, and E. Bohn, "Controlled growth of monodisperse silica spheres in the micron size range," *Journal of colloid and interface science*, vol. 26, no. 1, pp. 62–69, 1968.

[244] L. Liz-Marzán, M. Giersig, and P. Mulvaney, "Synthesis of nanosized gold-silica core-shell particles," *Langmuir*, vol. 12, no. 18, pp. 4329–4335, 1996.

[245] C. Fernandez-Lopez, C. Mateo-Mateo, R. Alvarez-Puebla, J. Perez-Juste, I. Pastoriza-Santos, and L. Liz-Marzan, "Highly controlled silica coating of PEG-capped metal nanoparticles and preparation of SERS-encoded particles," *Langmuir*, vol. 25, no. 24, pp. 13 894–13 899, 2009.

[246] J. Xu and C. Perry, "A novel approach to Au@ SiO_2 core-shell spheres," *Journal of Non-Crystalline Solids*, vol. 353, no. 11, pp. 1212–1215, 2007.

[247] E. Mine, A. Yamada, Y. Kobayashi, M. Konno, and L. Liz-Marzán, "Direct coating of gold nanoparticles with silica by a seeded polymerization technique," *Journal of colloid and interface science*, vol. 264, no. 2, pp. 385–390, 2003.

[248] S. Barcikowski, J. Jakobi, S. Petersen, A. Hahn, N. Bärsch, and B. Chichkov, "Adding functionality to metal nanoparticles during femtosecond laser ablation in liquids," in *Proceedings of 24nd International Conference on Applications of Lasers and Electro-Optics ICALEO*, vol. 10, 2007, p. 29.

[249] A. Govorov, W. Zhang, T. Skeini, H. Richardson, J. Lee, and N. Kotov, "Gold nanoparticle ensembles as heaters and actuators: melting and collective plasmon resonances," *Nanoscale Research Letters*, vol. 1, no. 1, pp. 84–90, 2006.

[250] U. Hohenester and A. Trügler, "MNPBEM–a Matlab toolbox for the simulation of plasmonic nanoparticles," *Computer Physics Communications*, 2011.

P1

Publication 1

T. Salminen, M. Hahtala, I. Seppälä, T. Niemi, M. Pessa, “Pulsed laser deposition of yttria-stabilized zirconium dioxide with a high repetition rate picoseconds fiber laser,” *Applied Physics A*, Vol. 98, pp. 487-490, 2010.

Appl Phys A manuscript No.
(will be inserted by the editor)

Pulsed Laser Deposition of yttria-stabilized zirconium dioxide with a high repetition rate picosecond fiber laser

Turkka Salminen*, Mikko Hahtala, Ilkka Seppälä, Tapio Niemi, Markus Pessa

Optoelectronics Research Centre, Tampere University of Technology, Tampere, Finland

Received: date / Revised version: date

Abstract We report the use of a mode-locked fiber laser in Pulsed Laser Deposition (PLD) of yttria stabilized zirconium oxide. The fiber laser produces picosecond pulses with megahertz repetition rates at the wavelength of 1060 nm. We have investigated the effects of the time delay and the physical overlapping of the consecutive pulses on the ablation thresholds and the properties of the deposited films. Our results show existence of two distinct evaporation modes: 1) a single pulse evaporation mode observed for low overlapping and long time delays between the pulses and 2) a high repetition rate evaporation mode for high overlapping with short delays. The first mode is characterized by evaporation of nanoparticles and clusters and yields structured films with high surface area. The second mode yields smooth films, with evaporation characteristics closer to those of thermal evaporation than traditional PLD.

PACS: 81.15.Fg 42.55.Wd 68.55.-a

1 Introduction

Pulsed laser deposition, is a versatile method. Transfer of the stoichiometry of the target onto deposited films makes PLD well suited for deposition of complex materials, such as high-temperature superconductors[1], piezo- and ferroelectric[2] materials, and for prototyping new material compositions. PLD has become a powerful tool for materials research, but it's suitability for industrial applications has been very limited.

Gamaly et al. suggested the use of short low-energy pulses with megahertz range repetition rates as an approach to deposit particle-free high quality films [3,4]. This approach has, indeed, potential to increase the PLD growth rates closer to those required for volume production. The higher repetition rates can also change the involved processes significantly. In addition to incubation effects observed with successive, overlapping pulses[5–7] the short time delay between the pulses can cause thermal effects as well[8]. Understanding these effects is important when assessing whether the beneficial properties of PLD, namely preservation of stoichiometry, are retained in high repetition rate PLD.

2 Experiment

2.1 Experimental setup

In our experiments, thin films of yttria-stabilized zirconium oxide (YSZ) were deposited onto silicon substrates by evaporating a sintered, 8-mol% YSZ target. We used a mode-locked yttrium-doped fiber laser at the wavelength of 1060 nm (X-Lase 20 from Corelase, Finland). The pulse width was 20 ps and the repetition rate was varied between 1, 2 and 4 MHz.

The films were deposited at room temperature under vacuum conditions ($\sim 10^{-5}$mbar). The cube-shaped vacuum chamber holds the mechanics for substrate and target manipulation, Fig. 1. The incident angle of the laser beam was 45° relative to the target surface and the substrate was at an angle of 45° or 90° in respect to the incident plasma. To evaporate the target surface evenly, we slowly moved the target back and forth along the Y-axis, while a mirror scanner scanned the laser beam along the X-axis. The scanner speed on the X-axis was varied between 1mm/s and 1m/s. This variation adjusted the amount of overlapping between the consecutive pulses. The time delay between consecutive pulses was changed by varying the repetition rate of the pulses. The time delays between the pulses were 1μs, 500ns and 250ns.

Surface morphology of the deposited films was analyzed by means of scanning electron microscopy (SEM). Film thickness and the index of refraction were measured

* *email:* turkka.salminen@tut.fi

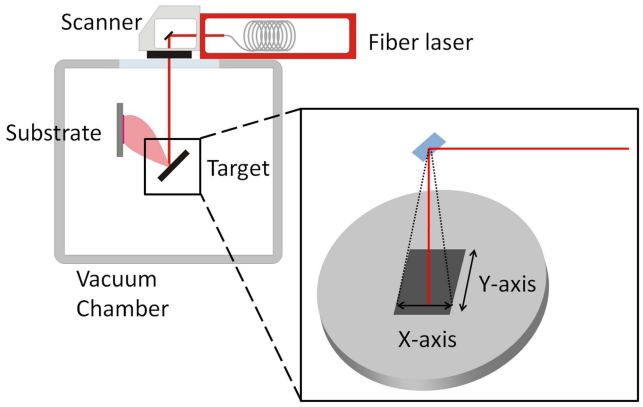

Fig. 1 Schematic diagram of the deposition system. The movement of the beam over the target is executed in the X-axis direction with a scanner and in the Y-axis direction by moving the target back and forth.

with an ellipsometer and by reflection measurements. The ablation threshold fluence, F_{th}, was estimated visually from the onset of visible plasma and measured with a crystal oscillator.

2.2 Effects of pulse overlapping

The number of overlapping pulses, N_p, can be calculated from the equation

$$N_p = f_{laser}\frac{D_{spot}}{v_{scan}} \quad (1)$$

where f_{laser} is the repetition rate of the laser, D_{spot} is the diameter of the laser spot and v_{scan} is the scanning speed of the laser beam including the X-direction movement by the mirror scanner and the slow Y-axis movement of the target (Fig. 1). Due to the overlapping of pulses, only a fraction of them interact with a clean target surface. Thus, the evaporation process and the observed thresholds can be very different compared to the case of a single non-overlapping pulse[8]. We must consider the different mechanisms in order to understand the evaporation process. What follows is a list of key items that need to be explored.

(i) Defects have an important role in the initial states of laser ablation.[5,9,10] They increase the absorption of light into the material and locally decrease the ablation threshold. The fluence required for defect formation by laser pulses is well below F_{th} and therefore accumulation of defects with overlapping pulses can lead to observation of significantly lowered ablation thresholds. It has been observed that the threshold lowering is saturated after certain amount of pulses. Rosenfeld et al. found the saturation for fused silica and CaF_2 to take place at $N_{p,sat}$ ≈20.[5] Whereas Mero et al. reported $N_{p,sat}$ ≈1000 for Ta_2O_5.[6] In our case the minimum N_p is about 17 (1MHz, 1m/s scanning speed), therefore all of the reported F_{th} values will include effects caused by the laser-induced defects.

(ii) Thermal effects - Each laser pulse causes a slight increase in the temperature of the interaction volume.[8] After a pulse, diffusion of heat and possibly material evaporation lower the local temperature until the next pulse arrives. For sufficiently high N_p the local temperature continues to rise until the interaction volume reaches a saturation temperature and the incoming laser energy is balanced by the losses caused by heat diffusion and possibly evaporation.

(iii) Changes in target stoichiometry - PLD preserves stoichiometry of a compound target better than any other evaporation method and transfers this stoichiometry to the growing film. However, the rising temperature leads to a possibility of thermal evaporation. Then the rate of evaporation of different elements becomes dependent on their respective vapor pressures, which may lead to changes in the stoichiometry of the target and subsequently, change the stoichiometry of the deposited films.

(iv) Non-equilibrium effects - The processes that follow the absorption of the short laser pulse have varying time-scales. These time-scales depend on the target material. Although the local thermalization between the electrons and the lattice typically take place in few picoseconds, the actual material evaporation can last even hundreds of nanoseconds, and resolidification of the target surface takes a few microseconds. For megahertz repetition rates, time delays between the consecutive pulses are in the range of tens or hundreds of nanoseconds. Therefore some of the evaporation processes are still ongoing as the next pulse hits the target.

(v) Plasma shielding - In case of very short pulse delays, the plasma evaporated by the previous pulse is still very close to the target. The dense plasma can absorb and scatter the energy of the laser pulse and effectively raise the threshold fluence.

3 Results and discussion

3.1 Threshold fluence

In our ablation experiments, the repetition rate of 1MHz at the maximum scanning speed corresponded to the lowest value of N_p ≈17, which yielded F_{th} ≈0.25J/cm^2. Increasing N_p to 170 lowered F_{th} to saturation value of 0.16J/cm^2 (Fig. 2). Further increase of N_p to 17 000 did not decrease the F_{th} anymore. For 2MHz and 4MHz repetition rates, F_{th} was 0.14J/cm^2 and 0.09J/cm^2 for a 1m/s scanning speed, respectively. The saturation threshold of 0.08J/cm^2 for 2MHz was obtained at N_p ≈700 and 0.03J/cm^2 for 4MHz at N_p ≈2000. Any further increase in N_p did not affect F_{th}. The threshold values for low N_p are nearly linearly dependent on the time between consecutive pulses for the studied repetition rates. For low repetition rates (<1kHz) it has been observed that

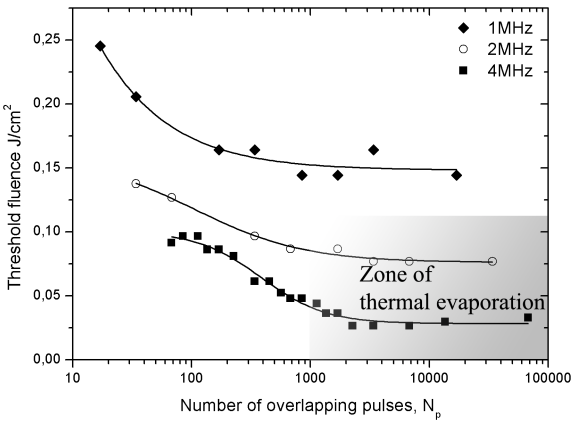

Fig. 2 Threshold fluences for 1, 2 and 4MHz repetition rates as a function of the number of overlapping pulses. The lines are guides for the eye.

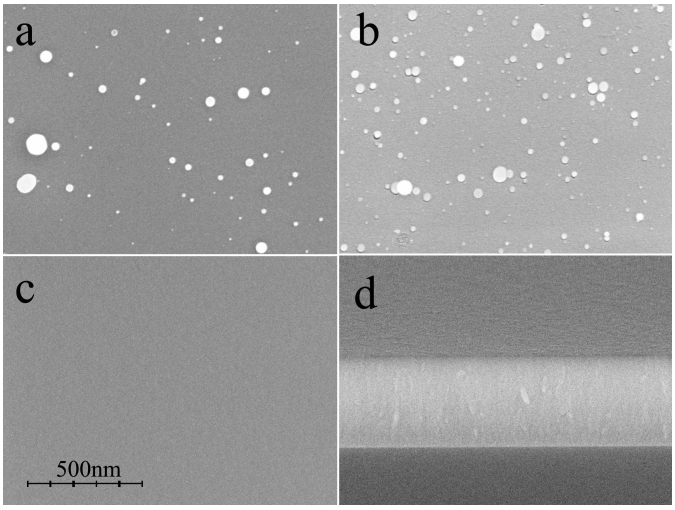

Fig. 3 Scanning electron microscope images of YSZ films. (a) Films deposited at a 1MHz repetition rate consist of nanoparticles. At 2MHz and 4MHz repetition rates the quality of the film depends on the amount of pulse overlapping. (b) Low overlapping yields films with nanoparticles, whereas high overlapping yields very smooth and particle free films (c and d). Panel d is a cross-section of the film in panel c.

the time between the pulses has no impact on the thresholds[6], but clearly that is not the case for MHz repetition rates.

It was found that the color of the target changes from white to dark during evaporation, indicating changes in stoichiometry of the surface layer of the target. Scanning repeatedly over the same, already darkened target area with a constant scanning speed did not lower F_{th} any further even as the pulses accumulated during several scans. The threshold was thus defined by N_p of a single scanning pass. Therefore it becomes clear that the formation of defects and further changes in target stoichiometry do not explain the observed behavior of F_{th} as a function of N_p. These observations suggest that the thermal mechanisms are significant in the evaporation process.

When compared to the threshold value of 1.64 J/cm^2 for rough YSZ coatings reported for single femtosecond pulses by Das et al.[7] our measured values are significantly lower. The saturation value they measured for N_p >500 was approximately 0.5 J/cm^2 which is still larger than our highest values by a factor of two. This shows that the short time delay has a significant impact on the threshold values.

Our explanation for the behavior of F_{th} as a function of N_p is related to cumulative local heating of the target by overlapping pulses. Rising temperature lowers F_{th}. Furthermore, if temperature is high enough, thermal evaporation begins, and with high enough repetition rate thermal evaporation can be sustained even if the pulse fluence itself is too low to cause evaporation. In the case of thermal evaporation the threshold is defined rather by the laser average power than the fluence of single pulses. Due to shorter pulse delays, i.e. shorter time for heat diffusion, the higher repetition rates can sustain the evaporation temperature with lower fluences.

3.2 Film deposition

The films deposited at the repetition rate of 1MHz consist of nanoparticles, particle clusters and small droplets regardless of the scanning speed (Fig 3a). For 2MHz and 4MHz, N_p has remarkable consequences on surface morphology. It can be seen from Fig. 3 that deposition with low N_p yields morphology similar to that obtained at 1MHz (Fig 3b). In sharp contrast, the films deposited in the saturation regime are smooth and particle-free (Fig 3c and 3d). We note that the films would consist of particles regardless of N_p if F_{th} were approximately 0.1 J/cm^2, which is about the ablation threshold at 1MHz. The index of refraction, n, for the smooth films, when the direction of the plasma was perpendicular to the surface of the substrate, was 2.1, while the films deposited at 45° turned out to be less dense exhibiting n =1.9.

Morphology of the films produced with small N_p was very similar to the films reported for femtosecond-pulse depositions[11,12]. This similarity suggests that the formation of nanoparticles is inherent to evaporation with ultra-short pulses. The particles are generated probably through fragmentation[13,14]. In our experiment, the wavelength of 1064 nm can also enhance particle generation due to longer absorption length and consequent distribution of the pulse energy into a larger volume.

The smooth films in the saturation regime for 2MHz and 4MHz can be accounted for by local thermal evaporation. The fluences are too low for individual pulses to cause evaporation. However, due to the poor thermal conduction of YSZ the local temperature of the area exposed to the pulses can exceed the evaporation temperature. Due to the thermal nature of this process, it is very likely that the stoichiometry of the deposited films dif-

fers from that of the target. In this case the evaporation rate is almost constant and the density of the plasma is likely to remain so low that no formation of particles takes place. Yet, for fluence above $0.1\mathrm{J/cm^2}$ particles are found on the films, suggesting that the individual pulses can cause direct evaporation causing a shift into the pulsed evaporation regime.

For 1MHz, no regime of thermal evaporation was observed. Saturation F_{th} of $0.16\mathrm{J/cm^2}$ is above the threshold that causes particles to emerge with 2MHz and 4MHz repetition rates. This suggests that for 1MHz the evaporation is still caused primarily by the individual pulses.

Finally, the different evaporation regimes may be distinguished from the visual appearance of the plasma. The plasma for low N_p has a bright, directed core, whereas the plasma produced with high N_p is broad and diffuse implying that thermal evaporation in this case dominates the evaporation process.

4 Conclusions

We have applied a picosecond pulse fiber laser to examine the influence of the pulse overlapping and pulse delay on the threshold fluence and the morphology of the deposited YSZ films. The pulse overlapping was observed to cause significant lowering of the ablation threshold which is attributed to formation of defects, changes in target stoichiometry and cumulative heating. The defects and especially the changes in the stoichiometry explain the significant differences to previously reported thresholds, whereas heating is the predominant cause for the observed threshold behavior as a function of the number of the overlapping pulses. In PLD-experiments, two distinct regimes of evaporation with very different film morphologies were found. Films deposited in the pulsed laser deposition-mode with small pulse overlapping yield high surface area films that consist of nanoparticles and particle clusters; a result typical to films deposited with ultra-short pulses. As the number of overlapping pulses is increased above a repetition rate dependent threshold the deposited films are smooth and particulate free. This deposition mode is attributed to local thermal evaporation caused by the cumulative heating effects and is made possible by the very high repetition rate of the laser.

Acknowledgements

This work was funded by the Finnish funding agency for technology and innovation (TEKES) through the project "Ultra-short-pulse fiber laser deposition of functional thin films" (PULSAR), project number: 1900/31/06. Turkka Salminen would also like to thank Jenny and Antti Wihuri Foundation for support.

References

1. D.Dijkkamp, T. Venkatesan, X.D. Wu, S.A. Shaheen, Y.H. Min-Lee, W.L. McLean and M. Croft, Appl. Phys. Lett. **51,** (1987) 619.
2. R. Ramesh, K. Luther, B. Wilkens, D.L. Hart, E. Wang, J.M. Tarascon, A. Inam, X.D. Wu and T. Venkatesan, Appl. Phys. Lett. **57,** (1990) 1505.
3. E.G. Gamaly, A.V. Rode and B. Luther-Davies, J. Appl. Phys. **85,** (1999) 4213.
4. A.V. Rode, B. Luther-Davies and E.G. Gamaly, J. Appl. Phys. **85,** (1999) 4222.
5. A. Rosenfeld, M. Lorenz, R. Stoian, D. Ashkenasi, Appl. Phys. A **69,** (1999) S373.
6. M. Mero, B. Clapp, J.C. Jasapara, W. Rudolph, D. Ristau, K. Starke, J. Krger, S. Martin, W. Kautek, Opt. Eng. **44,** (2005) 051107.
7. D.K. Das, J.P. McDonald, S.M. Yalisove, T.M. Pollock, Appl. Phys. A **91,** (2008) 421.
8. B. Luther-Davies, A.V. Rode, N. Madsen, E. Gamaly, Opt. Eng. **44,** (2005) 051102.
9. R.L. Webb, L.C. Jensen, S.C. Langford, J.T. Dickinson, J. Appl. Phys. **74,** (1993) 2323.
10. K. Hattori, A. Okano, Y. Nakai, N. Itoh, Phys. Rev. B. **45,** (1992) 8424.
11. S. Amoruso, G. Ausanio, R. Bruzzese, M. Vitiello, X. Wang, Phys. Rev. B **71,** (2005) 033406.
12. R. Teghil, A. De Bonis, A. Galasso, P. Villani, A. Santagata, App. Surf. Sci. **254,** (2007) 1220.
13. S. Amoruso, R. Bruzzese, X. Wang, N.N. Nedialkov and P.A. Atanasov, J. Phys. D. **40,** (2007) 331.
14. M.E. Povarnitsyn, T.E. Itina, M. Sentis, K. V. Khishchenko and P.R. Levashov, Phys Rev. B **75,** (2007) 235414.

Publication 2

P2

T. Salminen, M. Hahtala, I. Seppälä, P. Laukkanen, T. Niemi, ''Picosecond pulse laser ablation of yttria-stabilized zirconia from kilohertz to megahertz repetition rates'', *Applied Physics A*, Vol. 101, pp. 735-738, 2010

Appl Phys A manuscript No.
(will be inserted by the editor)

Picosecond pulse laser ablation of yttria-stabilized zirconia from kilohertz to megahertz repetition rates

Turkka Salminen*[1], Mikko Hahtala[1], Ilkka Seppälä[1], Pekka Laukkanen[2], Tapio Niemi[1]

[1] Optoelectronics Research Centre, Tampere University of Technology, Tampere, Finland
[2] Department of Physics and Astronomy, University of Turku, FI-20014 Turku, Finland

Received: date / Revised version: date

Abstract Thin films of yttria stabilized zirconia were deposited onto silicon substrates using high repetition rate picosecond pulse lasers. The applied lasers covered the repetition rate range from 10kHz to 4MHz. We found that the laser pulse overlapping which results from increased repetition rates led to considerable changes in the ablation process. Defect formation and local heating lead to lower ablation thresholds and, with sufficiently high repetition rates, to melting of the target and even to thermal evaporation. We found that yttria-stabilized zirconia (YSZ) films deposited with picosecond pulses at 1064 nm wavelength below repetition rates of 2MHz have rough, nanostructured morphology and the same atomic ratio of yttrium and zirconium as the target. Films deposited with 2MHz and higher repetition rates with high number of overlapping pulses are very smooth, but are yttrium deficient, providing evidence of the importance of the thermal processes.

PACS: 81.15.Fg 42.55.Wd 68.55.-a

1 Introduction

Pulsed laser deposition (PLD) can be used to produce high quality films while preserving the stoichiometry of complex materials. However, commercial applications have been limited due to the rather small scale of typical PLD-systems, resulting in low deposition rates and high costs.

Typical PLD-systems use a laser with repetition rate in the order of a few tens of hertz. It has been proposed that PLD could reach higher deposition rates by using ultra-short pulse lasers with high repetition rates [1,2]. However, it has also been shown that ultra-short pulse laser evaporation produces nanoparticles instead of smooth, homogenous films [3,4]. A recent study of pulsed laser deposition with a high repetition rate picosecond fiber laser found two distinct deposition regimes [5]. A pulsed evaporation mode with separate pulses led to deposition of nanoparticles, whereas overlapping high repetition rate pulses led to a thermal evaporation mode which yielded smooth films.

The evaporation and deposition process is controlled by the interplay of many parameters, which govern the properties of the deposited film. In this work we elucidate the roles of the repetition rate, pulse overlapping and laser wavelength in picosecond pulse laser deposition. We extend the results previously achieved with megahertz repetition rate lasers towards the kilohertz range, and compare the morphology and stoichiometry of the films deposited in both the pulsed evaporation mode and the thermal evaporation mode. We also extend the ablation threshold behavior to cover the range from single pulse evaporation at 10kHz to approximately 60 000 overlapping pulses at 4MHz repetition rate.

Due to their hardness and chemical inertness yttria-stabilized zirconia films have many applications including thermal barrier coatings, tribological coatings and solid electrolytes in solid oxide fuel cells. Their good optical properties make them an excellent choice for hard optical coatings which can be further functionalized by rare-earth metal dopants. Whereas some applications can benefit from the extraordinary properties of nanostructured films, optical hard coatings require smooth, homogenous, high quality films. High repetition rate pulsed laser deposition is an interesting technique as it allows deposition of both. In our experience, the general features of the deposition process are similar for most insulating oxides including zirconium oxide, aluminium oxide and titanium oxide. Therefore the results presented here can, to some extent, be generalized to other similar materials even though the exact parameters will vary. In this paper we have focused on yttria-stabilized zirconia partly due to its multicomponent nature which allows us to study the effects of the deposition parameters on the film stoichiometry.

* *email:* turkka.salminen@tut.fi

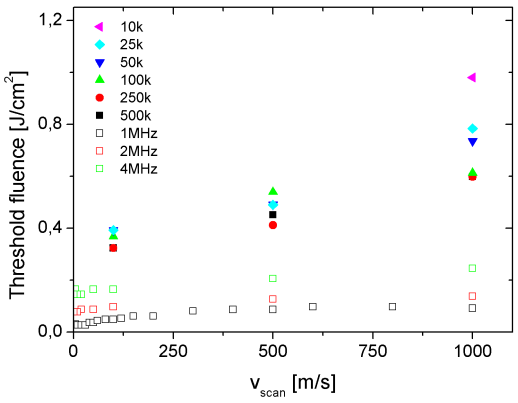

Fig. 1 Threshold fluences as a function of the scanning speed.

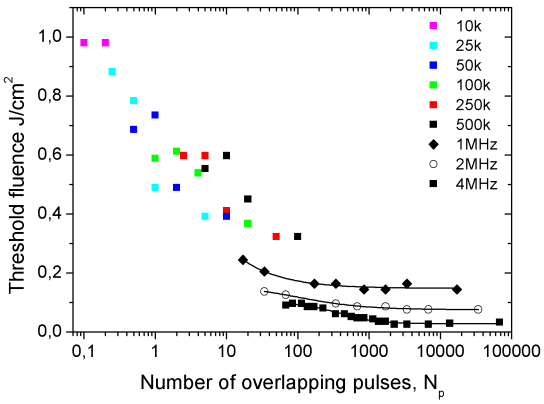

Fig. 2 Threshold fluences as a function of the number of overlapping pulses per single sweep. The lines in the fiber laser data [5] are guides for the eye.

2 Experiment

The experiments were performed with two lasers to cover a wide repetition rate range. A Lumera Super Rapid Nd:YVO_4 solid state laser generated 15 picosecond pulses with repetition rates from 10kHz to 500kHz and the megahertz range from 1MHz to 4MHz was covered with a Corelase X-Lase fiber laser producing 20 picosecond pulses at a wavelength of 1060 nm. To study the effect of the wavelength, the Nd:YVO4 solid state laser was used both at the primary wavelength of 1064 nm and at the third harmonic of 355 nm.

The film deposition and threshold measurements were performed at room temperature, under vacuum conditions (10^{-4}mbar). To evaporate the target surface evenly, we used a combination of a moving target and a mirror scanner to raster the target. Due to the limited scanning speed of approximately 1 m/s and the high repetition rates of several megahertz, the successive pulses overlap instead of hitting a fresh, unablated spot. Therefore, the scanning speed adds another process parameter as it controls the number of overlapping pulses, N_p, hitting the same spot on a single scanning sweep. In a previous study it was found that the observed evaporation behavior for megahertz pulse trains depends on N_p instead of the total number of accumulated pulses [5]. The reference also contains a more detailed description of the deposition system.

The evaporation targets were 5-mol% yttria-stabilized zirconium oxide (YSZ, Goodfellow #128-868-36) and the films were deposited onto silicon substrates. The film and target morphology was examined with a scanning electron microscope (SEM). The stoichiometry of the samples was measured with x-ray photoelectron spectroscopy (XPS) using Mg K_α radiation. The ablation thresholds were defined using a crystal oscillator and also estimated visually from the onset of the visible plasma.

3 Results and discussion

3.1 Threshold fluence

The ablation threshold fluences, F_{th}, were measured for selected repetition rates by varying the scanning speed. An inspection of the thresholds as a function of the scanning speed (Fig. 1) reveals the trend of decreasing thresholds with decreasing scanning speed. Increasing the repetition rate also considerably lowers the F_{th}.

When the data is presented as a function of the number of overlapping pulses during a single scanning sweep (Fig. 2), the correlation between N_p and F_{th} seems evident. The initial decrease in the thresholds as the N_p increases is most likely caused by defect formation [8–10] and to some extent by the residual heat from the previous pulses. With kilohertz repetition rates the heat can be conducted several micrometers between successive pulses which, in addition to heating, can lead to defect formation in the immediate neighborhood of the ablated region. This is observed as lower thresholds even before the pulses actually overlap ($N_p < 1$). The previously reported saturation behavior in the megahertz repetition range [5] fits well with the data. The saturation behavior can be explained by considering the heating effect caused by each laser pulse. As the number of pulses is increased, the temperature rises until saturation is reached when the heating is balanced by heat conduction. Higher repetition rates allow higher temperatures to be reached as the delay between the pulses is shorter and there is less time for heat conduction. Depending on the material and laser parameters, the saturation temperature can be high enough for melting or even thermal evaporation of the target to occur. In the latter case the nature of the evaporation process changes considerably as the evaporation is not caused directly by the high energy pulses, but by the high local temperature.

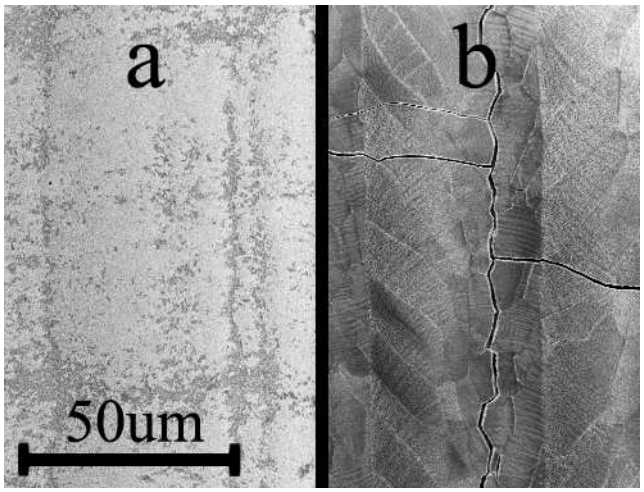

Fig. 3 (a) Target surface after evaporation with 500kHz repetition rate, ($N_p \approx 10$), shows no signs of melting. (b) The surface of the target after evaporation with 4MHz, ($N_p \approx 14000$), has melted and cracked during solidification.

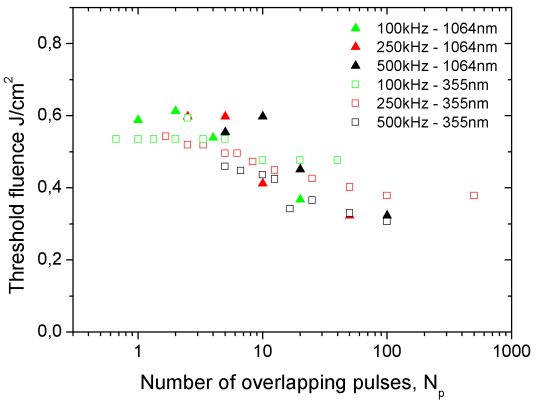

Fig. 4 Comparison of the ablation thresholds for 355 nm and 1064 nm wavelengths.

An SEM inspection of the targets (Fig. 3) confirms the difference between the evaporation mechanisms associated with low ($N_p \approx 10$) and high ($N_p \approx 14000$) numbers of overlapping pulses. The surface of a target evaporated with 500kHz repetition rate, shown in fig. 3a shows no signs of melting, whereas the target evaporated with a 4MHz repetition rate, shown in fig. 3b shows that the whole surface layer has melted and cracked during solidification.

Quite surprisingly, the threshold values do not seem to depend significantly on the wavelength, as can be seen from figure 4.

3.2 Film deposition

Films deposited with individual pulses or a low number of overlapping pulses consist of nanoparticles regardless of the repetition rate (Figs. 5a, 5b and 5c) or the wavelength (film deposited with 355nm is not shown here as its morphology is identical to that shown in Fig. 5a). The film morphology is similar to what is typically reported for femtosecond pulse laser deposition [3,4]. For the samples in figures 5b and 5c we deposited very thin layers of material to allow inspection of the individual particles. The sample in figure 5a, deposited with 500kHz, shows more irregular, fragment-like particles, compared to those deposited at higher repetition rates. As previously reported, increasing the repetition rate and the number of the overlapping pulses leads to local thermal evaporation which produces smooth films, as can be seen in figure 5d [5]. In the case of YSZ, the thermal evaporation regime can be reached when the repetition rate is 2MHz or above. For repetition rates of 1MHz and below the deposited films consist of nanoparticles, regardless of the number of overlapping pulses. Allowing for a suitable laser, it would be interesting to study whether the thermal evaporation regime can be reached with a wavelength of 355 nm.

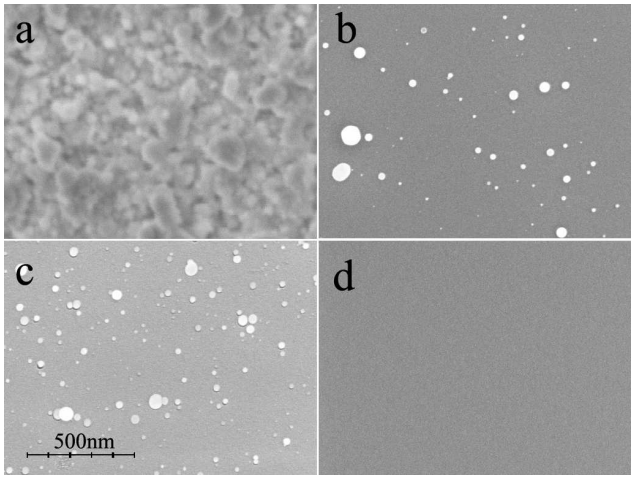

Fig. 5 SEM images of the samples deposited at 1064nm wavelength. Films were deposited with (a) 500kHz, (b) 1MHz, (c) and (d) 4MHz repetition rate. In samples (a), (b) and (c), the scanning speed was 1m/s, whereas sample (d) was deposited with a scanning speed of 0.005m/s. On samples (b) and (c) a thinner layer of material was deposited to allow inspection of the individual particles.

One of the major benefits of PLD is the transfer of the target stoichiometry onto the deposited films. As the number of overlapping pulses is increased, the stoichiometry of the films can also change due to thermal effects. To examine the transfer of the stoichiometry, we studied the target and the deposited films with XPS. The peak intensities of Y3d and Zr3d emissions and the atomic sensitivity factors, 1.867 for Y3d and 2.216 for Zr3d, were used to determine the yttrium contents, $Y/(Y+Zr)$, for the films and the target. The absolute yttrium contents were not of primary interest. However, a systematic determination of the yttrium ratios provides a meaningful comparison between the different samples and the

Table 1 The results of the XPS measurements.

Sample	λ $[nm]$	f_{laser} $[MHz]$	N_p	Y/(Y+Zr) -%
Target	-	-	-	5.1%
1	1064	0.5	10	5.2%
2	355	0.5	10	5.8%
3	1064	1	17	5.3%
4	1064	4	68	4.8%
5	1064	4	13600	3.8%
6	1064	4	13600	4.2%

target. The $Y/(Y + Zr)$-content of the target material was found to be 5.1%. Our measurement result is considerably lower than the 9.5% reported by the material supplier. However, the exact values are not essential for our comparative study. The measurement data for the deposited films is listed in table 1.

Samples 1 and 3, deposited with a wavelength of 1064 nm and low pulse overlapping, show very similar stoichiometry with the target. Increasing the repetition rate to 4 MHz resulst in a slight decrease of the yttrium content even with maximum scanner speed (sample 4) and as the number of overlapping pulses is further increased, the films have approximately 1% lower yttrium content than the target (samples 5 and 6). Sample 2, deposited with 355 nm wavelength, exhibits the opposite behavior. The yttrium content on the film is actually higher than that of the target. This is an interesting finding and should be studied further to clarify whether the wavelength can be utilized to tune the composition.

In previous studies of excimer laser PLD with nanosecond pulses, the Y/Zr ratio of the deposited films was found to match that of the target, if the fluence was at least approximately two times higher than the ablation threshold. Deposition very close to the ablation threshold led to deposition of yttrium deficient films [6]. Purely thermal processes like electron-beam evaporation have been reported to cause a significant loss of yttrium of up to 30% during the deposition [7]. In our experiments all of the samples were deposited with fluences only slightly above the ablation threshold, with fluences considerably smaller than two times F_{th}. However, in our experiments the yttrium loss was not observed for films deposited with low N_p. The yttrium loss was observed only when N_p was increased. Our findings show that near-threshold yttrium loss is not an issue with picosecond pulses. It also suggests that the nature of the process indeed changes towards thermal evaporation with increasing N_p and that the yttrium loss mechanisms are similar to the case of electron beam evaporation.

4 Conclusions

The increasing repetition rate was found to lower the ablation threshold. Decreasing the scanning speed and thereby increasing the number of overlapping pulses further decreases the thresholds, until saturation is reached as the thermal conduction balances the accumulating surplus heat from the laser pulses. Picosecond pulse evaporation of YSZ was found to produce nanoparticles, which is typical for ultra short pulse evaporation. Increasing the repetition rate above 2MHz, however, allows local thermal evaporation, yielding smooth films. In an XPS study, the pulsed evaporation at 1064nm wavelength was found to transfer the stoichiometry of the target material onto the deposited films. The change of the evaporation regime, from pulsed to thermal, led to deposition of yttrium deficient films.

Acknowledgements

This work was funded by the Finnish funding agency for technology and innovation (TEKES) through the project "Ultra-short-pulse fiber laser deposition of functional thin films" (PULSAR), project number: 1900/31/06. Turkka Salminen would also like to thank the Jenny and Antti Wihuri Foundation for support.

References

1. E.G. Gamaly, A.V. Rode and B. Luther-Davies, J. Appl. Phys. **85,** (1999) 4213.
2. A.V. Rode, B. Luther-Davies and E.G. Gamaly, J. Appl. Phys. **85,** (1999) 4222.
3. S. Amoruso, G. Ausanio, R. Bruzzese, M. Vitiello, X. Wang, Phys. Rev. B **71,** (2005) 033406.
4. R. Teghil, A. De Bonis, A. Galasso, P. Villani, A. Santagata, App. Surf. Sci. **254,** (2007) 1220.
5. T. Salminen, M. Hahtala, I. Seppälä, T. Niemi and M. Pessa, Appl. Phys. A **98**, 487, (2010).
6. F. Kokai, K. Amano, H. Ota, Y. Ochiai and F. Umemura, J. Appl. Phys. **72,** (1992) 699.
7. M. Hartmanova, M. Jergel, V. Navratil, K. Navratil, K Gmucova, F.D. Gandarilla, J. Zemek, S. Chromika nd F. Kundracik, Proceedings of the International Workshop Physics and Technology of Thin Films IWTF 2003, (2004) 158.
8. A. Rosenfeld, M. Lorenz, R. Stoian, D. Ashkenasi, Appl. Phys. A **69,** (1999) S373.
9. R.L. Webb, L.C. Jensen, S.C. Langford, J.T. Dickinson, J. Appl. Phys. **74,** (1993) 2323.
10. K. Hattori, A. Okano, Y. Nakai, N. Itoh, Phys. Rev. B. **45,** (1992) 8424.

Publication 3

P3

T. Salminen, J. Dahl, M. Tuominen, P. Laukkanen, E. Arola, T. Niemi, ''Single-step fabrication of luminescent GaAs nanocrystals by pulsed laser ablation in liquids'', *Optical Materials Express*, Vol. 2, No. 6, pp. 799-813, 2012

Single-step fabrication of luminescent GaAs nanocrystals by pulsed laser ablation in liquids

Turkka Salminen,[1,*] Johnny Dahl,[2] Marjukka Tuominen,[2] Pekka Laukkanen,[2] Eero Arola,[1] and Tapio Niemi[1]

[1]*Optoelectronics Research Centre, Tampere University of Technology, FI-33720 Tampere, Finland*
[2]*Department of Physics and Astronomy, University of Turku, FI-20014 Turku, Finland*
**turkka.salminen@tut.fi*

Abstract: Optical absorption and emission properties of gallium arsenide nanocrystals can be tuned across the visible spectrum by tuning their size. The surface of pure GaAs nanocrystals tends to oxidize, which deteriorates their optical properties. In order to prevent the oxidization, surface passivation has been previously demonstrated for GaAs nanocrystals larger than the Bohr exciton radius. In this paper, we study synthesis of small GaAs nanocrystals by pulsed laser ablation in liquids combined with simultaneous chemical surface passivation. The fabricated nanocrystals are smaller than the Bohr exciton radius and exhibit photoluminescence peaked near 530 nm due to quantum confinement. The photoluminescence properties are stable for at least six months, which is attributed to successful surface passivation. The chemical structure of the nanocrystals and changes caused by thermal annealing are elucidated with Raman spectroscopy, transmission electron microscopy and x-ray photoelectron spectroscopy.

OCIS codes: (160.4236) Nanomaterials; (160.4670) Optical materials; (250.5230) Photoluminescence; (350.3850) Materials processing.

References and links

1. L. E. Brus, "Electron–electron and electron-hole interactions in small semiconductor crystallites: The size dependence of the lowest excited electronic state," J. Chem. Phys. **80**(9), 4403–4409 (1984).
2. M. A. Olshavsky, A. N. Goldstein, and A. P. Alivisatos, "Organometallic synthesis of gallium-arsenide crystallites, exhibiting quantum confinement," J. Am. Chem. Soc. **112**(25), 9438–9439 (1990).
3. H. Uchida, C. J. Curtis, and A. J. Nozik, "Gallium arsenide nanocrystals prepared in quinoline," J. Phys. Chem. **95**(14), 5382–5384 (1991).
4. S. S. Kher and R. L. Wells, "A straightforward, new method for the synthesis of nanocrystalline GaAs and GaP," Chem. Mater. **6**(11), 2056–2062 (1994).
5. M. A. Malik, P. O'Brien, S. Norager, and J. Smith, "Gallium arsenide nanoparticles: synthesis and characterisation," J. Mater. Chem. **13**(10), 2591–2595 (2003).
6. M. A. Malik, M. Afzaal, P. O'Brien, U. Bangert, and B. Hamilton, "Single molecular precursor for synthesis of GaAs nanoparticles," Mater. Sci. Technol. **20**(8), 959–963 (2004).
7. U. Uchida, C. J. Curtis, P. V. Kamat, K. M. Jones, and A. J. Nozik, "Optical properties of gallium arsenide nanocrystals," J. Phys. Chem. **96**(3), 1156–1160 (1992).
8. J. Perrière, E. Millon, M. Chamarro, M. Morcrette, and C. Andreazza, "Formation of GaAs nanocrystals by laser ablation," Appl. Phys. Lett. **78**(19), 2949–2951 (2001).
9. A. A. Lalayan, "Formation of colloidal GaAs and CdS quantum dots by laser ablation in liquid media," Appl. Surf. Sci. **248**(1-4), 209–212 (2005).
10. R. A. Ganeev, M. Baba, A. I. Ryasnyansky, M. Suzuki, and H. Kuroda, "Laser ablation of GaAs in liquids: structural, optical, and nonlinear optical characteristics of colloidal solutions," Appl. Phys. B **80**(4-5), 595–601 (2005).
11. M. C. Traub, J. S. Biteen, B. S. Brunschwig, and N. S. Lewis, "Passivation of GaAs nanocrystals by chemical functionalization," J. Am. Chem. Soc. **130**(3), 955–964 (2008).
12. Y. Nannichi, J. Fan, H. Oigawa, and A. Koma, "A model to explain the effective passivation of the GaAs surface by $(NH_4)_2S_x$ treatment," Jpn. J. Appl. Phys. **27**(Part 2, No. 12), L2367–L2369 (1988).
13. T. Salminen, M. Hahtala, I. Seppälä, P. Laukkanen, and T. Niemi, "Picosecond pulse laser ablation of yttria-stabilized zirconia from kilohertz to megahertz repetition rates," Appl. Phys., A Mater. Sci. Process. **101**(4), 735–738 (2010).

#165524 - $15.00 USD Received 26 Mar 2012; revised 20 Apr 2012; accepted 10 May 2012; published 14 May 2012

14. A. K. Arora, M. Rajalakshmi, and T. R. Ravindran, "Phonon confinement in nanostructured materials," in *Encyclopedia of Nanoscience and Nanotechnology*, H. S. Nalwa, ed. (American Scientific Publishers, Los Angeles, 2004), Vol. 8, pp.409–512.
15. G. Burns, F. H. Dacol, C. R. Wie, E. Burstein, and M. Cardona, "Phonon shifts in ion bombarded GaAs: Raman measurements," Solid State Commun. **62**(7), 449–454 (1987).
16. I. D. Desnica, M. Ivanda, M. Kranjček, R. Murri, and N. Pinto, "Raman study of gallium arsenide thin films," J. Non-Cryst. Solids **170**(3), 263–269 (1994).
17. G. P. Schwartz, B. Schwartz, D. DiStefano, G. J. Gualtieri, and J. E. Griffiths, "Raman scattering from anodic oxide-GaAs interfaces," Appl. Phys. Lett. **34**(3), 205–207 (1979).
18. Y. Takagaki, E. Wiebicke, M. Ramsteiner, L. Däweritz, and K. H. Ploog, "Spontaneous growth of arsenic oxide micro-crystals on chemically etched MnAs surfaces," Appl. Phys., A Mater. Sci. Process. **76**(5), 837–840 (2003).
19. I. H. Campbell and P. M. Fauchet, "CW laser irradiation of GaAs: Arsenic formation and photoluminescence degradation," Appl. Phys. Lett. **57**(1), 10–12 (1990).
20. H. Richter, Z. P. Wang, and L. Ley, "The one phonon Raman spectrum in microcrystalline silicon," Solid State Commun. **39**(5), 625–629 (1981).
21. A. K. Arora, M. Rajalakshmi, T. R. Ravindran, and V. Sivasubramanian, "Raman spectroscopy of optical phonon confinement in nanostructured materials," J. Raman Spectrosc. **38**(6), 604–617 (2007).
22. D. Strauch and B. Dorner, "Phonon dispersion in GaAs," J. Phys. Condens. Matter **2**(6), 1457–1474 (1990).
23. R. K. Chang, J. M. Ralston, and D. E. Keating, in *Light Scattering Spectra of Solids,* G. B. Wright, ed. (Springer–Verlag, New York, 1969), p. 369.
24. H. Campbell and P. M. Fauchet, "The effects of microcrystal size and shape on the one phonon Raman spectra of crystalline semiconductors," Solid State Commun. **58**(10), 739–741 (1986).
25. J. Zi, K. Zhang, and X. Xie, "Comparison of models for Raman spectra of Si nanocrystals," Phys. Rev. B **55**(15), 9263–9266 (1997).
26. E. A. Rochette, B. C. Bostick, G. Li, and S. Fendorf, "Kinetics of arsenate reduction by dissolved sulfide," Environ. Sci. Technol. **34**(22), 4714–4720 (2000).
27. G. Scamarcio, A. Cingolani, M. Lugarà, and F. Lévy, "Resonant Raman effects at the indirect band gaps of GaS," Phys. Rev. B Condens. Matter **40**(3), 1783–1789 (1989).
28. G. W. Yang, "Laser ablation in liquids: Applications in the synthesis of nanocrystals," Prog. Mater. Sci. **52**(4), 648–698 (2007).
29. T. Fanaei and C. Aktik, "Passivation of GaAs using P_2S_5/$(NH_4)_2S$+Se and $(NH_4)_2S$+Se," J. Vac. Sci. Technol. A **22**, 874–878 (2004).
30. D. Peide, "Main determinants for III–V metal-oxide-semiconductor field-effect transistors," J. Vac. Sci. Technol. A **26**, 697–704 (2007).
31. J. G. Díaz and G. W. Bryant, "Electronic and optical fine structure of GaAs nanocrystals: The role of d orbitals in a tight-binding approach," Phys. Rev. B **73**(7), 075329 (2006).
32. J. J. Jancu, R. Scholz, F. Beltram, and F. Bassani, "Empirical spds* tight-binding calculation for cubic semiconductors: General method and material parameters," Phys. Rev. B **57**(11), 6493–6507 (1998).
33. J. S. Blakemore, "Semiconducting and other major properties of gallium arsenide," J. Appl. Phys. **53**(10), R123–R181 (1982).
34. G. E. Fenner, "Effect of hydrostatic pressure on the emission from gallium arsenide lasers," J. Appl. Phys. **34**(10), 2955–2957 (1963).
35. U. D. Venkateswaran, L. J. Cui, B. A. Weinstein, and F. A. Chambers, "Forward and reverse high-pressure transitions in bulklike AlAs and GaAs epilayers," Phys. Rev. B Condens. Matter **45**(16), 9237–9247 (1992).
36. C. L. Hinkle, M. Milojevic, B. Brennan, A. M. Sonnet, F. S. Aguirre-Tostado, G. J. Hughes, E. M. Vogel, and R. M. Wallace, "Detection of Ga suboxides and their impact on III–V passivation and Fermi-level pinning," Appl. Phys. Lett. **94**(16), 162101 (2009).
37. V. Polojärvi, J. Salmi, A. Schramm, A. Tukiainen, M. Guina, J. Pakarinen, E. Arola, J. Lång, I. J. Väyrynen, and P. Laukkanen, "Effects of $(NH_4)_2S$ and NH_4OH surface treatments prior to SiO_2 capping and thermal annealing on 1.3 μm GaInAsN/GaAs quantum well structures," Appl. Phys. Lett. **97**(11), 111109 (2010).
38. J. Dahl, V. Polojärvi, J. Salmi, P. Laukkanen, and M. Guina, "Properties of the SiO_2- and SiN_x-capped GaAs(100) surfaces of GaInAsN/GaAs quantum-well heterostructures studied by photoelectron spectroscopy and photoluminescence," Appl. Phys. Lett. **99**(10), 102105 (2011).
39. D. J. Lockwood, P. Schmuki, H. J. Labbé, and J. W. Fraser, "Optical properties of porous GaAs," Physica E **4**(2), 102–110 (1999).
40. N. Dmitruk, S. Kutovyi, I. Dmitruk, I. Simkiene, J. Sabataityte, and N. Berezovska, "Morphology, Raman scattering and photoluminescence of porous GaAs layers," Sens. Actuators B Chem. **126**(1), 294–300 (2007).
41. W. C. W. Chan and S. Nie, "Quantum dot bioconjugates for ultrasensitive nonisotopic detection," Science **281**(5385), 2016–2018 (1998).
42. J. M. Phillips, M. E. Coltrin, M. H. Crawford, A. J. Fischer, M. R. Krames, R. Mueller-Mach, G. O. Mueller, Y. Ohno, L. E. S. Rohwer, J. A. Simmons, and J. Y. Tsao, "Research challenges to ultra-efficient inorganic solid-state lighting," Laser Photonics Rev. **1**(4), 307–333 (2007).
43. Q. Li, C. Liu, Z. Liu, and Q. Gong, "Broadband optical limiting and two-photon absorption properties of colloidal GaAs nanocrystals," Opt. Express **13**(6), 1833–1838 (2005).

#165524 - $15.00 USD Received 26 Mar 2012; revised 20 Apr 2012; accepted 10 May 2012; published 14 May 2012

44. C. Wetzel and T. Detchprohm, "Wavelength-stable rare earth-free green light-emitting diodes for energy efficiency," Opt. Express **19**(S4 Suppl 4), A962–A971 (2011).
45. R. M. Farrell, E. C. Young, F. Wu, S. P. DenBaars, and J. S. Speck, "Materials and growth issues for high-performance nonpolar and semipolar light-emitting devices," Semicond. Sci. Technol. **27**(2), 024001 (2011).
46. H. Zhao, G. Liu, J. Zhang, J. D. Poplawsky, V. Dierolf, and N. Tansu, "Approaches for high internal quantum efficiency green InGaN light-emitting diodes with large overlap quantum wells," Opt. Express **19**(S4 Suppl 4), A991–A1007 (2011).
47. J.-P. Sylvestre, A. V. Kabashin, E. Sacher, M. Meunier, and J. H. T. Luong, "Stabilization and size control of gold nanoparticles during laser ablation in aqueous cyclodextrins," J. Am. Chem. Soc. **126**(23), 7176–7177 (2004).
48. A. Takami, H. Kurita, and S. Koda, "Laser-induced size reduction of noble metal particles," J. Phys. Chem. B **103**(8), 1226–1232 (1999).

1. Introduction

Fabrication of nanocrystals has gathered a lot of attention over the recent years due to the size dependent and hence tunable properties that can vary considerably from those of the bulk material. For semiconductor nanocrystals this allows adjustment of absorption and emission properties due to the change in the electron and the hole band-edge states and a blueshift of the band gap of the material when the particle size is smaller than the Bohr exciton radius of the material.

Gallium arsenide (GaAs), which is the base material for many optoelectronic devices, has a band gap of 1.42eV at 300K and the diameter of its Bohr exciton is about 19 nm [1]. This allows tuning of the band gap of the GaAs nanocrystals across the visible spectrum, which makes nanocrystalline GaAs an interesting material for various applications. Partly due to the high quantum efficiency achieved with compounds of zinc, cadmium, sulfur and selenide and especially with their core/shell-structures, free-standing GaAs nanocrystals have not been studied as thoroughly as the II/VI semiconductors. Properties of the GaAs nanocrystals and quantum dots have been investigated within oxide and polymer matrices and as epitaxially fabricated heterostructures. However, synthesis of stable, free-standing GaAs nanocrystals, exhibiting luminescence at clearly shorter wavelengths than bulk GaAs, has been challenging.

GaAs nanocrystals have been produced through chemical methods from $GaCl_3$ and $As(SiMe_3)_3$ in quinoline [2,3], from $GaCl_3$ and $(Na/K)_3As$ in toluene, monoglyme and diglyme [4], from $GaCl_3$ and $As(NMe_2)_3$ in 4-ethylpyridine [5] and from a single organometallic precursor in hexadecylamine [6]. The reports include observations of blueshifted band gap absorption [2–7] and visible photoluminescence [3–7]. These methods allow a good size control and produce a relatively narrow particle-size distribution, which is typical for chemical synthesis methods. However, these processes are fairly complex, requiring careful fabrication of precursors and require several process steps. The fabrication process can also take several days to finish.

Pulsed lasers have been used to fabricate nanocrystals by ablation of GaAs targets in low-pressure gas atmosphere. Thereafter, the nanocrystals were transferred to ethanol by nitrogen flow [8]. In these crystals, visible luminescence was observed at a low temperature of 2 K. A straightforward technique to fabricate nanocrystal solutions is pulsed laser ablation in liquids (PLAL). In this technique the GaAs target is suspended in a solvent and ablated with several laser pulses [9,10]. Lalayan reported visible luminescence from the samples fabricated using this technique, but the samples were not thoroughly characterized to confirm the source of the luminescence [9]. Ganeev *et. al.* reported gallium-rich (Ga:As-ratio 1.4:1) nanoparticles with increased extinction towards ultra-violet wavelength range, but no clear band-edge absorption was observed and photoluminescence was not studied [10].

Pure GaAs surface tends to oxidize, which can be detrimental for the properties of the nanocrystals. The thickness of the oxide can be comparable to the particle size and in some cases the particle can be completely oxidized. Another issue is the high ratio of surface atoms in nanocrystals, which introduces defects that change the electronic and optical properties of the particles. Particularly, in the case of photoluminescence, the (surface) defects can enhance

#165524 - $15.00 USD Received 26 Mar 2012; revised 20 Apr 2012; accepted 10 May 2012; published 14 May 2012

non-radiative transitions which reduce the photoluminescence. To reduce the harmful oxidation and to passivate the possible defects Traub *et. al.* demonstrated a process for oxide etching and subsequent surface passivation of solution suspended GaAs nanoparticles [11]. They reported improved luminescence intensity, especially after thermal annealing, but the produced nanoparticles were too large to exhibit change in the band gap due to quantum confinement.

In this paper, we report on a study of GaAs nanocrystals prepared with PLAL with simultaneous chemical surface passivation. The passivation is accomplished by using ammonium sulfide, a surface passivation agent widely studied for passivation of bulk GaAs [12], allowing a single-step fabrication of surface passivated nanocrystals. The nanocrystals exhibit visible photoluminescence and the prepared samples show no weakening of their luminescence during several months. We also elucidate the chemical structure of the prepared GaAs nanocrystals as a function of thermal annealing.

2. Experimental methods

2.1 Laser ablation

Laser ablation of solid GaAs targets was carried out in quartz and acrylic cuvettes using a high-repetition rate fiber laser ($\lambda \approx 1060$ nm, pulse width 20 ps, repetition rate 1 MHz, pulse energy ≈ 1.6 μJ, FWHM of the focused beam ≈ 15 μm). Targets were submerged in ethanol, de-ionized water or water solutions containing ammonium sulfide. The laser beam was moved on the target surface with a 2D mirror scanner with a speed of 2 m/s to avoid crater formation and possible heat induced problems associated with a high number of overlapping subsequent laser pulses [13].

2.2 Materials

The GaAs ablation target was an epitaxial grade, n-doped wafer manufactured by AXT. The dopant was silicon with atomic concentration of approximately $1.5 \cdot 10^{18}$ atoms cm^{-3}. De-ionized water with resistivity of 18 MΩ cm^{-1} was obtained from the Millipore Milli-Q-system. Ethanol (99.5%) was manufactured by Altia. Ammonium sulfide in a 20% water solution was obtained from Merck and it was used as received.

2.3 Sample preparation

The prepared nanoparticles were deposited on silicon substrates by drop casting. The substrate was placed on a hot-plate at a temperature of 170°C and drops of the nanoparticle solution were cast on the substrate until a total volume of 0.2 ml of the solution was consumed. Samples were then split in half; the first half was thermally annealed, while the second half was used as a reference.

Thermal annealing was performed in a nitrogen atmosphere. Annealing parameters were optimized to maximize the photoluminescence intensity of the samples while minimizing the changes to the shape of the luminescence spectra. A batch of 10 samples, prepared in ethanol, was used for the optimization procedure. Treatment at temperatures of 300°C and below caused no change in the photoluminescence of the samples when excited by laser pulses at 355 nm. The largest increase of the luminescence was observed at the temperature of 450°C, but the gain was accompanied by a considerable redshift in the wavelength of the maximum intensity. Parameters for the annealing experiment of the actual samples (375°C for 120 seconds) were selected as a compromise to maximize the PL with a minimal redshift.

2.4 Electron microscopy

To perform transmission electron microscopy (TEM) experiments, the nanoparticle samples dried on the silicon substrate were transferred to TEM-grids. This was achieved by first scratching the nanocrystals from the surface of the silicon substrate with a scalpel, then

#165524 - $15.00 USD Received 26 Mar 2012; revised 20 Apr 2012; accepted 10 May 2012; published 14 May 2012

placing the grid on top of the sample and finally dropping a single drop of ethanol to facilitate the transfer of the crystals to the grid. After drying, the grids were examined with a high-resolution TEM (Jeol JEM-2200FS). The same device was also used for electron diffraction measurements and for energy dispersive spectrometry (EDS). Additional inspection by scanning electron microscopy (SEM) was performed with a Carl Zeiss Ultra-55.

2.5 X-ray photoelectron spectroscopy (XPS)

The photoemission spectra were measured using a spectrometer (Perkin-Elmer PHI 5400) with a monochromatized Al Kα x-ray source that was operated at 14 kV. The analyzer pass energy was 18 eV and the energy step was 0.1 eV. In spectral analysis (fitting), the Voigt function was used after Shirley's background subtraction. The minimum number of components, as deduced from the pure line shape was included in fittings. For results reported here, no sample charging was observed as the As *2p* and Ga *2p* emission components from the GaAs nanocrystal were located systematically at 1324-1325 eV and 1117-1118 eV binding energies, respectively.

2.6 Raman spectroscopy

Raman spectroscopy was carried out with a spectrometer (Andor Shamrock 303) and a cooled CCD-camera (Newton 940P). The excitation laser was a 532nm wavelength Cobolt Samba with a beam FWHM of 0.7 mm. The sample was illuminated with a collimated laser beam in an approximately 30 degree angle with respect to the sample surface. In order to avoid sample heating the beam was not focused. Indeed, varying the laser power induced no peak-shifts, confirming that all observed deviations from the bulk Raman spectra are due to the properties of the sample. The scattered light was collected with a microscope objective along the normal of the surface of the sample and Rayleigh scattered light was filtered out with a Semrock Razoredge filter.

2.7 Photoluminescence measurements (PL)

Room temperature photoluminescence with excitation wavelengths of 355nm and 532nm was measured using the same Raman spectrometry setup. The 355nm excitation source was a diode-pumped solid-state laser (Ekspla NL202). The low-temperature measurements were done using a scanning monochromator (Oriel DK480) and a photomultiplier tube connected to a lock-in amplifier. The laser emitting at 532nm was used for excitation in the low-temperature measurements. The FWHM of the focused excitation beam in the photoluminescence measurements was approximately 100 μm.

2.8 Zetapotential measurements

The stability of the solutions was studied using a Malvern Zetasizer Nano instrument to measure the zeta-potential of the nanoparticle-solutions.

3. Results

3.1 Nanoparticles in liquids

Nanoparticle solutions produced by PLAL in ethanol were reddish-brown in color and stable for several months. On the contrary, the samples prepared in water were much lighter in color with visible clusters. Within 24 hours of preparation the samples in water were completely clear with clusters in the bottom of the container.

#165524 - $15.00 USD Received 26 Mar 2012; revised 20 Apr 2012; accepted 10 May 2012; published 14 May 2012

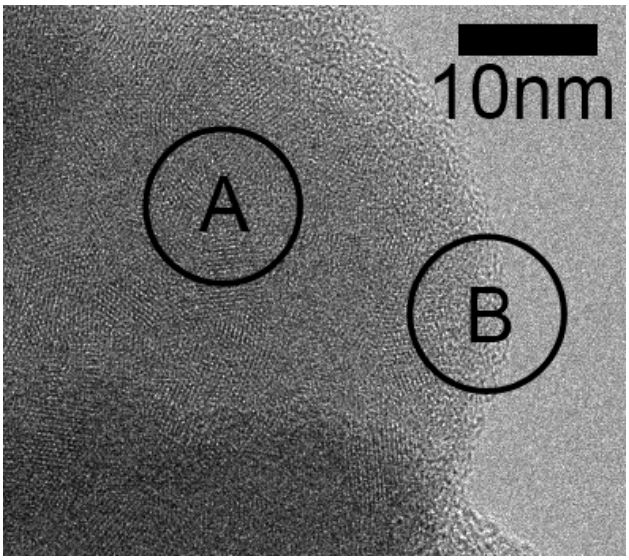

Fig. 1. HRTEM image of a large cluster of nanocrystals. The individual primary nanocrystals can be observed as separate crystalline regions within the cluster. The typical crystallite size is from 3 to 6nm. The EDS analysis was performed from regions A and B.

Table 1. EDS Analysis of the Nanoparticle Cluster Shown in Fig. 1

Element	A - core	B - edge
Ga	45%	32%
As	40%	18%
O	10%	40%
S	5%	10%

Laser ablation in a water solution of ammonium sulfide produced solutions with visual appearance and stability very similar to samples prepared in ethanol when the molarity of ammonium sulfide was between 0.1 mmol/l and 10 mmol/l. As the molarity of ammonium sulfide is increased above 10 mmol/l, increasingly lighter color solutions are produced. The color of the solutions keeps getting lighter during the following days until the liquid is completely clear. We interpret, that instead of stabilization, excess sulfur leads to formation of sulfide compounds that are subsequently oxidized. This interpretation is supported by the analysis of the samples prepared with ammonium sulfide molarity of 100 mmol/l. The Raman measurements show the distinct spectra of arsenolite (As_2O_3), which is the oxidation product of arsenic sulfide. The SEM-images also show micrometer-sized octahedra which are typical for arsenolite.

The Zeta-potential of the samples prepared in ethanol, 0.1 mmol/l and 1 mmol/l ammonium sulfide was measured to be –41 mV, –20 mV and –48 mV, respectively. Measurement of samples prepared in water was impossible due to rapid agglomeration.

3.2 Transmission electron microscopy

The TEM analysis shows that the samples consisted of crystalline nanoparticles and additional amorphous material.

The TEM samples were prepared from nanoparticles that were deposited on silicon substrates and therefore the primary nanocrystals have mostly agglomerated into larger clusters with sizes from 20 nm up to over one hundred nanometers. This prohibits proper statistical analysis of the size distribution of the primary nanocrystals. The diameter of the observed primary crystallites varied between 2 and 10 nm, the typical diameter being between 3 and 6 nm. The primary nanocrystals are polyhedron shaped, but on the average their shape

#165524 - $15.00 USD Received 26 Mar 2012; revised 20 Apr 2012; accepted 10 May 2012; published 14 May 2012

is close to a spherical form. Therefore, a relatively good estimation of the nanoparticle properties can be achieved by models developed for spherical nanoparticles. Few rod-like crystals were also observed.

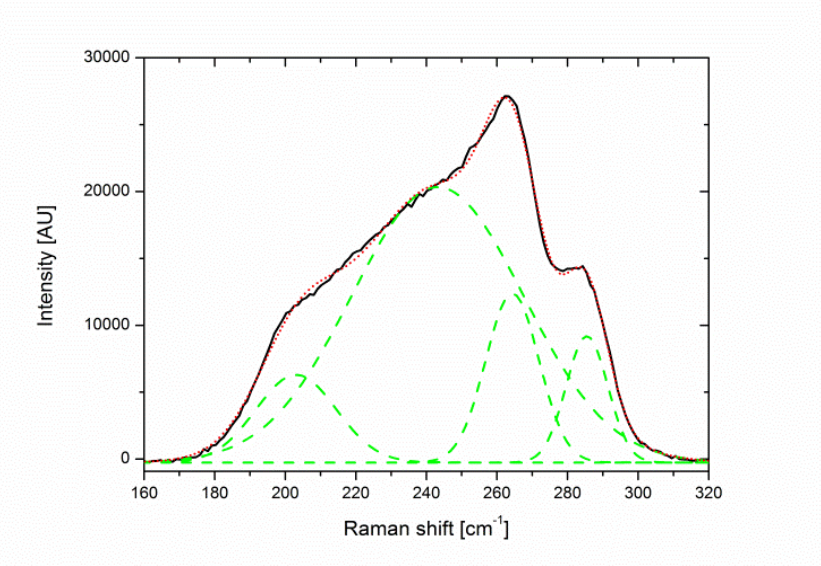

Fig. 2. Raman spectrum of GaAs nanocrystals prepared in ethanol. The fitted spectra is dominated by Gaussian peaks related to amorphous GaAs and amorphous arsenic. The black line is the measured spectrum, the red dotted line is the overall fit and the green dashed lines represent the individual components; from left to right: amorphous As, amorphous GaAs, and crystalline GaAs TO and LO phonon modes.

Electron diffraction and Fourier-transforms of the HRTEM images confirm that the crystals have zinc-blende structure with visible (111), (220), (311) and (422) diffraction peaks. The lattice constant was calculated to be 0.555 nm, which is lower than that of bulk GaAs (0.565 nm).

To analyze the influence of ammonium sulfide, we performed an EDS analysis on samples prepared in ethanol and 1mmol/l ammonium sulfide. Analysis was performed on agglomerates that included both nanocrystals and amorphous material. In ethanol the material is gallium rich, with 2 to 2.5 times more gallium than arsenic and with 30% to 35% oxygen. The RTA-treatment reduces the oxygen content to 25% and slightly increases the relative amount of arsenic, which is to be expected if amorphous material is removed and GaAs nanocrystals remain mostly unaffected by the treatment, as suggested by the Raman measurements. Samples prepared in ammonium sulfide have gallium to arsenic ratio between 1.2 and 1.6 with 33% oxygen and 2% sulfur. Again the RTA treatment improves the overall gallium to arsenic ratio and nearly halves the amount of oxygen and sulfur in the sample.

To further investigate the distribution of elements in the samples, we measured the EDS in the center (Fig. 1, region A) and on the edge (Fig. 1, region B) of a nanoparticle cluster for a sample prepared in 1 mmol/l of ammonium sulfide. The atomic percentages are listed in Table 1. The amorphous edge (region B) of the cluster is gallium rich with almost twice as much gallium as arsenic. The elemental composition suggests that the amorphous material attached to the nanocrystals is a mix of oxides and sulfides. The nanocrystals in the center (region A) are close to stoichiometric GaAs with gallium to arsenic ratio of 1.1 to 1. The amount of sulfur relative to oxygen is much higher than on the amorphous edge. Considering that the measurement of the center also includes some signal from the amorphous top layer, the results

#165524 - $15.00 USD Received 26 Mar 2012; revised 20 Apr 2012; accepted 10 May 2012; published 14 May 2012

suggest that the surface of stoichiometric GaAs nanoparticles is covered with a compound with Ga:O:S ratio close to 1:1:1.

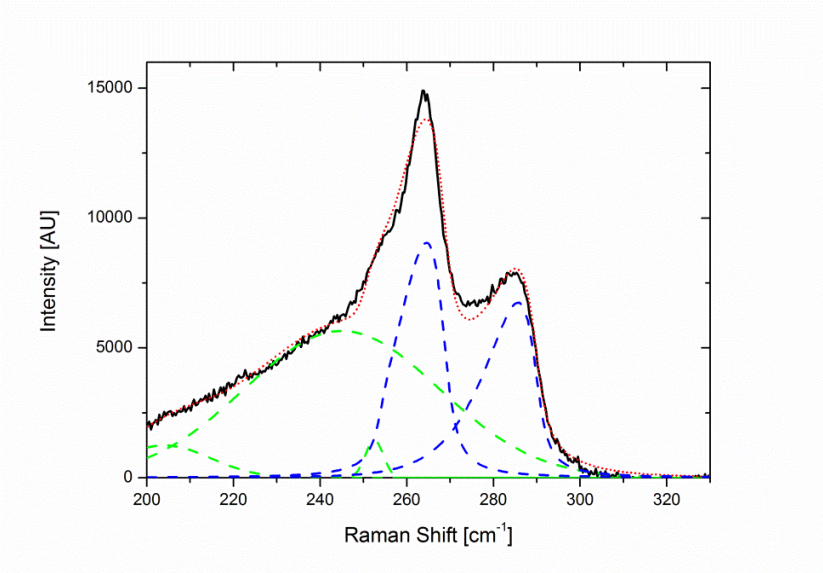

Fig. 3. Raman spectrum of a GaAs sample that was prepared in ethanol after thermal annealing. The black line is the measured spectrum; the dotted red line is the overall fit. The blue dashed lines are the TO and LO phonons of crystalline GaAs fitted with the Gaussian confinement model. The green lines represent the individual amorphous components: amorphous As (205 cm^{-1} and 252 cm^{-1}) and amorphous GaAs (245 cm^{-1}). The size of the nanocrystals obtained from the fit is 4.0 nm.

3.3 Raman spectroscopy

The peaks of both TO and LO phonons of GaAs can be observed in the Raman spectra of all of the samples. The peaks show considerable shifts towards lower energies and asymmetrical broadening, which is typical of GaAs nanocrystals [14].

For samples prepared in ethanol (Fig. 2) we observe Raman-peaks corresponding to the LO and TO phonons at wavenumbers of approximately 286 cm^{-1} and 265 cm^{-1} correspondingly. In addition, we see a large shoulder on the low-energy side. A reasonably good fit for this feature is achieved with two Gaussian peaks centered at 245 cm^{-1} and 205 cm^{-1}, which are attributed to amorphous GaAs [15,16] and amorphous arsenic [17–19] respectively. Also arsenic and gallium oxides have Raman features in this range, but other peaks related to these compounds are not observed. The amorphous components obscure the line shapes of the phonons related to crystalline GaAs. In the spectra of the annealed samples, the intensity of the amorphous components is significantly reduced (Fig. 3) revealing more precise shape of the crystalline phonon peaks. The LO phonon is observed at 286 cm^{-1} and the TO phonon at 265 cm^{-1}.

We used the Gaussian confinement model [20,21] to estimate the size of the nanoparticles from the Raman spectrum. For a full derivation of the model we refer to the original article by Richter et al. [20], a brief explanation can be found in the paper by Arora *et al.* [21]. The phonon dispersion curves were obtained from neutron scattering experiments performed at 12 K [22] and adjusted to room temperature using the temperature dependence measured by Chang *et al.* [23] The original model by Richter et al. [19] used $\alpha = 2$ to set the phonon amplitude at the nanoparticle boundary to $1/e$, however the best fits to the experimental data have often been obtained by setting $\alpha = 8\pi^2$ as proposed by Campbell and Fauchet [24].

#165524 - $15.00 USD Received 26 Mar 2012; revised 20 Apr 2012; accepted 10 May 2012; published 14 May 2012

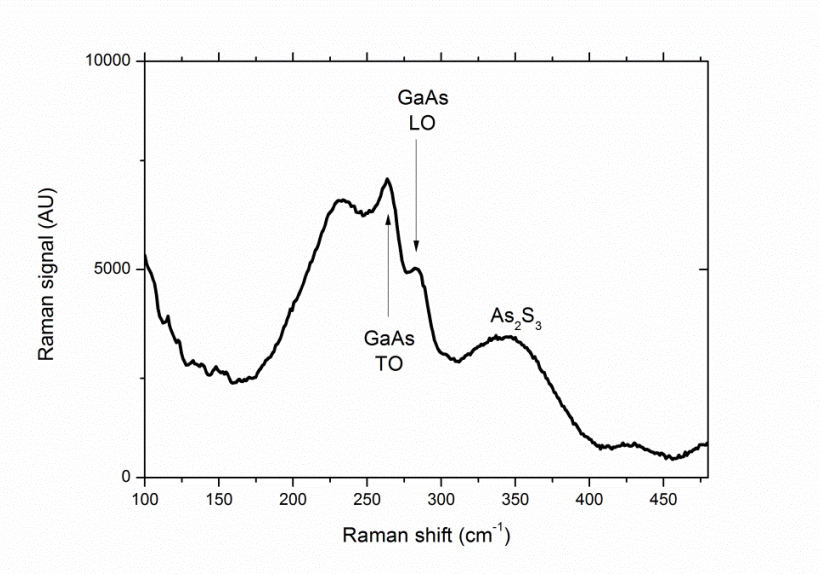

Fig. 4. Raman spectrum of the samples prepared in the ammonium sulfide solution. In addition to the peaks of crystalline GaAs, a Raman signal from arsenic sulfides is observed.

The best agreement with the experimental results, in very good agreement with the TEM measurements, was achieved for nanoparticle diameter of 4.0 nm, using $\alpha = 8\pi^2$ and including additional Gaussian peaks to model the contribution of amorphous GaAs and amorphous arsenic (Fig. 3). The broad peak centered at 247 cm^{-1} is attributed to amorphous GaAs and the peaks at 252 cm^{-1} and 204cm^{-1} to amorphous As. Calculations with $\alpha = 2$ and $\alpha = 9.67$, from the bond-polarizability model [25], produced relatively poor fits.

The calculated spectrum agrees with the measurements surprisingly well considering that the size distribution of our samples is relatively wide. The nanoparticle diameter has a significant impact on the shape of the calculated spectrum in the size range observed in the TEM measurements. The broad size distribution was expected to produce considerably broadened Raman peaks and a greater mismatch between the fit and the experimental data. However, the results are very similar to the ones calculated for monodisperse nanocrystals [13]. This can be partly explained by enhancement of the Raman signal by resonant excitation. Using a laser with a wavelength which is resonant with a transition in the studied material can increase the Raman signal by several orders of magnitude. In the particular case of 532 nm excitation wavelength, the signal from nanocrystals with transitions near the energy of 2.33 eV is enhanced. Nanocrystal size with corresponding band gap energy falls within the size range observed with TEM as discussed later and thus resonance enhancement could explain the observed strong Raman peaks.

For the samples prepared in the solutions of ammonium sulfide, the peak of the crystalline GaAs LO phonon is observed at 285 cm^{-1} and the peak of the TO phonon at 264 cm^{-1} (Fig. 4). Two additional broad features are observed around 230 cm^{-1} and 345 cm^{-1}. The broad peak around 230 cm^{-1} is in part attributed to amorphous gallium arsenide and arsenic that are also observed for the samples prepared in ethanol. The shape and the location of the peak is, however, slightly different suggesting formation of gallium and arsenic sulfides. The feature around 345 cm^{-1} is attributed to arsenic sulfide As_2S_3 (orpiment) [26], which is most likely in the amorphous form. This is suggested by the broadness of the peak and the absence of crystalline sulfides in the TEM analysis. Gallium sulfide, GaS, has Raman peaks near 345 cm^{-1} as well [27], but gallium sulfide has a high melting point of 965 °C and the feature

#165524 - $15.00 USD Received 26 Mar 2012; revised 20 Apr 2012; accepted 10 May 2012; published 14 May 2012

almost completely vanishes during RTA at 375 °C. Therefore the observed feature is most likely due to arsenic sulfide which has considerably lower melting point near 300 °C.

The RTA treatment decreases the signal from the sulfides and amorphous components, but at the same time increases the photoluminescence making detailed analysis of the peaks corresponding to GaAs difficult.

3.4 XPS

The core-level photoemission spectra in Figs. 5 and 6 show many As- and Ga-oxide related components in addition to the GaAs components. Due to the nature of the XPS measurements the signal arises mostly from the oxidized surface parts of the nanocrystal agglomerates (Fig. 1, region B) and from the amorphous material between the agglomerates. The As_2S_3 component is also observed, and its intensity clearly decreases during the RTA, being in good agreement with the above Raman results. Furthermore, it is observed that the relative intensity of the GaAs emission decreases. The accuracy of the analysis does not allow separation of emission from GaAs and amorphous As, and thus this apparent decrease of GaAs photoemission is in line with the disappearance of the amorphous GaAs- and amorphous As-components in the Raman spectra.

Before the RTA the samples prepared with the mild sulfur content appear to include also metallic Ga. Furthermore, the As XPS spectra reveal that the increased sulfur amount in the preparation decreases the formation of the highest oxidation state, As_2O_5, and enhances the As_2O_3 formation during the RTA. The increased sulfur concentration also decreases the amount of oxidized Ga. The signal corresponding to GaAs and amorphous As in the As *2p* spectrum is exceptionally strong in the sample prepared in 5 mmol/l $(NH_4)_2S$ which is reduced during the RTA suggesting that the sample has a considerable amount of amorphous material.

It is worth noticing that the possible emission from the lowest Ga oxidation state, Ga_2O, overlaps with the GaAs emission. These XPS results are discussed later along with the PL results.

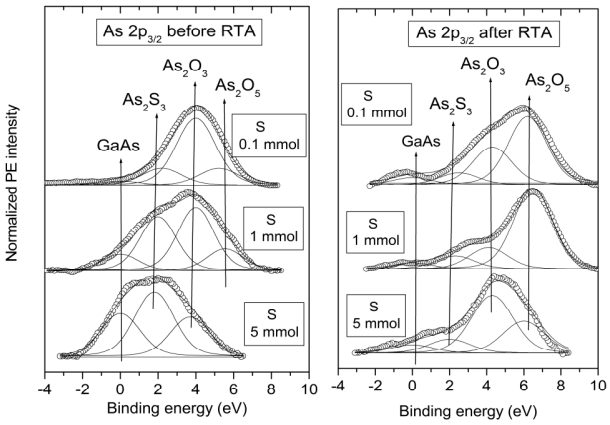

Fig. 5. As *2p* photoemissions from the nanocrystal samples prepared with ammonium sulfide. The origins of different photoemission components are proposed.

#165524 - $15.00 USD Received 26 Mar 2012; revised 20 Apr 2012; accepted 10 May 2012; published 14 May 2012

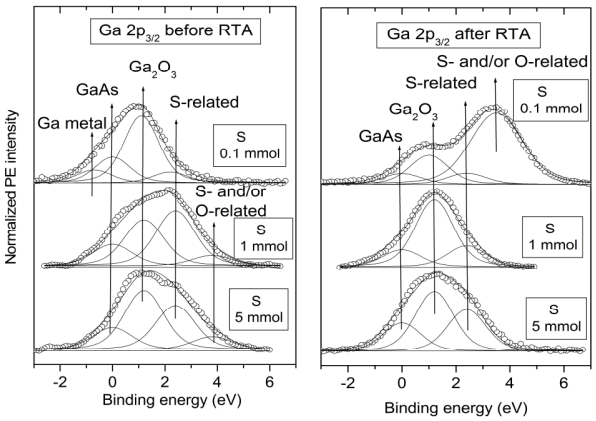

Fig. 6. Ga *2p* photoemissions from the nanocrystal samples prepared with ammonium sulfide. The origins of different photoemission components are proposed.

3.5 Photoluminescence

After drop casting on silicon substrate, the samples prepared in ethanol show weak photoluminescence when excited with a wavelength of 355 nm (Fig. 7A). The spectrum is very broad and seems to have two underlying peaks centered at 530 nm and 650 nm. The RTA treatment with optimized parameters increases the intensity of the luminescence approximately by an order of magnitude (Fig. 7B). For this sample the enhancement is stronger near the peak at 530 nm creating an apparent blueshift for the total spectrum.

The samples prepared in pure water did not show luminescence in our measurements. However, addition of small amounts of ammonium sulfide produced samples with more intense photoluminescence than the samples prepared in ethanol. With 0.1 mmol/l molarity, the spectrum has the two features also observed in the case of ethanol; the biggest difference being that the shorter wavelength peak is dominant even before the RTA and the center is at a slightly shorter wavelength of 520 nm (Fig. 7A). Increasing the molarity further enhances the luminescence intensity and especially the peak at 520 nm until at molarities of 5 mmol/l and above the peak starts to slowly redshift and the maximum intensity starts to fall. With 1 mmol/l molarity of ammonium sulfide the intensity of the luminescence is roughly an order of magnitude stronger than for nanocrystals prepared in pure ethanol. Interestingly, a further gain of an order of magnitude is observed after the RTA treatment (Fig. 7B). The RTA treatment also induces a redshift, of the peak wavelength to approximately 550 nm. The luminescence of the RTA-treated samples is also visible to the naked eye.

The significant improvement of the photoluminescence intensity from the crystals prepared with $(NH_4)_2S$ and after the RTA treatment made the luminescence measurable with excitation at 532 nm. This enabled us to measure the temperature dependence of the luminescence from 30K to 290K (Fig. 8). As expected, the intensity of the photoluminescence increases for all of the samples as the temperature is lowered. The temperature dependence of the integrated intensity, I_{PL}, was fitted with a simple model to estimate the activation energy, E_A, of the thermally activated non-radiative processes related to quenching of the luminescence at higher temperatures. The intensity can be written as:

$$I_{PL}(T) = \frac{I_0}{1 + \sum_{i=1}^{n} C_i \exp\left(-E_{A,i} / k_B T\right)}, \quad (1)$$

#165524 - $15.00 USD Received 26 Mar 2012; revised 20 Apr 2012; accepted 10 May 2012; published 14 May 2012

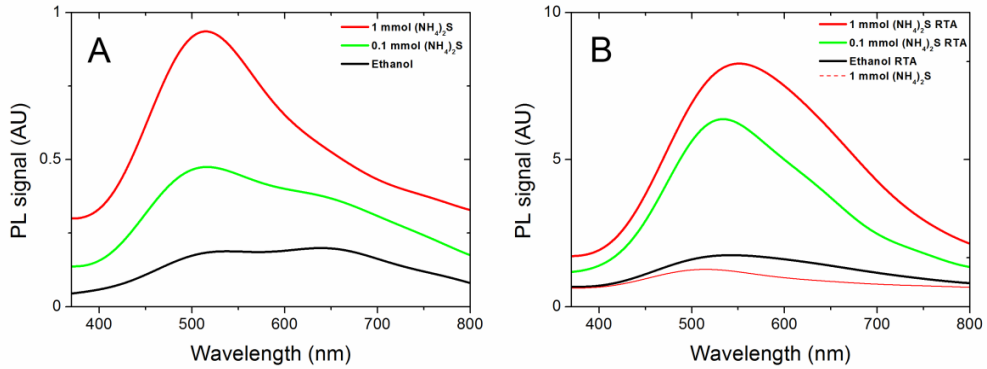

Fig. 7. Photoluminescence of the samples under 355 nm excitation. (A) As-deposited samples. (B) Samples after thermal annealing for 120 s at 375 °C. Luminescence spectrum of the unannealed sample prepared in the 1mmol/l $(NH_4)_2S$ solution is included as a reference.

where k_B is the Boltzmann constant, I_0 the intensity at 30 K and C_i is a weighting factor. Achieving a good fit required the use of one or two terms for the non-radiative processes depending on the sample.

For the RTA-treated samples prepared in ethanol the intensity is enhanced by a factor of 2 at low temperatures. The data and the fitted curve are plotted in Fig. 8A. A good agreement is achieved using two competing non-radiative decay mechanisms with activation energies of 2.5 meV and 50 meV. Unannealed samples did not have a strong enough PL signal to allow the measurement.

The measured temperature behavior and the fitted curves for samples prepared in 1mmol/l ammonium sulfide solution before and after annealing are plotted in Fig. 8C. Before annealing, the best fit is achieved using two terms with activation energies of 25 meV and 100 meV. The annealing seems to remove the low-energy decay route and a good fit for the RTA-treated sample is achieved using only one term yielding activation energy of 100 meV.

For samples prepared in 0.1 mmol/l of ammonium sulfide solution after the RTA-treatment, a good fit is achieved with two energies of 32 meV and 96 meV (Fig. 8B). This suggests that only partial passivation has been achieved, which agrees well with the lower overall intensity when compared with the samples prepared in molarity of 1 mmol/l. The unannealed sample behaves in a slightly more complex way showing a step-like behavior. A moderate fit is achieved with activation energies of 26 meV and 100 meV. However, a far better fit is achieved when using a sum of two independent emission terms, both following Eq. (1) with activation energies of 97 meV and 106 meV. This suggests that the emission might actually derive from two different sources with different band-edge electron and hole states which could be related to different size nanoparticles or due to the incomplete surface passivation creating two different populations of differently behaving nanoparticles.

The behavior of the samples prepared in 5 mmol/l solution of ammonium sulfide is more complex before annealing (Fig. 8D). The integrated luminescence intensity starts to oscillate as a function of temperature at temperatures below 150 K. Due to these oscillations, the relevance of the fitting parameters of Eq. (1) becomes highly questionable. We cannot explain this behavior, but it is likely that the mechanism for luminescence quenching is more complicated for higher sulfur concentrations. After the RTA treatment a good fit is achieved also for this sample with activation energies of 5 meV and 81 meV.

4. Discussion

Laser ablation of the target induces formation of plasma. The expansion of the plasma is restricted by the surrounding liquid which causes nucleation of the evaporated material to form nanoparticles [28]. In inert liquids this tends to lead to electrically charged nanoparticles

#165524 - $15.00 USD Received 26 Mar 2012; revised 20 Apr 2012; accepted 10 May 2012; published 14 May 2012

repel each other and therefore form very stable solutions. In the case of GaAs in water and solutions of ammonium sulfide the liquid is clearly not inert and oxygen and sulfur can react with the formed GaAs nanoparticles leading to the observed thin oxide and sulfide shells. The reactive species in the solvent can also react directly with gallium and arsenic ions at the liquid-plasma boundary, which can lead to direct formation of gallium and arsenic oxides and sulfides. We suspect that this is the origin of the amorphous material observed in the TEM and Raman analysis.

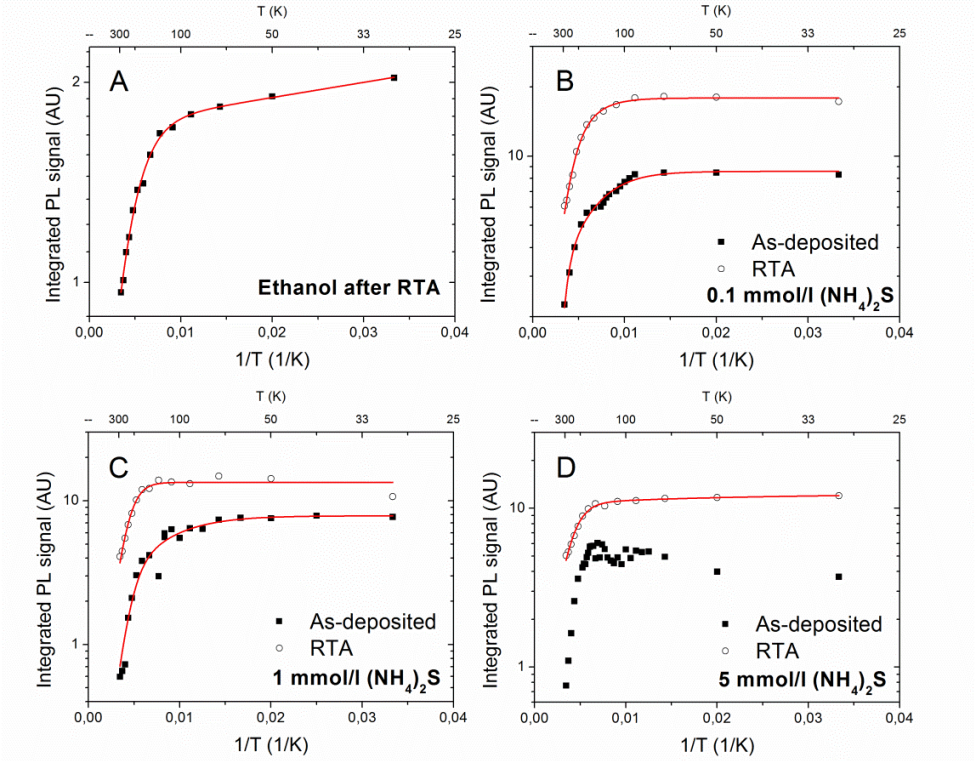

Fig. 8. Temperature dependent photoluminescence measurements excited with laser at wavelength of 532 nm. The samples produced in ethanol did not produce measurable luminescence before the RTA treatment. The values on the y-axis are included as a scale reference and are not directly comparable between different graphs.

The highest stability of the nanoparticle colloids is achieved in the intermediate molarity range between 0.1 mmol/l and 10 mmol/l of ammonium sulfide in water. The TEM and EDS analyses show that the most stable particles have a GaAs core and the surface is a gallium rich compound with both sulfur and oxygen. Therefore the stability is achieved by a combination of oxygen and sulfur and not by sulfur passivation alone. Particles produced in ethanol are stable and have a thin surface oxide layer, but it is unclear whether this oxide is produced in the liquid or after deposition in ambient air. High molarity of ammonium sulfide solution leads to destabilization and change in particle composition over time. All of these results support the proposed model for the PLAL in which the newly formed, very hot nanoparticles are reactive, but after cooling down the particles are stable unless the liquid is chemically reactive.

It is noteworthy that the most stable particles also exhibit the highest luminescence intensity. This supports the hypothesis that the stabilization is related to successful surface passivation. The samples were very stable after deposition on silicon and the measured Raman

#165524 - $15.00 USD Received 26 Mar 2012; revised 20 Apr 2012; accepted 10 May 2012; published 14 May 2012

and photoluminescence spectra were unchanged for at least six months. This is unexpected, considering that sulfur passivation of GaAs wafers has been shown to deteriorate within days [29,30]. The origin of the high stability in our samples might arise from the fact that the deposited nanocrystals have formed clusters where the passivated surfaces are actually interfaces between nanocrystals and therefore protected. It is also possible that the passivation layer, being a compound with both sulfur and oxygen, is more stable in the case of nanoparticles than sulfur alone.

Due to the properties of the samples, statistical size distribution measurements were not possible. However, the different estimates for the average nanocrystal size agree relatively well. Based on the TEM analysis, the typical nanocrystals are between 3 and 6 nm in diameter and the diameter obtained from the fitted Raman spectra is 4 nm. The photoluminescence maximum is near to the photon energy of 2.34 eV. Using the commonly applied effective mass approximation [1] a corresponding particle diameter of 2.3 nm can be calculated, however it is well known that this approximation does not work well for very small nanocrystals and yields too small size estimates. Calculations by Diaz *et al.* [31] based on an empirical $sp^3d^5s^*$ nearest neighbor tight-binding model developed by Jancu *et al.* [32] gives an estimated nanocrystal diameter of 3.4 nm which is in better agreement with the other size approximations. This is also in excellent agreement with the speculated resonance enhancement during Raman measurements.

A speculative comparison might be done between the observed lattice constant and previous findings on pressure-dependent behavior of the band gap: the change in the GaAs bulk lattice constant of 0.565 nm to 0.555 nm would require 4 GPa hydrostatic pressure [33] that would cause the band gap energy to increase by approximately 0.4 eV [34]. The tight-binding model in [32] did not explicitly allow lattice relaxations and used bulk values instead, therefore the additional blueshift caused by the decreased lattice constant should be considered as an additional effect. Therefore the HRTEM observation of a smaller lattice constant would imply that the nanocrystals have larger band gap than would be implied by their size related quantum confinement alone. On the other hand, the change of the lattice constant to smaller values could also be expected to shift the Raman peaks towards higher wave numbers as observed for epitaxial GaAs films in diamond anvil experiments [35]. However, this is not observed in our nanoparticles.

As a future work it would be interesting to carry out band gap and lattice constant measurements of nanoparticles with a very narrow size distribution in order to clarify the possible abovementioned issue related to the relationship between the lattice constant and PL wavelength in small nanocrystals and whether it should be taken into account in modeling.

The RTA treatment was observed to yield a significant increase in the PL intensity. This is attributed to several factors. Firstly, during the formation process, the nanoparticles are cooled down by the solvent from very high temperatures (thousands of K) in the plasma to room temperature very rapidly, which can leave plenty of crystal defects that are removed with annealing. Secondly, the passivating sulfur and oxygen layer can reorganize and improve the passivation. Thirdly, the amount of defects at the oxidized surface of the agglomerate, causing absorption, decreases during the RTA. It has been previously found related to PL of bulk GaAs that (i) Ga_2O_3 phase causes PL weakening defects, (ii) Ga_2O might even improve the oxidized GaAs surface, and (iii) As oxides are not harmful [36–38]. Our results are consistent with this picture. And finally, the amorphous material which possibly absorbs the emitted light is evaporated as shown by our Raman and XPS measurements.

The broad luminescence spectrum suggests that the nanocrystals have a relatively broad size distribution. The spectra for samples prepared in ethanol or in low ammonium sulfide molarities have two pronounced features, one centered at approximately 530 nm and another at 650 nm. This suggests that the size distribution is roughly bimodal with two separate and broad size distributions, which is typical to PLAL samples. The RTA treatment seems to enhance the luminescence from the smaller particles more efficiently. This is also the case

#165524 - $15.00 USD Received 26 Mar 2012; revised 20 Apr 2012; accepted 10 May 2012; published 14 May 2012

when molarity of ammonium sulfide is increased, suggesting that the number of nanoparticles in the lower size-distribution mode is greater, but the smaller particles are also affected by defects more severely.

Roughly similar photoluminescence has been measured for porous GaAs [39,40]. This has also been attributed to quantum confinement in nanocrystals, although the evidence of existence of the nanocrystals in those cases has been ambiguous.

The wide application range of the nanocrystals include fluorescence labels in biodiagnostics [41], luminescent media to convert and broaden the emission of blue LEDs to solid state white light source [42] and optical limiting by utilization of nonlinear optical properties of the particles [43]. Our results could pave way for the GaAs nanocrystals as an alternative technology for generating various colors by pumping them with blue LEDs. On the other hand, solid state InGaN quantum wells have been intensively investigated and developed for the blue/green/yellow emitters for obtaining white light directly, and indeed great progress in this field has been made [42,44–46]. An interesting future direction towards electrically pumped light source could rely on our nanoparticles uniformly layered on silicon substrates. At present, the properties of the crystals cannot compete with the properties of solid InGaN/GaN technology.

One factor that can limit the applications of the nanocrystals demonstrated in this work is the broad size distribution. The distribution can be narrowed by careful optimization of the process parameters, by modifying the liquids by additional chemicals, e.g. cyclodextrins [47] prior to ablation and by further laser processing [48]. For size critical applications, further size-selective filtering and deposition techniques can be applied. Further work must also be done to improve the quantum efficiency of the nanocrystals. This could be done by further optimization of the surface passivation or by deposition of a suitable shell-layer to form core/shell-particles.

5. Conclusions

The combined information from the TEM, EDS, Raman and XPS analysis shows that we have successfully produced surface passivated GaAs-nanocrystals that form stable colloidal solutions. The as-prepared nanoparticle solutions are not luminescent. Nanocrystals deposited on silicon wafers show photoluminescence with a broad spectrum on visible wavelengths peaked near 530 nm. The luminescence shows no deterioration within six months. It is also evident that a considerable portion of the evaporated material reacts with the solvent and forms amorphous material. The PL intensity is considerably enhanced by the sulfur and oxygen containing surface passivation and by thermal annealing via the removal of non-radiative defects and possibly light-absorbing amorphous material.

Acknowledgments

The authors acknowledge Joel Salmi for performing the RTA-treatments, Antti Tukiainen and Janne Simonen for discussions that improved the quality of this research, Hua Jiang for the TEM measurements and Tapio Sorvajärvi and Juha Toivonen for the possibility to use the 355nm laser. We also acknowledge Jenni Leppiniemi and Vesa Hytönen for their help with the zeta-potential measurements.

This work was funded by European Regional Development Fund through Council of Pirkanmaa in project EA31189.

#165524 - $15.00 USD Received 26 Mar 2012; revised 20 Apr 2012; accepted 10 May 2012; published 14 May 2012

Publication 4

P4

T. Salminen, M. Honkanen, T. Niemi, ''Coating of gold nanoparticles made by pulsed laser ablation in liquids with silica shells by simultaneous chemical synthesis'', *Physical Chemistry Chemical Physics*, Vol. 15, pp. 3047-3051, 2013

PCCP

RSC Publishing

PAPER

Coating of gold nanoparticles made by pulsed laser ablation in liquids with silica shells by simultaneous chemical synthesis

Cite this: *Phys. Chem. Chem. Phys.*, 2013, **15**, 3047

Turkka Salminen,*[a] Mari Honkanen[b] and Tapio Niemi[a]

Received 20th July 2012,
Accepted 24th September 2012

DOI: 10.1039/c2cp42999c

www.rsc.org/pccp

Coating of gold nanoparticles with silica shells by the well known Stöber-method requires the use of additional coupling agents to seed the growth of the shell as gold does not form a native oxide. Here we report a novel single-step process to create the gold nanoparticles directly into a mixture of tetraethyl orthosilicate and a catalyst by means of pulsed laser ablation in liquids. We observe that good silica shells are achieved only when all of the reagents are present during the production of the nanoparticles. Experiments with two different laser wavelengths: 515 nm and 1030 nm, show that the formation of the shell is efficient only with the laser wavelength close to the plasmon resonance of the gold nanoparticles. We propose a model indicating that the shell formation is initiated by laser-induced heating of the particles.

I. Introduction

Metal nanoparticles have many applications that require coating of the particles with shells or conjugated ligands. Silica shells are often used to increase biocompatibility and to serve as a platform for further functionalization. In the case of nanoparticles exhibiting local plasmon resonances, such as silver and gold, thin coating can be used to separate molecules from the surface of the particle. This allows enhancement of various optical interactions without quenching processes that dominate if the molecule is in direct contact with a metal nanoparticle.

Most approaches to produce colloidal silica-coated nanoparticles have adapted the Stöber-method[1] to grow the shell through hydrolysis of tetraethyl orthosilicate (TEOS). Gold, however, is extremely stable and inert material, which does not form a native oxide layer, which would act as a seed for silica growth. Therefore, the methods for gold–silica-core–shell nanoparticle fabrication are usually two-step processes that first require the use of coupling agents or primers that create a thin initial shell. Subsequently, nanoparticles are transferred to *e.g.* ethanol or 2-propanol and a thicker shell is grown through the Stöber-method. This approach was first demonstrated by Liz-Marzán *et al.*[2] who used silane molecules with an amino group as a surface primer. Alternatively, a thiol group or a combination of both types of molecules can be used.[3] Mine *et al.* showed that citrate stabilized gold nanoparticles can be coated without separate primers in a process where TEOS apparently reacts with the citrate to initiate the silica shell formation.[4] Fernández-López and co-workers used thiol-modified PEG for gold nanoparticle stabilization, which allowed silica growth with TEOS after the particles were transferred to ethanol.[5]

Barcikowski *et al.* reported coating of gold nanoparticles made by pulsed laser ablation in liquids (PLAL) with silica shells using a mixture of PVP and TEOS or amine-functionalized ATEOS[6] following the synthesis route suggested by Graf *et al.*[7] However, their conclusion was based on the increase of the hydrodynamic size of the particles and they did not observe the red-shift of the plasmon peak in the extinction spectra, which is normally associated with the formation of the silica shell.

We report a process that allows growth of silica shells directly onto pure gold nanoparticles without additional coupling or passivation agents. Furthermore, the nanoparticles can be fabricated directly into *e.g.* ethanol–water-mixture- or 2-propanol-based solution with TEOS and the chosen catalyst, eliminating the need to transfer the produced particles into a suitable solvent before the coating step. We propose that the mechanism for the direct shell formation is based on heating of the produced gold nanoparticles with the laser illumination near the plasmon resonance wavelength. Direct reaction of the nanoparticles with TEOS can lead to gold–silicon bonds on the nanoparticle surfaces and the silicon can then serve as a seed for the growth

[a] *Optoelectronics Research Centre, Tampere University of Technology, P.O. Box 692, 33101 Tampere, Finland. E-mail: turkka.salminen@tut.fi; Fax: +358 3 364 1436; Tel: +358 40 198 1070*

[b] *Department of Materials Science, Tampere University of Technology, Finland*

of a silica shell. By varying the TEOS concentration the method can be used to make core–shell structures or silica spheres with embedded individual or agglomerated gold nanoparticles.

II. Experimental

Methods and materials

Experiments were carried out in a glass container with the gold target placed in the bottom. Laser ablation was performed with Eolite Boreas laser with a pulse duration of 10 ns. The repetition rate used in the experiments was 20 kHz. The influence of the wavelength was studied by using two different wavelengths: the fundamental wavelength of 1030 nm and its frequency doubled wavelength of 515 nm. The beam was scanned using a 2D scanner to avoid crater formation. The pulse energy was 75 μJ, the spot diameter was approximately 30 μm and the laser fluence was approximately 10 J cm^{-2}.

Tetraethyl orthosilicate (99.999%) was purchased from Sigma–Aldrich and diluted with 2-propanol. Ammonia (a 28% water solution) and 2-propanol (99.5%) were manufactured by J. T. Baker. The gold-target was purchased from Kultakeskus.

The morphology of the produced nanoparticles was analyzed using a scanning electron microscope (SEM, Carl Zeiss Ultra-55) and a transmission electron microscope (TEM, Jeol JEM-2010) equipped with an energy dispersive X-ray spectrometer (EDS, Noran Vantage with a Si(Li) detector, Thermo Scientific). TEM samples were prepared by placing and drying a droplet of the nanoparticle solution on a holey carbon film on a copper grid. Several hundreds of nanoparticles were imaged from each sample and images representing typical structures are presented here. Extinction spectra of the colloids were measured using an Ocean optics HR-4000+ spectrometer and an Ocean optics DT-Mini-2-GS light source. The extinction is calculated from the transmission spectrum measured through the samples as $-\log_{10}(I/I_0)$ and it includes both the absorption and the scattering from the particles and the agglomerates.

Sample preparation

It has been previously shown that very good results are obtained for PLAL fabrication of bioconjugated nanoparticles when the biomolecules are already present in the ablation liquid.[8] In production of composites of polymers and embedded nanoparticles, the presence of the monomers during the PLAL process was observed to be a crucial factor to avoid nanoparticle aggregation during polymerization.[9]

To study the effect of having TEOS and/or a catalyst present during PLAL, we used several different approaches. First we tested the Stöber-process with nanoparticle colloids prepared in advance. The second approach was to include either TEOS or the catalyst during PLAL while the other reagent was added afterwards. Finally, ready-made Stöber-solutions with both TEOS and the catalyst were present in the solvent during PLAL (Fig. 1).

The experiments were carried out using 2-propanol as the solvent. The concentration of TEOS was varied from 5 μM to 45 mM. As the catalyst, we used ammonia with concentrations from 7 mM to 0.7 M. The gold nanoparticles produced with PLAL are stable in 2-propanol without any additional stabilizers and therefore the only added reagents were TEOS and ammonia.

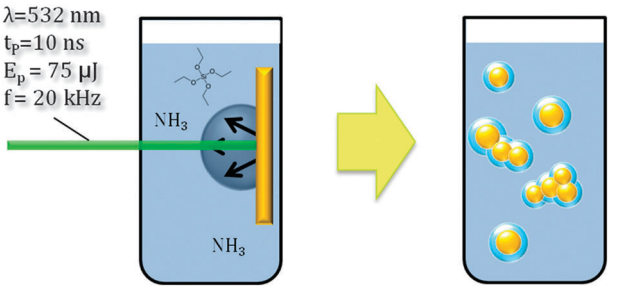

Fig. 1 Experiment: best results are achieved when the ablation is performed in the presence of both TEOS and a catalyst.

III. Results and discussion

Stöber-process for nanoparticle colloids

First a set of nanoparticle colloids were prepared in a pure solvent by ablation of the gold target with laser pulses at 515 nm wavelength. Then TEOS and the catalyst were added into the colloid. In all of the tests, addition of the catalyst caused rapid agglomeration and subsequent sedimentation of the nanoparticles regardless of the addition order of TEOS and ammonia. Thus, this approach did not lead to the desired silica coated gold particle colloids.

PLAL with TEOS in the solvent

Similar results were obtained for samples prepared with TEOS in the solvent during the PLAL process. The addition of the catalyst resulted in rapid agglomeration of the nanoparticles. However, high concentration (>5 mM) of TEOS resulted in such a rapid formation of large silica spheres, with diameters ranging from 100 nm up to 1 μm that the gold nanoparticles were captured on the surface or inside the spheres.

PLAL with the catalyst in the solvent

Somewhat surprisingly, adding the catalyst into the solvent before the laser ablation led to production of stable gold nanoparticle colloids. After the ablation, TEOS was added in varying concentrations and some silica growth was observed after 20 hours as shown in Fig. 2(A) for the TEOS concentration of 0.5 mM. However, the shells are incomplete with irregular shapes. In addition, only coated agglomerates and no single core–shell particles were observed in TEM analysis. The extinction spectra of the samples show a gradual red shift of the plasmon resonance peak by 4 nm during the 20 hours (Fig. 3).

PLAL with TEOS and the catalyst in the solvent

The most successful approach was to add both, TEOS and the catalyst, into the solvent just before starting the ablation. TEM images of the samples immediately after the PLAL process show a very thin amorphous layer on the surface of the gold nanoparticles. In the samples deposited on TEM grids 20 hours

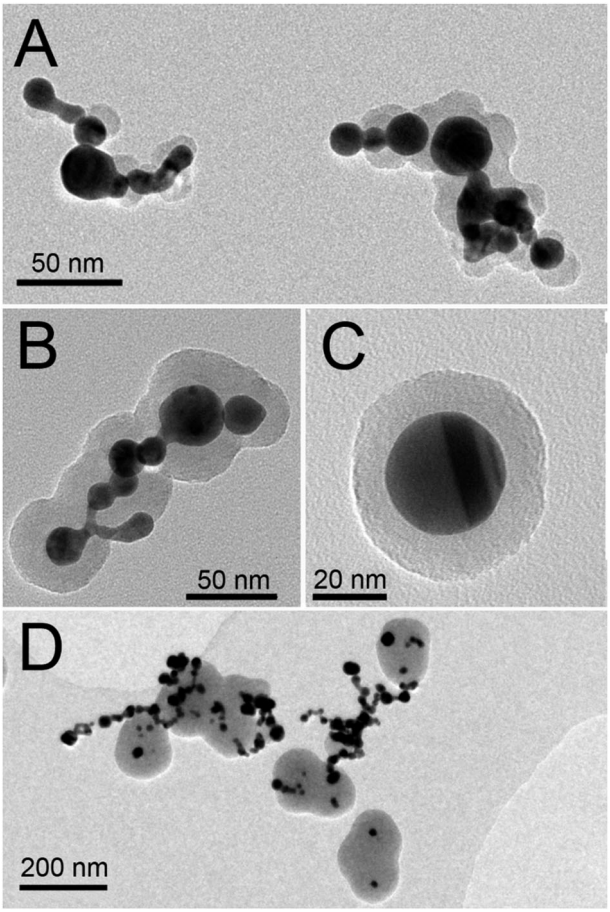

Fig. 2 TEM images of the samples produced in 2-propanol. The silica has been produced with 0.5 mM TEOS and 0.7 M ammonia. PLAL with the catalyst in the solvent and addition of TEOS afterwards leads to stable colloids, but the shells are rough and incomplete (A). PLAL with both reagents in the solvent leads to growth of a thin shell on both: individual nanoparticles and nanoparticle agglomerates (B and C). However, the growth was successful only with the laser wavelength of 515 nm. PLAL with 1030 nm wavelength produced only partial shells (D).

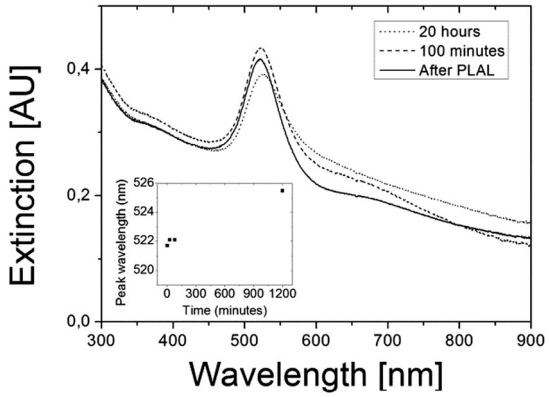

Fig. 3 Extinction spectra for the sample shown in Fig. 2(A) measured at varying times after the PLAL process and TEOS addition. The sample was prepared in 2-propanol with 0.7 M ammonia. Afterwards TEOS was added its final concentration being 0.5 mM. Inset: the plasmon peak shifts by 4 nm during 20 hours.

after the preparation, almost all of the individual particles and agglomerates are covered with a silica shell as shown in Fig. 2(B) and (C). Extinction measurements show that the plasmon resonance peak red shifts after the sample preparation up to a total of 5 nm measured after 20 hours (Fig. 4). These samples were prepared in 2-propanol, with a TEOS concentration of 0.5 mM and an ammonia concentration of 0.7 M.

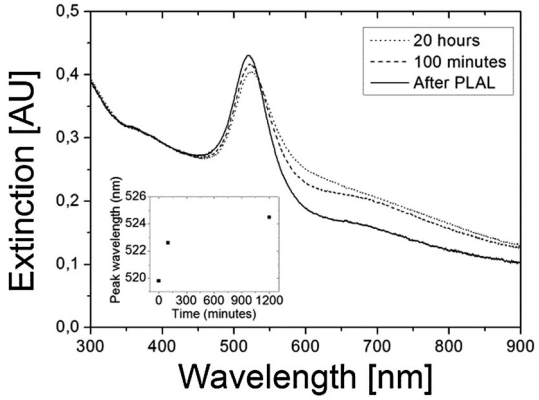

Fig. 4 Development of the extinction spectrum in time for a typical sample produced by PLAL in 2-propanol with 0.5 mM TEOS and 0.7 M ammonia. TEM images of the sample are shown in Fig. 2(B) and (C). Inset: the observed wavelength of the plasmon peak shows a red-shift as the shell gets thicker. The plasmon peak after 20 hours in this case is narrower than for samples characterized by the spectra in Fig. 3.

Samples produced with TEOS concentrations below 0.25 mM were not observed to have shells in TEM analysis. In this case, the extinction measurements show that the plasmon resonance peak red shifts by only approximately 1 nm as shown in Fig. 5.

The use of TEOS concentrations higher than 5 mM led to production of large (>100 nm) silica spheres with embedded gold nanoparticles and agglomerates. Our results show that the extinction measurements alone are not enough to allow conclusions regarding the shell growth. Distinguishing good quality shells from partial and rough shells requires additional analysis, *e.g.* TEM. However, our data show that for samples with too low TEOS concentration for the shell growth to be observable in TEM, the red shift is also minimal (Fig. 5).

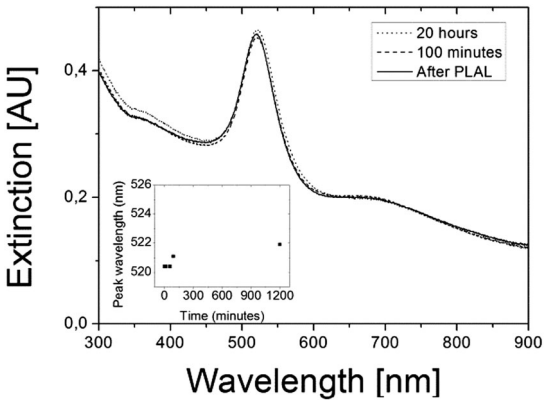

Fig. 5 Extinction spectra development for a sample prepared with lower TEOS concentration of 0.25 mM. The plasmon resonance peak is shifting only by approximately 1 nm and no shell formation can be observed in TEM analysis of the sample.

The shift in this case is most likely due to growth of a very thin shell or agglomeration.

Effect of the laser wavelength

To better understand the mechanisms responsible for the successful shell growth, we performed experiments with the laser wavelength of 1030 nm. For these experiments we used ready-made Stöber-solutions that gave the best results with the 515 nm wavelength. Unlike in the case of the green laser, we observed only partial growth of the shell as shown in Fig. 2(D). This suggests that the laser wavelength is an important factor to facilitate the direct growth of the shells on the gold nanoparticles. The plasmon resonance peak observed in the extinction measurements immediately after PLAL is near 520 nm, which is very close to the 515 nm wavelength. The plasmon resonances of the nanoparticles have primarily two effects. Firstly, the resonance enhances the local electromagnetic field strength near the surface of the particles, and secondly, the absorbed field will heat the particles. The difference in the field enhancement between the used wavelengths is less than an order of magnitude. Moreover, it is unclear what effects the enhancement of the field has on the growth of the silica shell. A much larger difference can be expected in the temperature of the nanoparticles. According to ref. 10, the maximum temperature change, $\Delta T_{\max}$, reached by the gold nanoparticles of radius R_{NP} under illumination of intensity I_0 can be estimated from:

$$\Delta T_{\max}(I_0) = \frac{{R_{\mathrm{NP}}}^2}{3k_0}\mathrm{Re}\left[i\omega\frac{1-\varepsilon(\mathrm{r})}{8\pi}\left|\frac{3\varepsilon_0}{2\varepsilon_0+\varepsilon_{\mathrm{m}}}\right|^2\right]\frac{8\pi I_0}{c\sqrt{\varepsilon_0}}, \qquad (1)$$

where k_0 is the thermal conductivity of 2-propanol, ω is the angular frequency of the laser, ε_0 and ε_{m} are the dielectric functions of the surrounding media and the metal, correspondingly, and c is the speed of light under vacuum. The model predicts a temperature difference by a factor of approximately 350 between the wavelengths of 515 nm and 1030 nm. For the parameters used in this study, the temperature of a produced nanoparticle with a diameter of 20 nm that interacts with the laser beam at a distance of 9 mm from the focal point is only increased by approximately 3 degrees in the case of the 1030 nm laser and by about 1000 degrees, *i.e.* to the melting point of gold in the case of the 515 nm laser. This temperature is high enough for considerable TEOS decomposition[11] and may lead to direct bonding of gold to free silicon atoms/ions or decomposition products of TEOS. This initial layer may then serve as a platform for further growth of silica shells through the Stöber-process after the PLAL process.

Heating the nanoparticles to such high temperatures leads to the decrease in the size of the nanoparticles through evaporation, but also to sintering of molten, colliding nanoparticles. This can be observed from the TEM images, *e.g.* Fig. 2(A), (B) and (D). It is worth noting that as the temperature of gold increases, the refractive index of gold changes and results in diminishing intensity of the plasmon resonance. Finally, the resonance disappears completely for molten gold.[12,13] This leads to less energy being absorbed by the hot particles and suppresses evaporation of the produced nanoparticles.

Due to the large difference in the temperature increase, sintering is not typically observed for infra-red lasers. However, with the high repetition rate laser we applied, the laser pulses have short time delays and they arrive close to each other on the target surface. Under these conditions the density of the nanoparticles produced by the previous laser pulse is still very high near the surface of the target. In close vicinity of the focal point the 1030 nm wavelength can cause considerable heating, although it is not intensive enough to heat the produced nanoparticles further away in the colloid and initiate the TEOS transformation. Therefore, in our samples, some sintering is observed as can be seen in Fig. 2(D). Due to these reasons, to avoid fused agglomerates in favour of individual core–shell-nanoparticles, a lower repetition rate laser is required.

Extinction spectra

We measured the extinction spectra of the nanoparticle colloids and related its changes to the growth of the silica shell. In the case of the sample shown in Fig. 2(B) and (C) the plasmon peak is observed to red-shift by approximately 5 nm during 20 hours (Fig. 4). Calculations of the optical properties of the coated metal nanoparticles with the MNPBEM toolbox[14] for the 10 to 15 nm shells observed in the TEM images yield a change of approximately 6 to 7 nm for the amorphous silica shells. The plasmon peak is very sensitive to the permittivity of the material of the shell and for a less dense material, which is most likely the case for TEOS-grown shells, the red-shift is smaller. Therefore the calculations are well in line with the observations.

The spectra in Fig. 3–5 show a feature near 700 nm which likely results from the agglomerated and fused nanoparticles. The shape of the feature changes and the extinction at wavelengths longer than the plasmon resonance increases for samples where silica growth is identified in TEM images (Fig. 3 and 4). This is attributed to further, TEOS and silica induced agglomeration.

For samples where the silica coating of the gold nanoparticles was incomplete, a much smaller red shift or no shift at all was observed. Therefore it is possible that the observations by Barcikowski *et al.*[6] are a result of partial silica growth or PVP coverage since no red-shift of the plasmon peak was observed. The wavelength of the femtosecond pulse laser that they used was 800 nm and therefore, if the mechanism responsible for the initial shell formation is heating of the formed nanoparticles as suggested by our results, the lack of silica shells would be expected.

IV. Conclusions

We have shown that coating of individual and agglomerated gold nanoparticles with silica shells can be achieved in a single-step PLAL process in the presence of TEOS and ammonia in 2-propanol. The best results are achieved when the 515 nm wavelength is used for ablation, suggesting that heating of the nanoparticles in the solvent is a crucial step to initiate the formation of the shell. It is possible that heating leads to breaking of TEOS molecules and bonding of silicon to the surface of the gold nanoparticles. Silicon can then act as the seed for the silica growth during the following Stöber-process.

This approach allows coating of gold nanoparticles without additional coupling agents or ligands.

As a future work it would be interesting to repeat the experiment with a lower repetition rate laser in an attempt to produce individual core–shell nanoparticles without the fused clusters. If the issue related to sedimentation during catalyst addition can be avoided, it would be interesting to see if the laser-induced heating could be used to seed the growth of the shell for ready-made nanoparticles.

Acknowledgements

We acknowledge Tero Kumpulainen, Ari Stjerna and Jorma Vihinen for their help with the laser. We would also like thank Vincenzo Amendola and Stephan Barcikowski for the insightful discussions during the ANGEL 2012 conference.

This work was funded by European Regional Development Fund through Council of Pirkanmaa in project EA31189.

Notes and references

1 W. Stöber and A. Fink, *J. Colloid Interface Sci.*, 1968, **26**, 62.
2 L. M. Liz-Marzán, M. Giersig and P. Mulvaney, *Langmuir*, 1996, **12**, 4329.
3 J. Xu and C. C. Perry, *J. Non-Cryst. Solids*, 2007, **353**, 1212.
4 E. Mine, A. Yamada, Y. Kobayashi, M. Konno and L. M. Liz-Marzán, *J. Colloid Interface Sci.*, 2003, **264**, 385.
5 C. Fernández-López, C. Mateo-Mateo, R. A. Álvarez-Puebla, J. Pérez-Juste, I. Pastoriza-Santos and L. M. Liz-Marzan, *Langmuir*, 2009, **25**, 13894.
6 S. Barcikowski, J. Jakobi, S. Petersen, A. Hahn, N. Bärsch, B. Chichkov, Proceedings of 24th International Conference on Applications of Lasers and Electro-Optics ICALEO, 10/29/2007 to 11/01/2007, Orlando, FL, USA. 108-113.
7 C. Graf, D. L. J. Vossen, A. Imhof and A. van Blaaderen, *Langmuir*, 2003, **19**, 6693.
8 S. Petersen and S. Barcikowski, *Adv. Funct. Mater.*, 2009, **19**, 66.
9 P. Wagener, G. Brandes, A. Schwenke and S. Barcikowski, *Phys. Chem. Chem. Phys.*, 2011, **13**, 5120.
10 A. O. Govorov, W. Zhang, T. Skeini, H. Richardson, J. Lee and N. A. Kotov, *Nanoscale Res. Lett.*, 2006, **1**, 84.
11 J. C. S. Chu, J. Breslin, N. S. Wang and M. C. Lin, *Mater. Lett.*, 1991, **12**, 179.
12 M. Otter, *Z. Phys.*, 1961, **161**, 163.
13 M. A. van Dijk, *Nonlinear optical studies of single gold nanoparticles*, *Ph. D. thesis*, Leiden University, Leiden, 2007.
14 U. Hohenester and A. Trügler, *Comput. Phys. Commun.*, 2012, **183**, 370.

Tampereen teknillinen yliopisto
PL 527
33101 Tampere

Tampere University of Technology
P.O.B. 527
FI-33101 Tampere, Finland

ISBN 978-952-15-3042-5
ISSN 1459-2045